MARIA CLARA COIMBRA GONÇALVES

EXPERIMENTAL INVESTIGATION ON MICROMILLING MACHINING OF Ti-6Al-4V TITANIUM ALLOY ADDITIVELY MANUFACTURED BY SELECTIVE LASER MELTING (SLM)

São Paulo
2022

MARIA CLARA COIMBRA GONÇALVES

EXPERIMENTAL INVESTIGATION ON MICROMILLING MACHINING OF Ti-6Al-4V TITANIUM ALLOY ADDITIVELY MANUFACTURED BY SELECTIVE LASER MELTING (SLM)

CORRECTED VERSION

A Dissertation submitted to the Polytechnic School of the University of São Paulo in fulfillment of the requirements to obtain the Title of Master in Sciences.

Field of research:

Design and Manufacturing

Advisor:

Gilmar Ferreira Batalha

São Paulo
2022

Autorizo a reprodução e divulgação total ou parcial deste trabalho, por qualquer meio convencional ou eletrônico, para fins de estudo e pesquisa, desde que citada a fonte.

Este exemplar foi revisado e corrigido em relação à versão original, sob responsabilidade única do autor e com a anuência de seu orientador.

São Paulo, 22 de março de 2022

Assinatura do autor: Maria Clara Coimbra Gonçalves

Assinatura do orientador: Gilmar Ferreira Batalha

Catalogação-na-publicação

Gonçalves, Maria Clara Coimbra
EXPERIMENTAL INVESTIGATION ON MICROMILLING MACHINING OF Ti6Al4V TITANIUM ALLOY ADDITIVELY MANUFACTURED BY SELECTIVE LASER MELTING (SLM) / M. C. C. Gonçalves -- versão corr. -- São Paulo, 2022.
131 p.

Dissertação (Mestrado) - Escola Politécnica da Universidade de São Paulo. Departamento de Engenharia Mecânica.

1.Processos de Fabricação 2.Microfresamento 3.Ligas de titânio 4.Manufatura Aditiva 5.Ti6Al4V I.Universidade de São Paulo. Escola Politécnica. Departamento de Engenharia Mecânica II.t.

ACKNOWLEDGMENTS

This work was possible thanks to the guidance of Prof. Dr. Gilmar Ferreira Batalha and Prof. Dr. Rodrigo Lima Stoeterau and the financial aid provided by the National Council for Scientific and Technological Development (CNPq).

Many thanks to MSc. Marcello Mergulhão and Prof. Dr. Maurício Neves, IPEN researchers, for their collaboration and supply of the printed material, and also to the company OMNITEK, where the samples of this work were printed.

My sincere appreciation for the assistance provided by MSc. Milla Gomes and Prof. Dr. Márcio Bacci, from the Federal University of Uberlândia (UFU), on doing part of the experimental procedures reported in this dissertation.

Thanks to Prof. Dr. Ed Claudio Bordinassi and Prof. Dr. Sérgio Delijaicov for their willingness to help with the sample's residual stress measurements.

Also, I am grateful for the structure provided by the Polytechnic School of the University of São Paulo (USP), specifically the Surface Phenomena Laboratory (LFS). Special thanks to all other students who have helped me somehow and to the technicians MSc. Raphael Ferreira, Cássio Junqueira, Fidel and Rafael Melchior for all their help.

Lastly, I am grateful to have found all the necessary support from my family and friends during this period of studies.

ABSTRACT

Increasingly, small size components are being used by many fields which use miniaturized products as working tools, highlighting the medical and dental industries. Both micromachining and additive manufacturing processes can be separately applied to obtain these products, but combining both processes show great potential for reducing manufacturing time and costs. In this context, additive manufacturing processes, such as Powder Bed Fusion (PBF), have gained attention in producing near-net-shape components due to their lower material consumption and ability to generate complex geometries. However, parts manufactured by this process present two main characteristics: periodic surface and anisotropy related to their printing direction. Therefore, machining processes such as micromilling need to be done on the parts in order to achieve the desired dimensional, geometric and/or roughness tolerances. However, the study of micromilling process in printed parts is recent and its machinability is poorly known. Thus, this work aims to make a comparison between the results of the micromilling process of conventional and printed parts by Selective Laser Melting, with and without heat treatment. The material analyzed was the titanium alloy Ti-6Al-4V, which is one of the most applied titanium alloys in aerospace, aeronautical, medical and dental sectors. For this reason, micromilling tests were carried out, varying the machining parameters, to analyze the results of machining forces, surface roughness, burr formation and residual stresses. In addition, a comparison was made with the results made on a micro milling machine with a mini dynamometer and a conventional CNC machine. With the obtained results, it was observed that, for the set of parameters used, no significant difference was observed on machining forces, surface roughness and burr formation for micromilling samples of commercial Ti6Al4V and additively manufactured. In addition, the machining force results collected in a conventional CNC were higher due to the robustness of this system. It is also noteworthy that, for the experiments on this work, the cutting speed was the most influential parameter on the cutting forces and the feed influenced the feed forces the most. The best surface roughness results were obtained for the smallest micromills and at high speeds. Also, burr formation presented a correlation with feed forces results. Furthermore, adhesion of material on the cutting edge of the tool was observed in the experiments. Therefore, the obtained results corroborate to the improvement of the micromachining process in materials with low machinability. Thereby, aiming to optimize this process and to produce high quality components.

Keywords – Micromilling. PBF. Titanium alloys. Ti-6Al-4V. Additive Manufacturing.

RESUMO

Cada vez mais, componentes em tamanho reduzido vêm sendo utilizados por diversos tipos de indústrias, onde destacam-se as áreas médica e odontológica, que utilizam muitos desses produtos miniaturizados como ferramentas de trabalho. Tanto processos de microusinagem quanto processos de manufatura aditiva podem ser separadamente utilizados para obtenção desses produtos mas, a combinação de ambos mostra grande potencial para redução de tempo e custos de fabricação. Nesse contexto, processos de manufatura aditiva, como a Fusão em Leito de Pó (PBF), ganharam atenção na fabricação *near net shape* de componentes devido ao seu menor consumo de material e capacidade de gerar geometrias complexas. Porém, as peças provenientes desse processo apresentam duas características: acabamento superficial irregular e anisotropias relacionadas à sua direção de impressão. Por isso, processos de usinagem, como o microfresamento, precisam ser aplicados para que as peças alcancem as tolerâncias dimensionais, geométricas e/ou rugosidade desejadas. No entanto, o estudo do processo de microfresamento em peças impressas é recente e sua usinabilidade é pouco conhecida. Com isso, este trabalho tem por objetivo fazer uma comparação entre os resultados do processo de microfresamento de peças convencionais e impressas por Fusão Seletiva a Laser, com e sem tratamento térmico. O material analisado foi a liga Ti-6Al-4V que é uma das ligas de titânio mais aplicadas na indústria nos setores aeroespaciais, aeronáuticos, médicos e odontológicos. Para isso, ensaios de microfresamento foram realizados, variando-se os parâmetros de usinagem, para analisar os seus resultados de forças, rugosidade, formação de rebarbas e tensões residuais. Além disso, foi feita uma comparação dos resultados feitos em uma microfresadora com um minidinamômetro e uma CNC convencional. Com os resultados obtidos, observou-se que não houve diferença significativa entre os resultados das forças de usinagem, rugosidade e formação de rebarbas para as diferentes amostras analisadas. Além disso, os resultados das força de usinagem e rugosidade coletados na CNC convencional foram mais altos devido a robustez do sistema. Destaca-se também que, a velocidade de corte foi o parâmetro mais influente nas forças de corte e o avanço influenciou mais as forças de avanço. Os melhores resultados de rugosidade foram obtidos para as menores fresas e em altas velocidades e a formação de rebarbas apresentou uma correlação com os resultados das forças de avanço. Além disso, foram observados os mecanismos de *tool run-out* e formação de aresta postiça de corte nos experimentos. Logo, os resultados obtidos corroboram para a melhoria do processo de microusinagem em materiais de difícil usinabilidade, visando a otimização desse processo e produção de componentes de alta qualidade.

Palavras-chave – Microfresamento. PBF. Ligas de Titânio. Ti-6Al-4V. Manufatura Aditiva.

LIST OF FIGURES

1 Metal additive manufacturing market in 2020 25

2 LPBF process applications: (**a**) tool insert with cooling channels; (**b**) CoCr dental restorations and titanium hip implants; and (**c**) pneumatic valve . . 26

3 Comparison of the buy-to-fly ratio between machining processes and 3D printing 27

4 Manufacturing costs per part by: (**a**) conventional processes and (**b**) Powder Bed AM processes 27

5 Illustration of the LPBF process 28

6 Principle of the LPBF process 29

7 Costs related to the AM process by SLM: (**a**) Division of the production total cost and (**b**) Division of the SLM production cost only 29

8 Schematic of a pseudo-binary isomorphous phase diagram 33

9 Titanium binary phase diagrams with different alloying elements 34

10 (**a**) Ti-6Al-4V titanium alloy microstructure with α and β phases highlighted (**b**) Ti-6Al-4V alloy highlighted in a pseudo-binary isomorphous phase diagram 35

11 CCT diagram for Ti-6Al-4V alloy 36

12 Common microstructures for Ti-6Al-4V alloy: **(a)** Conventional annealed alloy, **(b)** Bimodal, **(c)** Equiaxial and **(d)** Lamellar 37

13 SEM images of a LPBF printed Ti-6Al-4V alloy with zoom in the indicated areas 38

14 Orthogonal cutting process geometry 40

15 **(a)** Contact zones during cutting and **(b)** Cutting force diagram 41

16 Helical end mill geometry 42

17 Machining force components and chip geometry in milling 43

18 Up and down milling processes 43

19 **(a)** R_a profile representation and **(b)** S_a profile representation 45

20 **(a)** S_p roughness, **(b)** S_v roughness and **(c)** S_z roughness 46

21 Surface profiles according to a variation on S_{sk} and S_{ku} values 46

22 $2\theta \times sin^2\Psi$ graph 49

23 Cutting tools damage and wear types 51

24 Types of milling burrs 53

25 Burr thickness and height 54

26 Mechanisms of tool-workpiece interaction for different depths of cut: **(a)** Rubbing, **(b)** Burnishing, **(c)** Ploughing (negative rake angle) and **(d)** Cutting (positive rake angle) 55

27 Schematic of the effect of the minimum chip thickness 56

28 Chip morphology comparison when micro cutting Ti-6Al-4V cast and SLM for different feed and speeds 58

29 SEM image of the used Ti-6Al-4V powder 62

30 (**a**) 3D OmniSint-160 printer. (**b**) Printed samples without heat treatment. 62

31 Considered profiles for 2D surface roughness measurements before machining 64

32 Roughness profiles before machining: (**a**) Parallel to printing direction (vertical) and (**b**) Perpendicular to printing direction (horizontal) 66

33 3D roughness profile before machining: (**a**) Sample 1, (**b**) Sample 2 and (**c**) Sample 3 67

34 OM images (500x) of the: (**a**) printed sample and (**b**) conventional sample 68

35 SEM images (2000x) of the: (**a**) printed sample and (**b**) conventional sample 68

36 EDS spectrum of the: (**a**) printed sample e (**b**) conventional sample 69

37 Scheme of the forces acquisition system 70

38 Micromill geometry 70

39 Micromills used for the experiments: (**a**) 0,5 mm e (**b**) 0,8 mm 71

40 Methodology used to estimate the tool nose radius 71

41 Experimental setup 72

42 Force acquisition system used for the tests at Schaublin CNC machine . . . 73
43 (**a**) Schaublin CNC machine and (**b**) dynamometer and dial gauge 73
44 Experimental setup for experiments in the Schaublin CNC machine 73
45 Three-component piezoelectric dynamometer 74
46 MiniDyn multicomponent dynamometer 75
47 Samples dimensions 76
48 Shimadzu diffractometer available at FEI University Center 78
49 Hypothetical examples of the Pearson correlation coefficient 79
50 Cutting forces results for the conventional sample 81
51 Feed forces results for the conventional sample 82
52 Result of the cutting edge motion on cutting forces 82
53 Cutting forces results for the printed samples 84
54 Feed forces results for the printed samples 85
55 Cutting force results for the printed samples with heat treatment 86
56 Feed force results for the printed samples with heat treatment 86
57 Cutting forces results for: (**a**) conventional sample, (**b**) printed samples and (**c**) printed HT samples 87
58 Heat map for analyzing the correlation among the samples manufacturing process and **(a)** cutting forces and **(b)** feed forces results 87
59 Tool diameter measurements (μm) and effective channel width for the: (**a**) 0.5 and (**b**) 0.8 tools 88
60 Heat map for analyzing the correlation among the cutting parameters and cutting forces 89
61 Joint plot of Fc x Vc 90
62 Heat map for analyzing the correlation among the cutting parameters and feed forces 91
63 Joint plot of Ff x Feed. 91

64 Cutting forces for the Schaublin experiments with a tool diameter of: (**a**) 0.5 and (**b**) 0.8 mm 92

65 Feed forces for the Schaublin experiments with a tool diameter of: (**a**) 0.5 and (**b**) 0.8 mm 92

66 Heat map showing the correlation among the cutting forces, cutting speed and tool diameter for the Schaublin CNC experiments 93

67 Heat map showing the correlation among feed forces, cutting speed and tool diameter for the Schaublin CNC experiments 94

68 S_a average results for the conventional sample 95

69 S_q average results for the conventional sample 95

70 S_{sk} average results for the conventional sample 97

71 S_{ku} average results for the conventional sample 97

72 3D surface images for f = 2 μm/tooth for the conventional sample 98

73 S_a average results for the printed samples 99

74 S_q average results for the printed samples 99

75 S_{sk} average results for the printed samples 100

76 S_{ku} results for the printed samples 100

77 3D surface images for f = 2 μm/tooth for the printed samples 101

78 S_a and S_q results comparison between the printed sample with and without heat treatment for experiments with the 0.8 mm diameter tool and speed of 60 m/min 101

79 S_{sk} and S_{ku} results comparison between the printed sample with and without heat treatment for experiments with the 0.8 mm diameter tool and speed of 60 m/min 102

80 3D surface images for for the printed sample with and without heat treatment for the cutting parameters of f = 2 μm/tooth, Vc = 60 m/min and D = 0.8 mm 103

81 S_a and S_q results for the printed samples machined on the Schaublin CNC 103

82 S_{sk} and S_{ku} results for the printed samples machined on the Schaublin CNC 103

83 3D surface images for f = 1 μm/tooth for the printed samples machined on the Schaublin CNC . . . 104

84 Heat map showing the correlation among surface roughness and the cutting parameters for the CNC Mini-mill experiments . . . 105

85 Heat map showing the correlation among surface roughness and the cutting parameters for the Schaublin CNC experiments . . . 105

86 Residual stress results variation with samples . . . 107

87 Heat map showing the correlation between the RS results, samples and measured direction . . . 107

88 Mean burr height estimation for conventional sample with Vc = 60 m/min and fz = 1 μm/tooth . . . 108

89 Heat map showing the correlation among cutting parameters and burr height 109

90 SEM images showing burr formation for each milling condition using the tool diameter of 0.5 mm . . . 110

91 SEM images showing burr formation for each milling condition using the tool diameter of 0.8 mm . . . 111

92 Illustration of the binary image used for estimating burr area. The images presented are from the: (**a**) conventional sample and (**b**) printed samples, both machined with the 0.5 mm tool diameter, Vc = 40 m/min and f = 1.5 μm/tooth . . . 111

93 Heat map showing the correlation between the feed forces and burr area results for: (**a**) 0.5 mm and (**b**) 0.8 mm tool diameters . . . 113

94 Burrs for the experiments made on the Schaublin CNC . . . 114

95 Tools after milling each sample . . . 116

96 Tool sides after milling each sample (D = 0.5 mm, tool #1) . . . 117

97 Tool sides after milling each sample (D = 0.8 mm, tool #3) . . . 118

98 Chip formation after milling the printed TT sample (D = 0.5 mm, tool #2) 118

LIST OF TABLES

1 Chemical composition of conventional Ti-6Al-4V alloy (grade 5) 34

2 Properties of pure titanium and Ti-6Al-4V alloy 35

3 Chemical composition required for the Ti-6Al-4V powder 37

4 Required mechanical properties for Ti-6Al-4V components manufactured via PBF 38

5 Powder's chemical composition analysis XRF 61

6 Particle size distribution of Ti-6Al-4V powder 61

7 LBPF process parameters 62

8 Average hardness of all three LPBF printed samples without heat treatment (Vickers Hardness, load of 30 kgf, time 15s, three repetitions) 63

9 Hardness measurements on the conventional Ti-6Al-4V sample (Vickers Hardness, load of 50 kgf, time 15s) 63

10 Roughness parameters measured in each direction of the specimen before machining 65

11 3D roughness parameters obtained for the printed samples before machining 66

12 Experiments' factorial design 76

13 Diffractometer parameters 77

14 Pearson's correlation coefficient interpretation 79

15 Machining force results for the conventional sample 83

16 Machining force results for the printed samples 83

17 Machining force results for the printed samples with heat treatment 84

18 Surface roughness results for the conventional sample 96

19 Surface roughness results for the printed samples 99

20 Surface roughness results for the printed samples with heat treatment . . . 102

21 Residual stress results 106

22 Burr height results 109

23 Burr area results 112

24 Burr results for the Schaublin experiments 114

NOMENCLATURE

AM Additive Manufacturing

BCC Body-centered cubic

BSE Backscattered Electrons

BUE Built up edge

CCT Continous Cooling Transformation

CNC Computer Numerical Control

$DMLM$ Direct Metal Laser Melting

$DMLS$ Direct Metal Laser Sintering

DOE Design of Experiments

EBM Electron Beam Melting

EDS Energy Dispersion Spectroscopy

ELI Extra Low Interstitial

HCP Hexagonal close packed

HRC Hardness Rockwell C

HT Heat Treatment

$IPEN$ Nuclear and Energy Research Institute

LM Layer Manufacturing

OM Optical Microscope

PB Powder Bed

PBF Laser Powder Bed Fusion

PBF Powder Bed Fusion

PCI Peripheral Component Interconnect

RMS Root Mean Square

RP Rapid Prototyping

RPM Revolutions per minute

RS Residual Stress

SEM Scanning Electron Microscope

SLM Selective Laser Melting

SLS Selective Laser Sintering

XRD X-Ray Diffraction

XRF X-Ray Fluorescence

SYMBOLS

Physical quantity	**Symbol**	**SI unit**
Cutting speed	V_c	m/min
Cutting force	F_c	N
Feed force	F_f	N
Shear force	F_s	N
Normal force	F_n	N
Axial force	F_a	N
Radial force	F_r	N
Tangential force	F_t	N
Cutter rotation angle	ψ	$^\circ$
Specific axial force	K_{ac}	N/mm^2
Specific radial force	K_{rc}	N/mm^2
Specific tangential force	K_{tc}	N/mm^2
Arithmetic mean height of a line	R_a	μm
Root mean square height of a line	R_q	μm
Maximum height of peaks in a line	R_p	μm
Maximum depth of valleys in a line	R_v	μm
Maximum height parameter in a line	R_z	μm
Skewness - line	R_{sk}	-
Kurtosis - line	R_{ku}	-
Arithmetic mean height of an area	S_a	μm
Root mean square height of an area	S_q	μm
Maximum height of peaks in an area	S_p	μm
Maximum depth of valleys in an area	S_v	μm
Maximum height parameter in an area	S_z	μm
Skewness - area	S_{sk}	-
Kurtosis - area	S_{ku}	-
Wavelength	λ	m
Refraction angle	θ	$^\circ$
Residual stress	σ	MPa
Diffraction plane constant	K	kg/mm^2/deg
Diffraction angle	Ψ	$^\circ$
Burr height	h	μm
Burr thickness	b	μm
Tool diameter	D / $\varnothing$	mm
Feed per tooth	fz	μm/tooth
Root mean square of force	F_{RMS}	N
Population correlation coefficient	ρ	-
Pearson's correlation coefficient	r	-

CONTENTS

Symbols

1 Introduction **19**

1.1 Justification 20

1.2 Objectives 21

1.2.1 General objectives 21

1.2.2 Specific objectives 21

1.3 Structure and organization 22

2 Literature review **23**

2.1 Additive manufacturing 23

2.1.1 Additive Manufacturing processes 24

2.1.2 Additive Manufacturing of metallic components 26

2.1.3 Laser Powder Bed Fusion process 28

2.1.4 Methods for raw material characterization 29

2.2 Titanium 31

2.2.1 Titanium alloys 32

2.2.2 Ti-6Al-4V Alloy Properties 33

2.2.2.1 Properties of Ti-6Al-4V alloy printed by LPBF 37

2.2.3 Titanium α case layer 39

2.3 Machining 39

2.3.1 Cutting forces 39

2.3.2 Surface roughness 44

2.3.3 Residual stress 47

2.3.4 Tool wear . . . 49
2.3.5 Burr formation . . . 52
2.4 Micromilling . . . 54
2.4.1 Definition . . . 54
2.4.2 Scale effect . . . 55
2.4.3 Cutting parameters influence on the micromilling process . . . 56
2.5 Recent advances in Ti-6Al-4V micromachining . . . 57

3 Materials and Methods 60

3.1 Laser Powder Bed Fusion process . . . 60
3.1.1 Powder characterization . . . 60
3.1.2 Printing process . . . 61
3.2 Samples characterization . . . 63
3.2.1 Hardness measurements . . . 63
3.2.2 Roughness measurements . . . 64
3.2.3 Microscopy analysis . . . 67
3.3 Micromilling process . . . 69
3.3.1 Materials used . . . 69
3.3.2 Design of experiments . . . 75
3.4 Procedures for data analysis . . . 76
3.4.1 Pearson correlation coefficient . . . 78

4 Results and discussion 80

4.1 Machining forces analysis . . . 80
4.1.1 Conventional sample . . . 80
4.1.2 Printed samples . . . 83
4.1.3 Printed samples with heat treatment . . . 84
4.1.4 Analysis and comparisons of machining forces data . . . 85

4.1.5 Cutting forces results for Schaublin CNC experiments 92
4.2 Surface roughness analysis 95
4.2.1 Conventional sample 95
4.2.2 Printed samples 98
4.2.3 Printed samples with heat treatment 100
4.2.4 Surface roughness results for Schaublin CNC experiments 102
4.2.5 Cutting parameters influences on surface roughness data 104
4.3 Residual stress results 106
4.4 Burr formation 108
4.4.1 Burr height results 108
4.4.2 Burr area results 110
4.5 Burr area results for Schaublin CNC experiments 113
4.6 Tool conditions 115

5 Conclusions **119**

5.1 Future works 121

References **122**

1 INTRODUCTION

Lately in media and literature, the terms *Additive Manufacturing* (AM) and *3D Printing* are being used to refer to all solid free-form fabrication technologies, such as Powder Bed Fusion processes (PBF) as Selective Laser Melting (SLM), also referred as Laser Powder Bed Fusion (LPBF), and Selective Laser Sintering (SLS) [CHIA; WU, 2015]. Recent developments on these 3D printing strategies are making it possible to expand the amount of available materials and to reduce production time.

Regarding the advantages of additive manufacturing processes, its lower resource consumption, complex shapes production, less material waste and the possibility of a rapid manufacturing in a variety of materials should be highlighted [UHLMANN et al., 2015; CHEN et al., 2017; XIONG; ZHANG; WANG, 2009]. In addition, in applications where conventional manufacturing is impossible or extremely difficult to apply, ready-to-use or near-net-shaped 3D printed parts are a solution.

The Additive Manufacturing application areas are extensive. According to Chia and Wu [2015], a promise of 3D printing is the production of complex biomedical devices that follow a computer design using patient-specific anatomical data. In this aspect, an area of great interest in the advancement of this technology is the medical field, which aims to use this technology routinely for regeneration of complex tissues such as bones, cartilage, muscles, vessels and nerves [CHIA; WU, 2015]. These technologies are already available on the market and are currently being used, for example, to manufacture orthodontic appliances.

Another area with good prospects for the application of parts manufactured by AM is the aeronautical industry. According to Uhlmann et al. [2015], in the global market, there is a demand for more than 28,000 new commercial aircraft for the period 2012-2031, due to the need to replace older aircraft. According to the authors, additive manufacturing generates opportunities for designing lightweight parts with an optimized topology to meet this demand. Furthermore, the authors point out that an investigation on the machinability and the mechanical properties of Ti-6Al-4V samples produced by PBF are

important topics to investigate.

In this sense, metallic materials are used to manufacture a range of components and micro-components for medical, dental, aerospace and aeronautical industries. Among them, titanium and its alloys are widely applied due to their high corrosion resistance, excellent mechanical strength and low density [BALDO, 2013]. Concerning the AM process of metallic components, it is currently possible to obtain, by this method, products with mechanical properties superior to those obtained through traditional methods [BREMEN; MEINERS; DIATLOV, 2012; MERGULHÃO, 2017].

Even with all benefits of applying AM strategies on metallic micro-components production, the outcome parts present an anisotropy related to the printing direction and high surface roughness. In order to achieve the desired dimensional, geometric tolerances and/or surface roughness specifications, micromachining processes, such as micromilling, are applied.

In this context, observing the importance of AM metallic parts in industry nowadays, the wide application of titanium alloys in micro-components manufacture and the need of micromachining as a finishing process for printed materials, this work aims to add a contribution on the micromilling process analysis of LPBF printed Ti-6Al-4V titanium alloys. The general goal is to analyze the process outcomes, as cutting forces, surface roughness, residual stresses and burr formation, for the conventional and LPBF printed Ti-6Al-4V alloy with and without heat treatment.

1.1 Justification

As previously approached, the LPBF process enables the production of lightweight titanium parts with optimized topology. In addition, it has advantages such as better use of raw material and *near net shape* production of components [UHLMANN et al., 2015; CHEN et al., 2017]. However, additive manufactured parts presents high surface roughness, low dimensional and geometric accuracy and high residual stresses [VAFADAR et al., 2021]. As a consequence, there is a need of post-processing operations to improve the parts' properties and accuracy, particularly for applications in medical and dental industry. In that regard, micromilling techniques can be used to overcome the limitations generated by 3D printing processes.

Among the materials used in microcomponents production, resistant materials with good ductility, corrosion resistance and biocompatibility are desired. The titanium alloy

Ti-6Al-4V stands out for its properties, and it is the titanium alloy most used by industries, given that 50% of the global production of this metal is dedicated to its production. Furthermore, the aerospace industry consumes 80% of the global production of this alloy, demonstrating its importance for the segment [SHOKRANI; DHOKIA; NEWMAN, 2016].

However, few research was developed in the area of micromachining of titanium alloys if compared to materials such as steel and aluminum, specifically if the micromilling LPBF printed alloys are considered [JAFFERY et al., 2015]. Thus, a need of studies investigating the micromachining process of this material and its machinability have been reported in literature [KURAM; OZCELIK, 2015].

Furthermore, the improvement of manufacturing techniques is fundamental in the development of optimized products. Micromachining, for example, has been growing thanks to the increase in machine precision and the development of new machining technologies and techniques [BALDO, 2013]. The integration of micromachining with LPBF is an area that has few studies and has promising application sectors.

1.2 Objectives

1.2.1 General objectives

This dissertation aims to present an analysis of the micromilling process in Ti-6Al-4V samples printed by LPBF. The main focus was to observe the differences of the micromilling process outcomes for a LPBF printed Ti-6Al-4V alloy with and without heat treatment and a conventional manufactured Ti-6Al-4V alloy.

Therefore, the behavior of cutting forces during the micromachining process of printed and conventional alloys were analyzed. For that, tests following a full factorial design were carried out varying the cutting speed, tool diameter and feed per tooth. After that, the resultant surface roughness and burr formation on the workpieces were evaluated. Additionally, tool conditions were analyzed during the experiments and a residual stress analysis was performed on each sample after machining. Tests in a robust system and with lower speed were also made for comparison purposes.

1.2.2 Specific objectives

For the development of this dissertation, the following specific objectives were established:

- Make a characterization of the samples used in the micromilling process in terms of its roughness, hardness and microstructure;
- Manufacture the necessary devices to carry out the tests;
- Check tool's integrity during the micromachining process;
- Carry out the micromilling tests measuring the cutting forces of the process;
- Measure the surface roughness and burr formation of the machined slots;
- Analyze the behavior of the cutting forces, surface roughness and burr formation regarding different cutting parameters;
- Analyze the residual stress of the samples regarding the micromilling influence;

1.3 Structure and organization

This dissertation is divided into five chapters, as described below:

Chapter 1 - Introduction: It includes a contextualization of the theme, the exposition of the motivation, the general and specific objectives and the organization of the work.

Chapter 2 - Literature Review: It covers a literature review on relevant points for the work, such as the LPBF process and its applications, the Ti-6Al-4V alloy and its machinability, the micromilling process and the influence of the machining parameters on surface roughness and cutting forces.

Chapter 3 - Materials and Methods: It presents the materials and procedures used to perform LPBF printing and micromilling tests. Among them, there are the characterization of the raw material for the LPBF process, the planning of machining experiments and the methodology for analyzing the results.

Chapter 4 - Results and Discussion: This section shows the analysis of the samples before machining and the results of forces, surface roughness, tensile stresses, burr formation and tool's conditions after performing the micromilling process.

Chapter 5 - Conclusions: It addresses the conclusions obtained from the project and from the results achieved. It also includes suggestions for future work.

2 LITERATURE REVIEW

2.1 Additive manufacturing

According to Silva [2017], at the beginning of the Industrial Revolution the term *Manufacturing* was understood as "a large production system with standardized and serial methods, that requires a division of work". Initially the term was related to human labor, but over time, products manufactured using machinery were also incorporated into the word manufacture.

Terms such as Additive Manufacturing, Rapid Prototyping and Hybrid Manufacturing have been widely used in today's media. This is related to the idea that the world is now at the beginning of the Fourth Industrial Revolution, which is supported by the use of new technologies that allow a mixture of the physical, digital and biological worlds. The industry arising from this industrial revolution is known as Industry 4.0 and it has promoted transformations in production, management and governance systems. Additive Manufacturing is an important technology for this industry, and the advances in this area and in areas such as nanotechnology, materials science, biotechnology, and others, are linked to the evolution of Industry 4.0 [SILVA, 2017].

Thereby, Additive Manufacturing can be defined as a technology that uses 3D printers to generate prototypes or functional objects from a CAD file. It starts by reading the CAD file, dividing the object into layers and building these layers in the printing machine to reproduce the object in three dimensions [DMITRIYEV et al., 2017].

Among the benefits of Additive Manufacturing, the rational use of raw material with less waste and a near-net-shape production of components are often highlighted [CHEN et al., 2017; UHLMANN et al., 2015]. This is due to the fact that Additive Manufacturing can considerably reduce the buy-to-fly ratio of a product. This ratio concerns the amount of raw material used and the amount of material in the finished part. Basically, the term refers to the amount of material that is purchased not to be effectively used in the final product, that is, the material wasted.

Dmitriyev et al. [2017] consider Additive Manufacturing as a *green* manufacturing process, since this technology has minimal material waste. This benefit is especially important in the production of components made with expensive raw materials or when recycling is not possible.

Even though metal AM technologies have almost unlimited potential, and the range of applications has increased in recent years, metrology and quality control are still a challenge regarding product quality [VAFADAR et al., 2021]. In this context, additive manufacturing, specially in metallic parts, can lead to anisotropy and heterogeneity in its mechanical properties. One way to provide the required mechanical properties to the parts is through post processing [KOK et al., 2018].

2.1.1 Additive Manufacturing processes

According to Ransikarbum, Pitakaso and Kim [2020], there are seven main categories of AM, as classified by the American Society for Testing and Materials. These categories and their common Metal AM Processes are summarized as follows, according to the descriptions presented in literature [AMERICAN SOCIETY FOR TESTING AND MATERIALS, 2015; RANSIKARBUM; PITAKASO; KIM, 2020; VAFADAR et al., 2021; ZHANG et al., 2018; PAGAC et al., 2021]:

- **VAT Photopolymerization**: category of processes in which a ultraviolet light is deployed to form chains between molecules of liquid light-curable resin, crosslink them, and as a result, solidify the resin. Common AM processes: Digital Light Processing, StereoLithograPhy and Continuous Digital Light Processing.

- **Material Extrusion**: methodology where the material is dispensed through a heated extrusion nozzle following a path to build the 3D parts. Common AM processes: Fused Deposition Modeling and Bound Powder Extrusion.

- **Powder Bed Fusion**: in these processes thermal energy such as electron and laser beams selectively melts and fuses the material in a powder bed. Among the PBF processes, there are: Direct Metal Laser Sintering (DMLS), Selective Laser Melting (SLM), Electron Beam Melting (EBM) and Direct Metal Laser Melting (DMLM).

- **Directed Energy Deposition**: where material in wire or powder form is selectively added to a substrate with sufficient energy to create a layer. Common process: Thermal Energy.

- **Material Jetting**: where the photopolymer resin is selectively sprayed to the target location in droplets, and UV light is used to cure and solidify the liquid material layer by layer. One common process is Nano Particle Jetting.
- **Binder Jetting**: it is a process where a liquid-state binder agent is selectively deposited onto the powder bed to bind the powder and form a layer of a part. Once one layer is printed, the build plate moves down, and the powder roller spreads a new layer of powdered material and the process continues until the part is finished.
- **Sheet Lamination**: processes where sheets of materials are bonded layer by layer to build the desired component. Common processes: Laminated Object Manufacturing and Ultrasonic Additive Manufacturing

According to Vafadar et al. [2021], applications of all these seven groups exist in the metal AM market, and the industrial adoption of these metal AM processes in 2020 is illustrated in Figure 1.

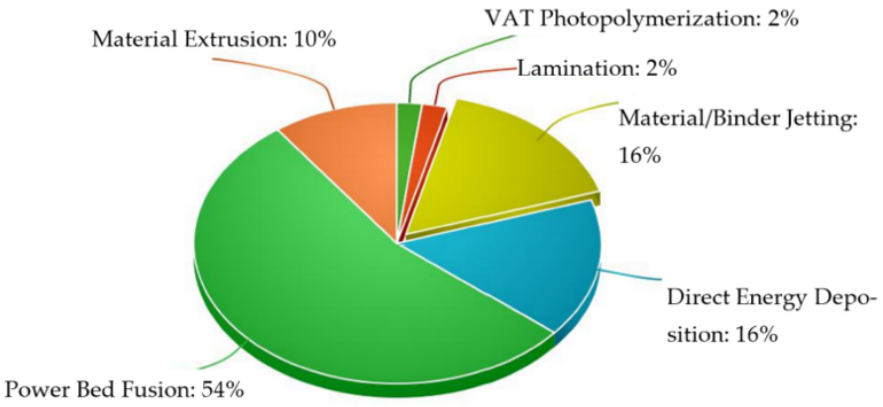

Figure 1: Metal additive manufacturing market in 2020. Source: [VAFADAR et al., 2021]

About these processes, it can be pointed out that the parts fabricated by ME are not metallic parts, but rather parts with metal content. Also, DMLM and DMLS are very similar processes, but in the DMLM a laser beam creates ultra-thin metal layers and provides a homogeneous melt pool, what improves surface quality and reduces porosity on the outcome part. On the other hand, in EBM technology, a high energy electron beam is used to fuse metal powder, instead of a laser as in the LPBF process [VAFADAR et al., 2021]. In addition, the construction time required to make a part by PBF is longer if compared to DED technologies, but it is possible to obtain more complex parts and better surface finish with this technology, facilitating their post-processing [BHAVAR et al., 2014]. This advantages makes the PBF technology the most popular one nowadays (Figure 1).

2.1.2 Additive Manufacturing of metallic components

According to Kruth et al. [2005] the technologies of Layer Manufacturing (LM) were developed in the late 80's as techniques for Rapid Prototyping (RP) . In the 2000s, the applications of these types of processes were expanded for purposes of prototyping, tooling and fabrication (Figure 2). This expansion was mainly due to the advancement of LM techniques in processing a wide variety of materials, obtaining products with physical and mechanical properties similar to those obtained by conventional processes [KRUTH et al., 2005; BREMEN; MEINERS; DIATLOV, 2012]. Figure 2 shows examples of layer manufacturing applications, all made of metallic materials.

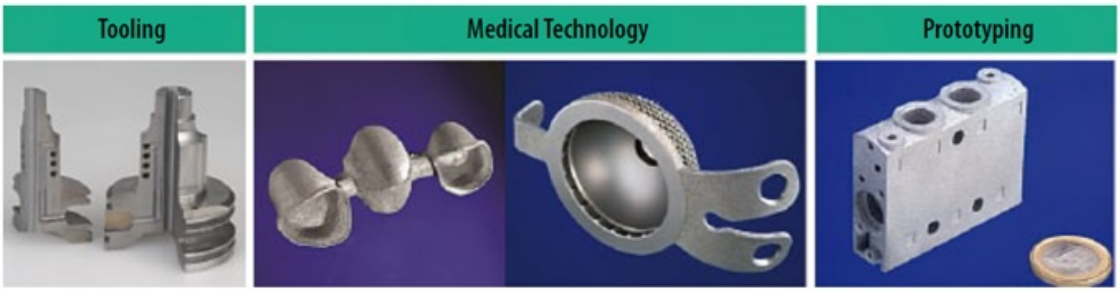

Figure 2: (**a**) tool insert with cooling channels; (**b**) CoCr dental restorations and titanium hip implants; and (**c**) pneumatic valve (Festo AG & Co. KG). Source: Bremen, Meiners and Diatlov [2012]

Silva [2017] points out that industries such as aerospace, automotive and medical are benefiting from advances in Additive Manufacturing in metal parts. Common processes for printing metallic 3D parts are: LPBF, DMLS and EBM. With these technologies, it is now possible to obtain complex objects that would be expensive, if not impossible, to be manufactured by conventional processes.

In this sense, in conventional manufacturing processes of metallic materials, the buy-to-fly ratio for parts from traditional machining can reach 20:1, as shown by Taminger [2008]. With Additive Manufacturing, as can be seen in Figure 3, for manufacturing the same part the buy-to-fly ratio reaches 2:1.

Figure 4 presents a distribution made by Barnes and Kingsbury [2016] related to the associated fabrication costs of titanium parts by machining and by Additive Manufacturing for application in aerospace industry. According to the authors, for Additive Manufacturing, the input material is significantly more expensive than other primary forms of titanium product. However, in addition to this technology being in expansion, its efficiency is increased by allowing the reduction of the total number of parts in a project, reducing labor in assembly operations and reducing supply chain management

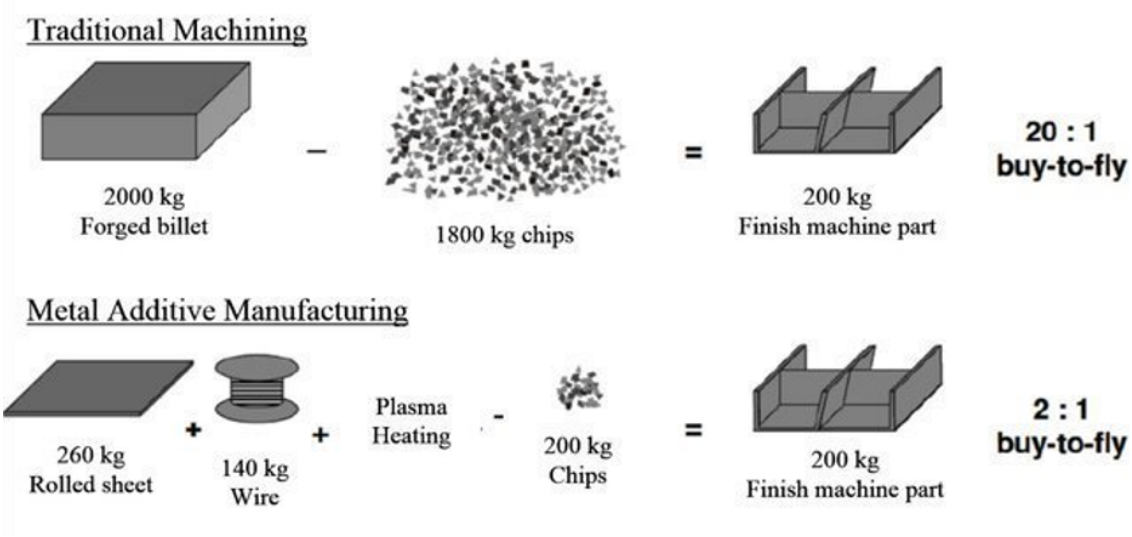

Figure 3: Comparison of the buy-to-fly ratio between machining processes and 3D printing. Source: Taminger [2008]

costs.

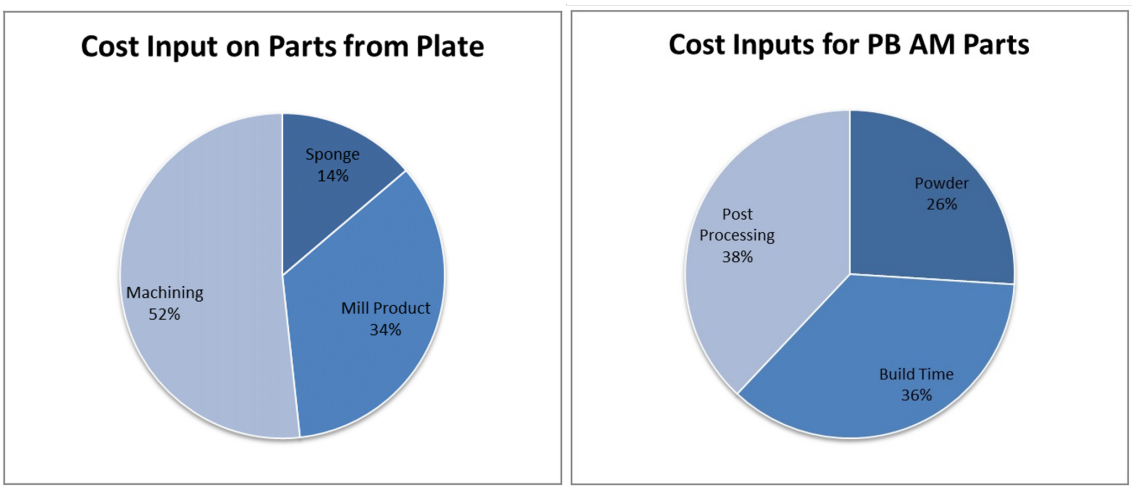

Figure 4: Manufacturing costs per part by: (**a**) conventional processes and (**b**) Powder Bed AM processes. Source: [BARNES; KINGSBURY, 2016]

In addition, the growth of Additive Manufacturing industry is predicted to be rapid and substantial as new equipment are developed, thus more materials become available and more end users adopt the technology [METAL-AM, 2020]. Among the industries that mostly adopted AM technologies, the aerospace, automotive, and industrial machines represents 60% of the market revenue in 2018 [WOHLERS et al., 2017]. Thus, according to Wohlers et al. [2017], the global value of this industry in terms of sales is expected to exceed U$15.8 billion dollars over the next years.

2.1.3 Laser Powder Bed Fusion process

The Laser Powder Bed Fusion process, in some cases referred to as Selective Laser Melting (SLM) process, is a specific Additive Manufacturing technique designed to use high power density laser to selectively melt and fuse metallic powders [YAP et al., 2015]. With this technique, components are built layer by layer by merging the powders into a selected area, as illustrated in Figure 5.

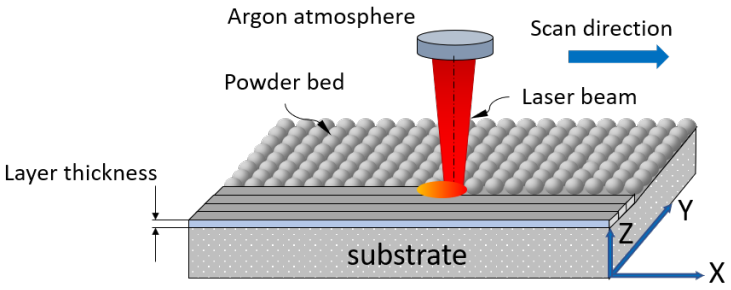

Figure 5: Illustration of the LPBF process

According to Bremen, Meiners and Diatlov [2012], the LPBF process can be divided into steps, as illustrated in Figure 6. First, the 3D-CAD volume model is divided into layers and transferred to the LPBF machine, then the process follows the subsequent dynamic:

- A thin layer of powder is deposited on a substrate;
- The regions that must contain solid material are scanned by the high power laser, in an inert atmosphere, producing one layer of the part;
- The platform/substrate is lowered down to the thickness of the layer produced, and the process is repeated until the entire part is manufactured;
- The component is removed from the machine and cleaned.

A benefit of the LPBF process, addressed by Bremen, Meiners and Diatlov [2012], is that it does not require special tools to manufacture a particular part, eliminating pre-production costs. In addition, it is possible to reach a density of approximately 100% in the LPBF process, since there is a complete fusion of powder. However, parts manufactured by this process have a higher roughness, low dimensional accuracy and high tensile residual stresses, which leads to the need of post-processing operations.

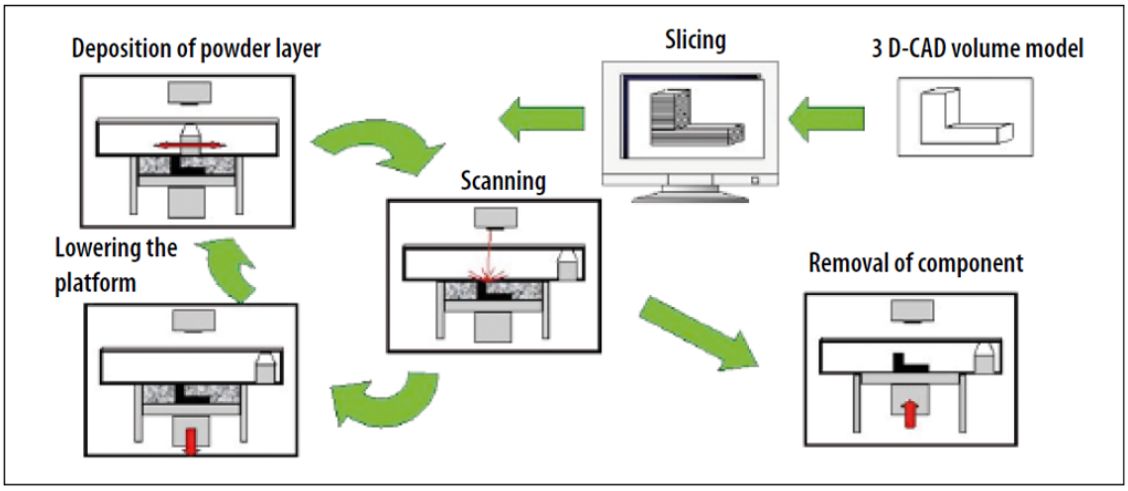

Figure 6: Principle of the LPBF process. Source: Bremen, Meiners and Diatlov [2012]

Another interesting point is about the cost related to the manufacturing process by LPBF/SLM. Previtali et al. [2017] concludes in their results that 87% of the total cost of production of parts by SLM is related to the printing process (Figure 7a). Nevertheless, the costs related to the SLM printing process can be divided into: equipment cost, which is the main cost factor according to Previtali et al. [2017], representing 52% of the total cost of the SLM process; overhead costs, which include labor, energy, administration, maintenance and security costs, and represent 30% of the total cost; material and tools costs (Figure 7b) [PREVITALI et al., 2017].

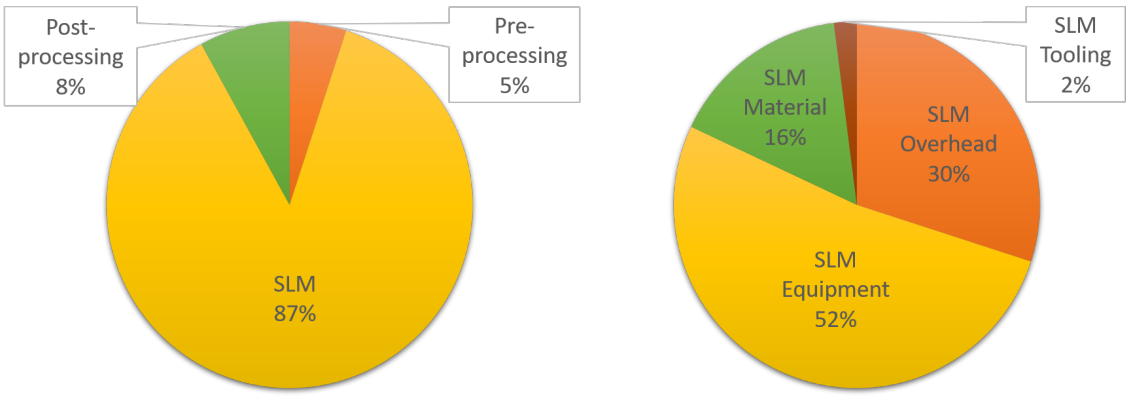

Figure 7: Costs related to the AM process by SLM: (**a**) Division of the production total cost and (**b**) Division of the SLM production cost only. Source: Previtali et al. [2017]

2.1.4 Methods for raw material characterization

The analysis of the raw material used for the LPBF process, in terms of the diameter and composition of the powder for example, is essential to guarantee the quality of the printed product. Some techniques are applied to carry out this process quality control.

Among them, as Oliveira [2011] defines, the X-Ray Fluorescence spectrometry (XRF) is a non-destructive technique used to identify the proportion and chemical elements present in a sample. In this technique, a high-energy radiation source excites the atoms in the sample, promoting electrons at more energetic levels. In this state, the atom in an unstable situation will emit energy to return to its ground state, and this energy is characteristic for each chemical element, what is used for its identification and quantification [OLIVEIRA, 2011].

The powder's particle size analysis is based on the inversion of a diffusion of a matrix, whose resolution is based on theories deriving from Maxwell's equations [CILAS, 2020]. In this analysis, Mie or Fraunhofer theories can be used to calculate particle size distributions ranging from tens of nanometers to thousands of micrometers [CILAS, 2020]. The application differences of these two models are explained in [ISO, 1999] standard, where the two methods are recommended in the analysis of spherical particles. The Fraunhofer method is recommended in the analysis of opaque materials and with particles with diameters much larger than the used laser wavelength or in cases where the material's refractive index is unknown [PAPINI, 2003; CILAS, 2020]. Thereby, the Fraunhofer theory of diffraction by means of laser diffraction/scattering is applied to specify particle sizes by means of the light intensity distribution pattern [SHIMADZU, 2019].

In addition to the raw material analysis, other parameters need to be considered for the LPBF manufacturing process, such as laser power and diameter, scan speed, thickness/distance between scans, temperature of the environment, type and volume of gas used in the modified atmosphere [BREMEN; MEINERS; DIATLOV, 2012; GRZESIAK; KRAWCZYK, 2015; MEIER; HABERLAND, 2008; GU et al., 2015]. These parameters directly influence the properties and quality of the material obtained.

Regarding the analysis of materials and their microstructure, the Scanning Electron Microscope (SEM) is a widely used equipment. In SEM the area to be analyzed is irradiated by a thin electron beam and with that a series of radiations are emitted, such as: secondary electrons, backscattered electrons, x-rays, Auger electrons and photons. These radiations provide information about the sample, as its surface topography, composition and crystallography [MALISKA, 2003]. Furthermore, according to Maliska [2003, p. 5], the secondary electrons provide a topographic image of the surface of the sample, resulting in high resolution images. On the images generated by the backscattered electron signals a characteristic image of the composition variation is shown.

2.2 Titanium

Titanium was the material chosen for the development of additive manufacturing and micromilling tests in the present work. This metal can be found in the lithosphere in soils, rocks and running water, in the composition of various minerals such as rutile (TiO_2) and ilmenite ($FeTiO_3$), which are the two main sources for extracting this metal [FOREGS, 2018]. Titanium from both rutile and ilmenite was discovered in the mid-18th century. Ilmenite can be found in the Ilmen Mountains in Russia and rutile on beaches in Australia, India and Mexico [SANTOS, 2017].

The process of extracting this metal, known as the Kroll process, is complex and expensive, as it requires the use of inert atmospheres or vacuum, as titanium is highly reactive with oxygen [LÜTJERING; WILLIAMS, 2007]. This processing difficulty makes the titanium cost high, limiting its use in industry, even though there is a great availability of this material in nature [SANTOS, 2017]. According to Freese, Volas and Wood [2001], titanium is the fourth most abundant structural metal on earth, surpassed only by aluminum, iron and magnesium. It is also the tenth most abundant element on earth, representing 0.5% of the weight in the earth's crust [RAILSBACK, 2018].

Even with its high cost, titanium is the focus of many researches, as it is a material that has desirable properties for applications in various industries, as the aeronautics, aerospace, medical and chemical ones. Among its best known characteristics, its high strength, lightness, biocompatibility, non-toxicity, corrosion resistance and high melting point can be mentioned [LÜTJERING; WILLIAMS, 2007; ZIBEROV, 2018].

Titanium is an allotropic element, which at room temperature has a hexagonal close packed structure (HCP) , also known as α phase. Its allotropic transformation temperature is 882°C, where it transforms into a body-centered cubic structure (BCC) , or β phase [FREESE; VOLAS; WOOD, 2001].

According to Marinho [2016], commercial titanium is a complex alloy, which contains elements such as iron, carbon, nitrogen, oxygen and hydrogen, which modify its polymorphic transformation temperature, starting to occur in a range where the phases coexist. These elements (or impurities) from the Kroll process influence the metal in such a way that, for its commercialization, pure titanium is classified into grades one to four.

2.2.1 Titanium alloys

Titanium alloys are distinguished by their composition and may have different properties depending on the alloying elements present and their quantity. In this way, it is possible to manipulate the elements in an alloy to enhance a certain property. These elements can be classified as α or β stabilizers, depending on the modification they cause on the allotropic transformation temperature of titanium.

If the element increases the allotropic temperature of titanium, it is classified as α-stabilizer. Elements such as aluminum, oxygen and nitrogen are α-stabilizers, that is, the greater the amount of these elements in an alloy, the longer the α phase will be. If the element decreases this temperature, it is classified as β-stabilizer, that is, larger amounts of these elements will promote the β phase. Among the β-stabilizing elements we can mention molybdenum, iron, vanadium, chromium and manganese [FREESE; VOLAS; WOOD, 2001]. The β-stabilizer elements divide in turn into β isomorphic stabilizers (such as Mo, V, Ta and Nb) and β eutectoid (Mn, Fe, Cr, Co, Ni, Cu, Si) [MARINHO, 2016].

Thus, titanium alloys can be classified according to the alloying elements and phases as [MARINHO, 2016]:

- α **alloys**: These are single-phase alloys that presents only α stabilizers neutral elements. They are stable and have good properties at high temperatures;
- **Near** α **alloys**: Contains a small percentage of β-stabilizer alloy elements (1 to 2%). The microstructure consists of α phase with little amount of retained β phase;
- α-β **alloys**: These alloys contain 4 to 6% of β-stabilizing elements. They present good mechanical strength and they can be thermally treated to achieve different microstructures;
- **Metastable** β **alloys**: They have 10 to 15% of β-stabilizing alloying elements. The β phase is retained at room temperature in a metastable condition. These alloys contain a small amount of α-stabilizer elements, which act as hardening agents, and present high mechanical strength;
- β **alloys**: They have a high amount of β stabilizing elements (about 30%), which is the stable phase at room temperature. The β alloys are refractory metals with high density and low ductility, that are used in highly corrosive environments.

This classification is shown in the pseudo-binary isomorphous phase diagram illustrated in Figure 8. In this schematic the metastable HCP α'-martensite starts at temperature $M_{Sa'}$ and the orthorhombic α"-martensite at temperature $M_{Sa"}$. Where α'- and α"-martensite are structures resulting of martensitic transformation due to rapid cooling. The α'-martensite phase has a needle-like appearance that retains the HCP structure. The α"-martensite derives from a rhombic distortion of the α' phase, what results in a fine and metastable needled martensite. In this sense, Figure 9 represents some binary phase diagrams for titanium with different alloying elements.

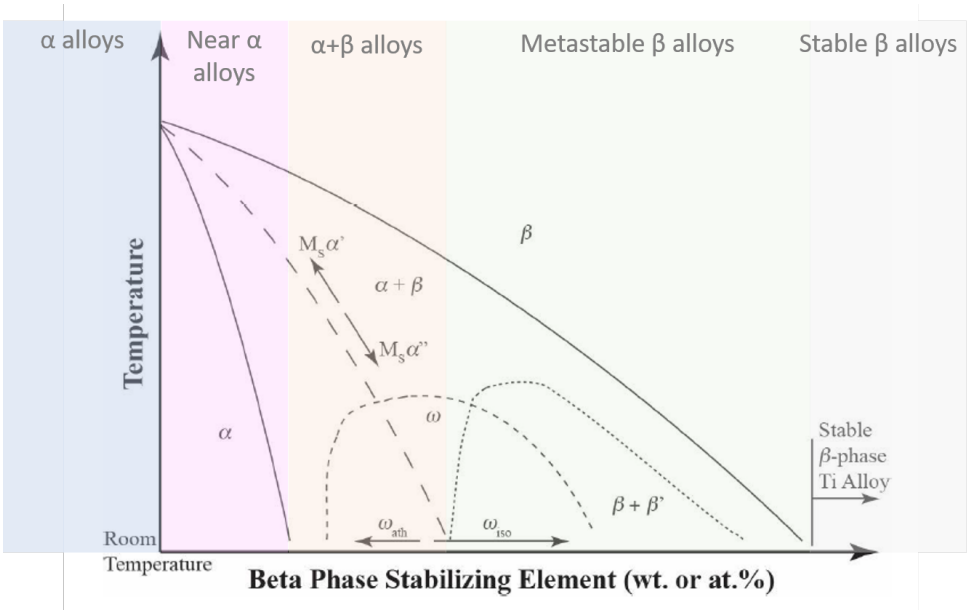

Figure 8: Schematic of a pseudo-binary isomorphous phase diagram. Adapted from: Kolli and Devaraj [2018]

Due to the wide combination possibilities among different alloying elements, many alloys were created to have excellent tensile strength, compression and creep resistance, at selected temperatures and without a complex manufacturing process [DONACHIE, 1988]. Among a variety of titanium alloys, the Ti-6Al-4V alloy is the most common and most used in the industry, as 50% of the global production of this metal is dedicated to its production [SHOKRANI; DHOKIA; NEWMAN, 2016]. This alloy is mainly applied when a higher mechanical strength is desired [DONACHIE, 1988].

2.2.2 Ti-6Al-4V Alloy Properties

The Ti-6Al-4V titanium alloy has this nomenclature because it contains 6% aluminum and 4% vanadium in its composition. This alloy is classified as a alpha-beta alloy, since aluminum is a α-stabilizer element, that is, it tends to increase the titanium allotropic

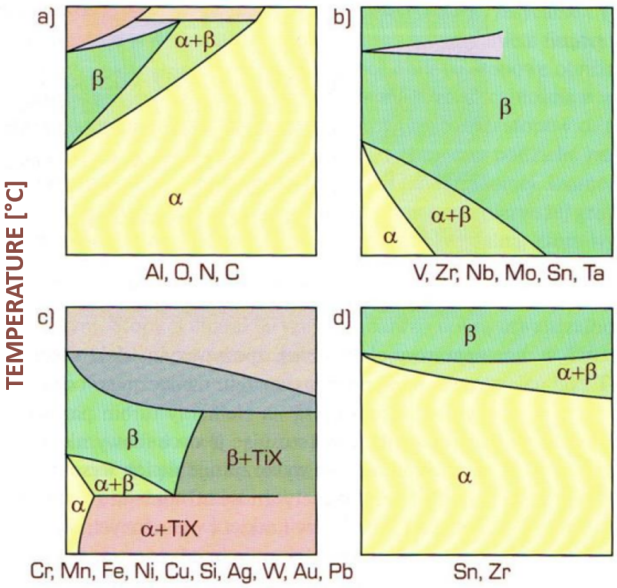

Figure 9: Titanium binary phase diagrams with different alloying elements. Source: Dobrzański (2009 apud MARINHO, 2016)

transformation temperature, promoting the α phase. Although, Vanadium is a β-stabilizer element and it tends to decrease the titanium allotropic transformation temperature, promoting the β [FREESE; VOLAS; WOOD, 2001] phase. Alloys that support both phases simultaneously present improved physical properties if compared to alloys with the presence of a single phase [ACE, 2015].

Table 1 shows in detail the chemical composition of a conventional Ti-6Al-4V alloy.

Table 1: Chemical composition of conventional Ti-6Al-4V alloy (grade 5). Adapted from: AMIT et al. [2015]

Titanium	**Aluminum (Al)**	**Vanadium (V)**	**Iron (Fe)**	**Oxygen (O)**
89,75 %	6 %	4 %	0,25 % (max.)	0,2 % (max.)

Table 2 shows a comparison between pure titanium and Ti-6Al-4V alloy properties at room temperature. As it can be seen, the addition of aluminum and vanadium to titanium improves some of its properties. It can be noted that, for the Ti-6Al-4V alloy, the Rockwell hardness triples, the ultimate tensile strength and the fracture strength are around four times higher and the maximum operating temperature doubles if compared to pure titanium. On the other hand, the Young's modulus, ductility and thermal conductivity of the alloy are reduced.

Table 2: Properties of pure titanium and Ti-6Al-4V alloy. Adapted from: Jaffery et al. [2015]

Property	**Material**	
	Ti	Ti-6Al-4V
Density (g/cm_3)	4,5	4,42
Hardness (HRC)	10-12	30-41
Ultimate tensile strength (MPa)	220	950
Fracture strength (MPa)	140	880
Young's modulus (GPa)	116	113,8
Ductility (%)	54	14
Thermal conductivity ($W/(m.K)$)	17	6,7
Maximum operating temperature (°C)	150	315

In Figure 10a, the microstructure of the Ti-6Al-4V alloy is shown and its different phases are pointed out, where the lighter part indicates the hard α phase and the darker part indicates the β phase. However, this alloy can present different types of microstructures, depending on its chemical composition, processing and heat treatments [MARINHO, 2016]. Figure 10b shows the Ti-6Al-4V alloy highlighted in a pseudo-binary isomorphous phase diagram.

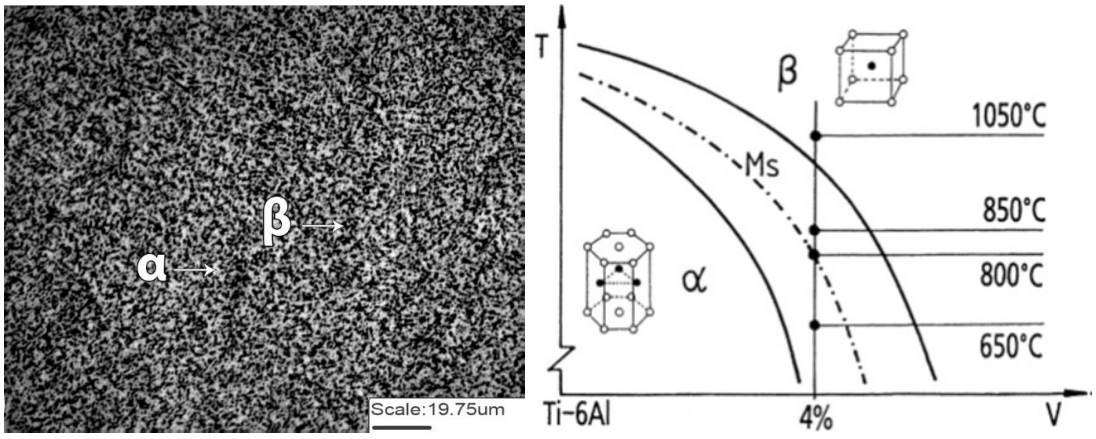

(a) (b)

Figure 10: (**a**) Ti-6Al-4V titanium alloy microstructure with α and β phases highlighted (**b**) Ti-6Al-4V alloy highlighted in a pseudo-binary isomorphous phase diagram. Source: Fedrigo and Junior [2017] and Ducato et al. [2013]

When cooling the alloy above the allotropic transformation temperature in an extremely slow rate, the stable β phase (BCC) becomes a globular type of the α phase (HCP). This behavior can be noticed on the experimental Continous Cooling Transfor-

mation (CCT) diagram obtained by [DABROWSKI, 2011] shown in Figure 11 . As the cooling rate increases, the α phase nucleation rate also increases and the diffusion process is reduced, which results in the formation and growth of α grains inside the β grains. On the other hand, for very high cooling rates, as in quenching processes, the β phase is partially or completely transformed, depending on its composition, into microstructures of the type α' (compact hexagonal) or α" (orthorhombic structure) [PEDERSON, 2002].

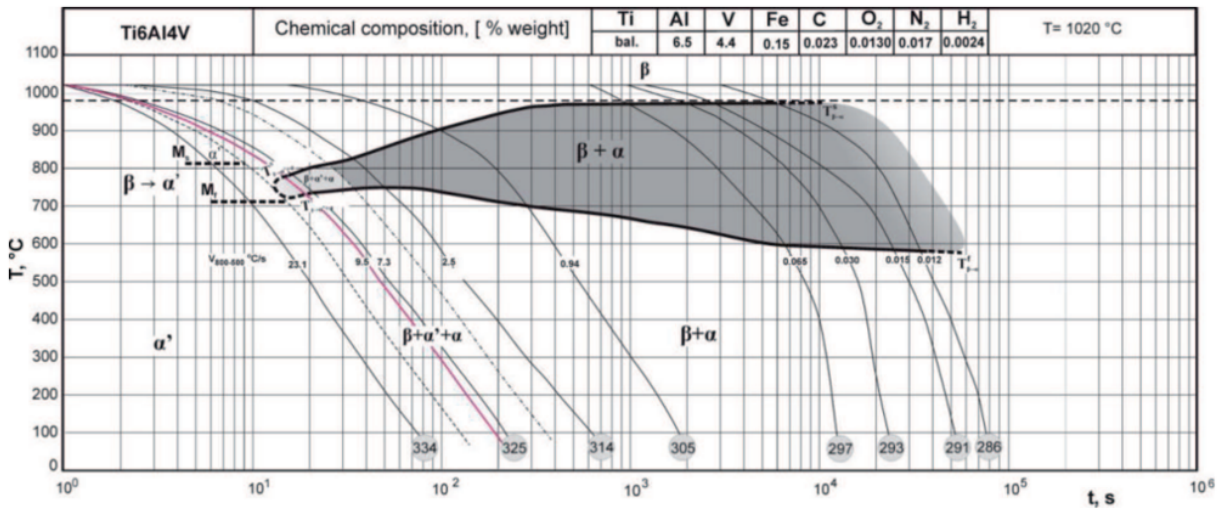

Figure 11: CCT diagram for Ti-6Al-4V alloy. Source: Dabrowski [2011]

For the Ti-6Al-4V alloy, some of the common microstructures that can be obtained through different types of processing are presented in Figure 12, as presented in the work of Attanasio et al. [2013]. According to the authors, the bimodal microstructure presents equiaxed α grains in a lamellar matrix $\alpha + \beta$, and it presents a good combination of mechanical properties. The equiaxed microstructure presents good ductility due to the reduction of the lamellar matrix. Both the bimodal and equiaxial microstructure are results of recrystallization processes. Finally, the lamellar microstructure, resulting from cooling at a rate of approximately 5°C/min, is a microstructure that has low ductility and, according to the experiments carried out by the authors, has a lower hardness.

In general, titanium and its alloys are known to be difficult materials to machine by traditional methods, as their low thermal conductivity provides an temperature increase at the tool-workpiece interface. Furthermore, at high operating temperatures, titanium is chemically reactive with most materials used for cutting tools, it means that the tool and workpiece tend to bond/melt during machining. Titanium also has a low modulus of elasticity, which can interfere on the tool-workpiece contact during machining [AMIT et al., 2015].

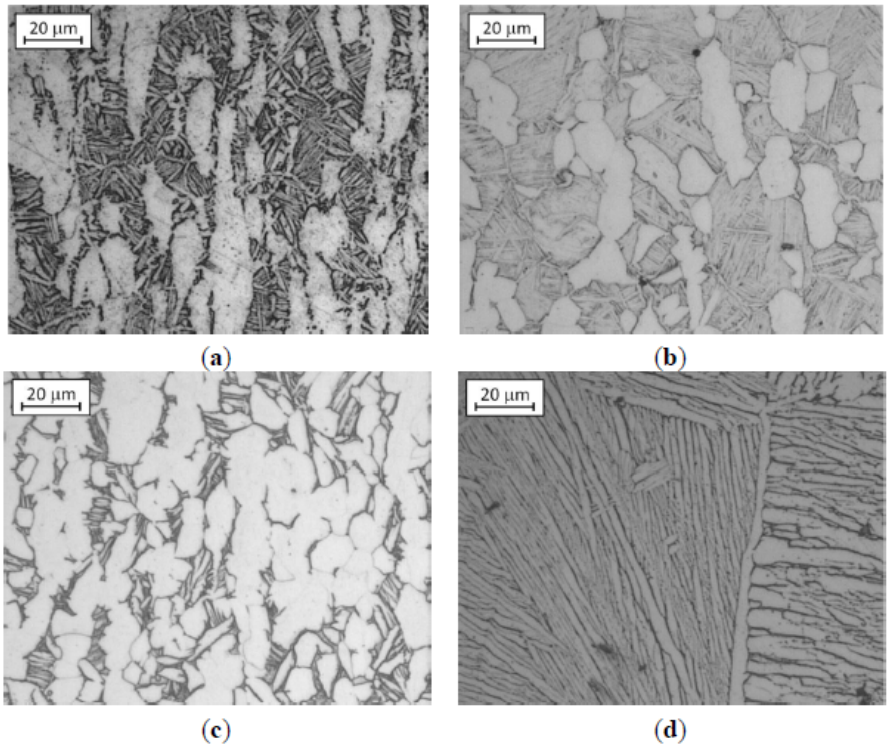

Figure 12: Common microstructures for Ti-6Al-4V alloy: **(a)** Conventional annealed alloy, **(b)** Bimodal, **(c)** Equiaxial and **(d)** Lamellar. Source: Attanasio et al. [2013]

2.2.2.1 Properties of Ti-6Al-4V alloy printed by LPBF

Regarding the properties of the material printed by LPBF, the ASTM 3001/14 standard establishes the minimum requirements for Ti-6Al-4V alloy components manufactured by additive manufacturing. It includes their chemical composition, microstructure and mechanical properties. The chemical composition required for the Ti-6Al-4V powder is shown in Table 3.

Table 3: Chemical composition required for the Ti-6Al-4V powder (wt%). Source: American Society for Testing and Materials [2014]

Ti	**Al**	**V**	**Fe**	**O_2**	**N_2**	**H_2**	**C**	**Y**
Balanced	6,5	4,5	<0,25	<0,13	0,05	0,012	0,08	0,005

The properties of components produced with additive manufacturing are regulated by ASTM 3302/18. The mechanical properties required for Ti-6Al-4V grade 5 and Ti-6Al-4V ELI alloys are presented in Table 4. Regarding the difference between these alloys, the alloy Ti-6Al-4V-grade 23 ELI presents high purity because it presents a reduced amount of interstitial elements. Therefore, it has better corrosion resistance and toughness than a grade 5 alloy, making it ideal for medical and biomedical applications [LKALLOY,

2020]. Thus, comparing the properties of the alloy obtained by rolling and by additive manufacturing via SLM (Tables 2 and 4), it is noted that the fracture strength does not undergo major changes regardless of its means of production (range of 860-895 MPa).

Table 4: Required mechanical properties for Ti-6Al-4V components manufactured via PBF. Source: American Society for Testing and Materials [2018]

Alloy	**Fracture strength [MPa]**	**Yield strength (0,2% offset) [MPa]**	**Elongation [%]**	**Área reduction [%]**
Ti-6Al-4V	895	825	10	15
Ti-6Al-4V ELI	860	795	10	25

Regarding the microstructure, Yang et al. [2016] made an extensive study of the Ti-6Al-4V alloy microstructure printed by LPBF. In their experiments, the authors observed the formation of α'-martensite in the microstructure from the SLM process, which is a characteristic of the rapid cooling of this process. According to the authors, the β phase (BCC) of the alloy is completely transformed into the hexagonal close-packed metastable phase α' martensite by a diffusionless transformation. Because of this, the resulting microstructure consists of extremely fine α' martensites with columnar β grains. This behavior can be seen in Figure 13. The columnar beta grains of this material favor intergranular failure. The material also has high strength and its thin martensites with tight spacing can prevent dislocations motion, resulting in low ductility.

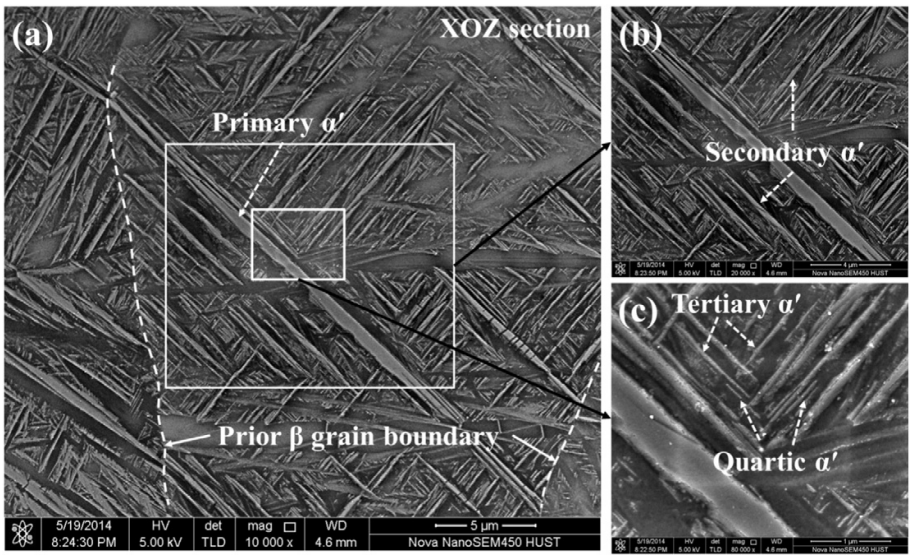

Figure 13: SEM images of a LPBF printed Ti-6Al-4V alloy with zoom in the indicated areas. Source: Yang et al. [2016]

2.2.3 Titanium α case layer

Titanium and its alloys forms a thin hard and brittle oxide layer when it comes into contact with air, this is known as α case layer. This layer damages several material's mechanical properties and lowers its tensile ductility and fatigue resistance [GADDAM et al., 2013]. For this reason, in manufacturing processes that use titanium and its alloys, it is necessary to control the manufacturing atmosphere, as titanium is highly reactive with carbon, nitrogen and, mainly, oxygen [LÜTJERING; WILLIAMS, 2007]. Therefore, inert atmospheres or vacuum are necessary for titanium melting processes, as is the case of LPBF.

According to Marinho [2016], the α case layer is an "oxygen enriched phase that occurs in titanium and its alloys when exposed to high temperatures and oxidizing atmospheres". It occurs by the diffusion of the interstitial solid solution of oxygen, carbon or nitrogen into titanium. If this oxide film forms, its removal is not a simple process, because this thin layer is consistent and stable, making titanium resistant to many reagents. In some cases, chemical pickling is applied and hydrofluoric acid or a mixture of hydrofluoric and nitric acid can be used [ACE, 2015].

2.3 Machining

The following subsections address a review of the process outcomes studied in this work: cutting forces, surface roughness, residual stress, tool wear and burr formation.

2.3.1 Cutting forces

Studying the machining forces is important for the material removal processes comprehension and for designing proper machines and tools. From the cutting forces it is possible to determine the energy consumed in a process, to describe the machinability of a part and to better choose the machining parameters [BALDO, 2013; DIB; DIAS; JASINEVICIUS, 2017]. The amplitude and direction of cutting forces in a machining process is influenced by depth of cut, feed rate, cutting speed, specimen material, tool material and geometry, and cutting fluid usage [ALTINTAS, 2012].

As stated by Altintas [2012] and Araujo, Mougo and Campos [2021] the machining forces are defined as the action of the part on the tool over a certain period of time, which allows the removal of material. Altintas [2012] punctuates that even though the

most common machining operations are a three-dimensional process, the two-dimensional orthogonal cutting case is used to explain the general mechanics of metal removal. Furthermore, despite the forces acting on an area, it is considered, for simplicity, that the forces act on a point.

In orthogonal cutting, the material is removed by a cutting edge perpendicular to the direction of relative tool-workpiece motion, as it can be seen in Figure 14 [ALTINTAS, 2012]. The cutting is considered to be uniform along the cutting edge and the cutting forces are exerted in the directions of velocity and uncut chip thickness, which are called tangential (F_t) and feed (F_f) forces, respectively [ALTINTAS, 2012].

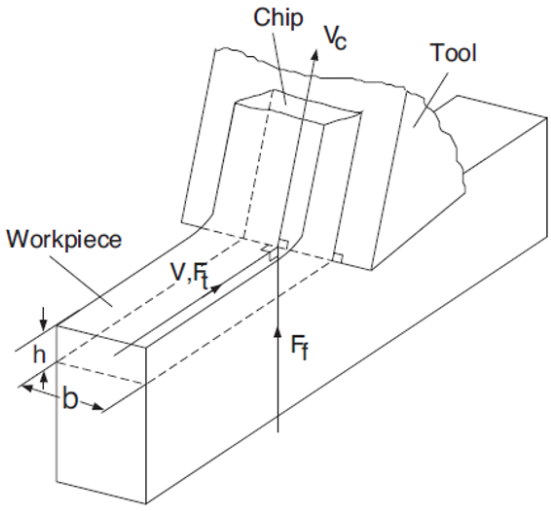

Figure 14: Orthogonal cutting process geometry. Source: Altintas [2012]

As Altintas [2012] describes in Figure 14, as the tool edge penetrates the workpiece, the material ahead of the tool is sheared over the primary shear zone, forming the chip. Thus, the chip partially deforms and moves along the rake surface of the tool, which is called the secondary deformation zone. The tertiary zone is the friction area between the flank of the tool and the finished surface. The illustration of these shear zones is shown in Figure 15a. It can be noted that the shear plane is into the primary shear zone and it is represented by the line that separates the deformed material from the material that still attached to the part. Also, the angle between the cutting speed direction (V) and the shear plane is called shear angle (ϕ_c).

In the force model presented by Altintas [2012], all forces acting on the tool are due to the shearing process or due to chip and rake face contact. The cutting forces acting on the cross section of the orthogonal cut are shown in Figure 15b. The resultant force (F_c) acting on the tool tip is formed by the feed force, which acts in the feed direction, and by the tangential cutting force, which acts in the direction of cutting speed, both

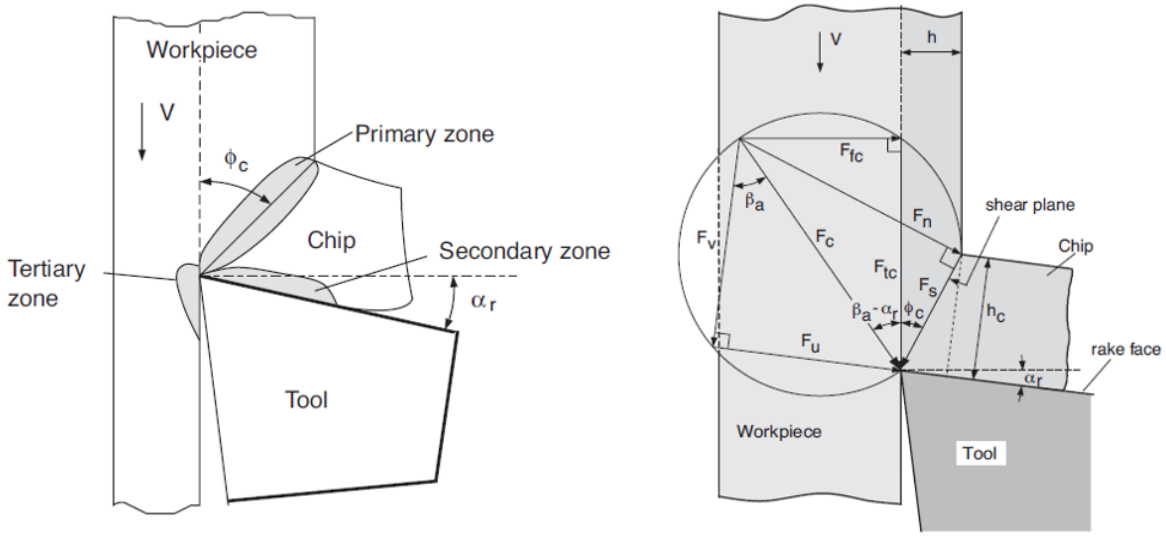

Figure 15: **(a)** Contact zones during cutting and **(b)** Cutting force diagram. Source: Altintas [2012]

are denoted by Altintas [2012] as F_{fc} and F_{tc}, respectively. From force equilibrium, the resultant force (F_c) is given by:

$$F_c = \sqrt{F_{fc}^2 + F_{tc}^2} \tag{2.1}$$

From the geometry presented in Figure 15b, it is possible to find the shear (F_s) and normal (F_n) forces, acting on the shear plane, given by:

$$F_s = F_{tc}cos(\phi_c) - F_{fc}sin(\phi_c) \tag{2.2}$$

$$F_n = F_{tc}sin(\phi_c) + F_{fc}cos(\phi_c) \tag{2.3}$$

Furthermore, the frictional (F_u) and normal (F_v) forces, acting on the rake face of the tool, are given as a function of the rake angle (α_r) by:

$$F_u = F_{tc}sin(\alpha_r) + F_{fc}cos(\alpha_r) \tag{2.4}$$

$$F_v = F_{tc}cos(\alpha_r) - F_{fc}sin(\alpha_r) \tag{2.5}$$

End mills with helical flutes (Figure 16), like the ones used in this work, are often applied to make cuts with greater depths and small widths, as they damp sharp variations of the milling forces, presenting better tool life than non-helical mills [YOUSSEF; EL-HOFY, 2008]. In this illustration, the shear forces acting on infinitesimal elements in the axial, radial and tangential directions are denoted, respectively, by $dF_a(\psi)$, $dF_r(\psi)$

and $dF_t(\psi)$. Another illustration for the shear forces acting in one infinitesimal element is shown in Figure 17. From this illustration, it is possible to visualize the geometry of the chip formation process during milling and to note that in helical mills, the chip load gradually increases with its helix. Furthermore, up and down milling are distincted in Figure 18.

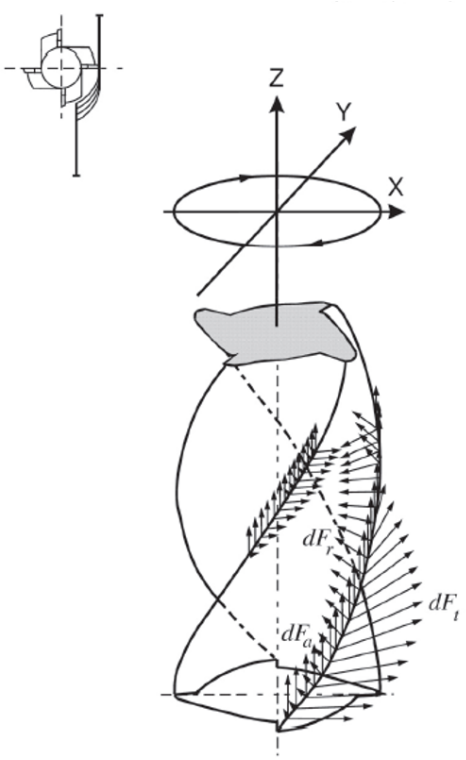

Figure 16: Helical end mill geometry. Source: Altintas [2012]

In milling process, chip thickness is dependent on the cutter rotation angle (denoted by Shi et al. [2019] as ψ in Figure 17), varying periodically with it. The angles denoted by ψ_{en} and ψ_{ex} in Figure 17 represent the entry and exit angles of the tool, where cutting process begins and ends, respectively. Therefore, the chip thickness for the milling process, where c is the feed rate, is given by:

$$h(\psi) = c \cdot sin(\psi) \tag{2.6}$$

The axial ($F_a(\psi)$), radial ($F_r(\psi)$) and tangential ($F_t(\psi)$) shear forces for the milling process can be expressed for infinitesimal elements as a function of chip removed area and

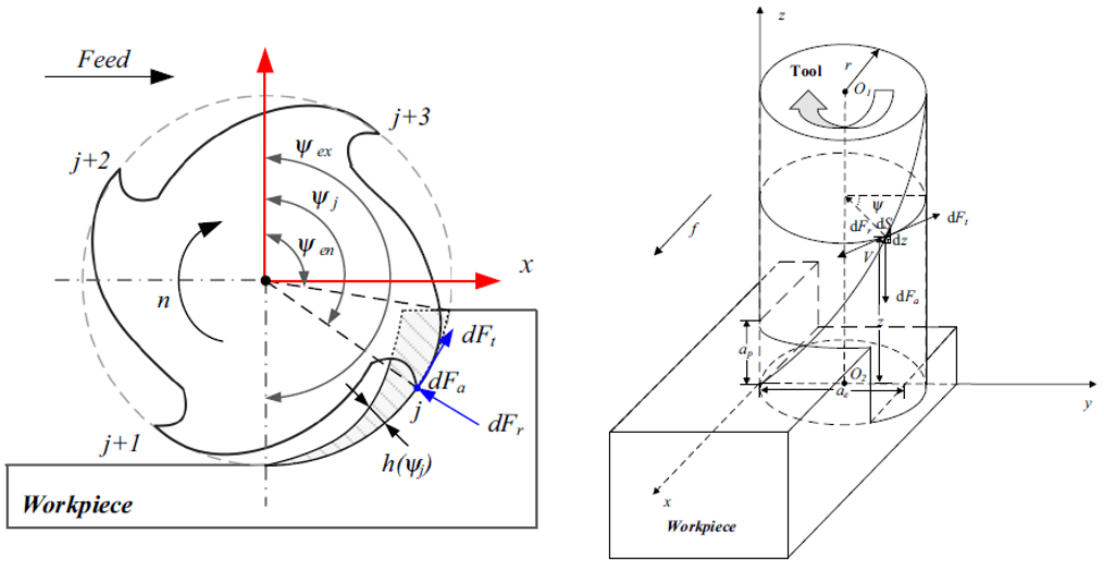

Figure 17: Machining force components and chip geometry in milling. Source: Shi et al. [2019]

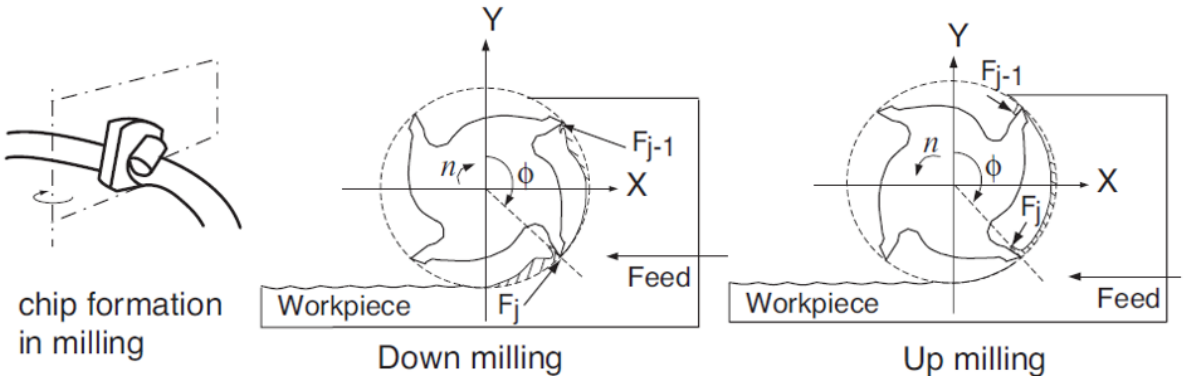

Figure 18: Up and down milling processes. Source: Altintas [2012]

infinitesimal cutting depth (dz) as:

$$\begin{cases} dF_a(\psi) = K_{ac}h(\psi)dz + K_{ae}dz \\ dF_r(\psi) = K_{rc}h(\psi)dz + K_{re}dz \\ dF_t(\psi) = K_{tc}h(\psi)dz + K_{te}dz \end{cases} \tag{2.7}$$

where K_{ac}, K_{rc} and K_{tc} are the specific cutting forces related to shear cutting in the axial, radial and tangential directions, and K_{ae}, K_{re} and K_{te} are cutting edge constants [ALTINTAS, 2012]. All these coefficients can be obtained through milling tests, which allows the calculation, through the integration of the infinitesimal forces of the cutting edge at

the analyzed time instant, of the forces in each direction represented in the Figure 16:

$$\begin{cases} F_x(\psi) = -F_t cos(\psi) - F_r sin(\psi) \\ F_y(\psi) = F_t sin(\psi) - F_r cos(\psi) \\ F_z(\psi) = F_a \end{cases} \tag{2.8}$$

These components are greater than zero when the tool is cutting, that is, between ψ_{st} and ψ_{ex}.

As addressed by Youssef and El-Hofy [2008, p. 371, ch. 10], "empirical values for estimating the cutting forces are no longer sufficient to reliably establish the optimum machining conditions". Therefore, using equipment such as a dynamometers to measure machining forces became a common practice in several studies. Monitoring cutting forces allows a more efficient control of the expected results, as they can give a spectrum of tool wear conditions, surface roughness and process efficiency [BALDO, 2013].

2.3.2 Surface roughness

An important attribute of a product is its roughness. It plays a crucial role in the component functionality and also in its aesthetics. Roughness can be defined as a set of small microgeometric irregularities, that is, small bumps and recesses, left on the surface of a piece, resulting from contact with another surface [BALDO, 2013]. In the case of microparts, surface roughness has an important influence on their functionality and the fact that the part can be smaller than a millimeter represents a great measurement challenge [MOREIRA, 2012].

To assess the roughness of a part many parameters and measurement methods have been developed. These parameters can be divided into roughness measurements made in two or three dimensions. Despite the ease of measuring 2D parameters, their applications are limited, as their values cannot be used to characterize a surface [SEIKA; KOWALSKI, 2014]. 3D measurements are more reliable and representative, so they were used in this dissertation to study the printed and machined surface.

Thus, the roughness parameters can be classified into amplitude, spacing or hybrid parameters [RODRIGUES; JASINEVICIUS, 2020]. Amplitude parameters are related to the distance between peaks and valleys in a vertical direction and are most often used to describe a surface. The spacing parameters, on the other hand, indicate the horizontal distance between the peaks and valleys. Lastly, the hybrid ones present the slope angle

of the protrusions [RODRIGUES; JASINEVICIUS, 2020].

The most commonly used amplitude parameter to describe the roughness of a surface is its roughness average, as it is applicable to most manufacturing processes and is easy to measure. In two dimensions, the roughness average represents the arithmetic mean height of a line within the total evaluation length (Figure 19a), given by R_a. On the other hand, its expansion to three dimensions gives rise to the arithmetical mean height of an area (S_a), which is represented in Figure 19b. This parameter has the disadvantage of not considering the spacing of the profile. So, it does not allow the distinction between peaks and valleys on the surface, and it does not identify atypical peaks and/or valleys [BALDO, 2013].

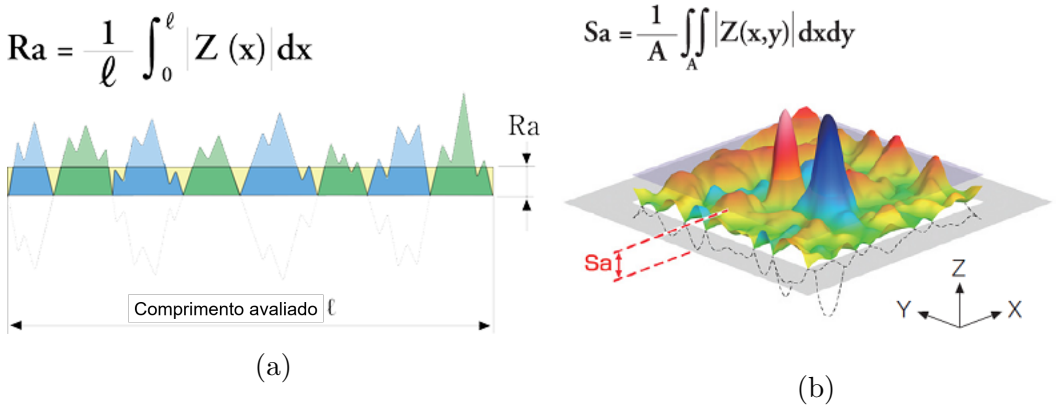

Figure 19: **(a)** R_a profile representation and **(b)** S_a profile representation. Source: Olympus [2021]

According to Farias [2009], to perform an analysis on a surface, one should not consider only the arithmetic mean deviation parameter (S_a) to indicate its functional capacity. Despite the wide application and good statistical significance of this parameter, it needs complements to assign a functional meaning to its values [WAIKAR; GUO, 2008].

Among other roughness parameters that can be analyzed to enrich the measurement, the maximum height of peaks (S_p) and the maximum depth of valleys (S_v) can be mentioned. They represent the distance from the midplane of the highest peak and lowest valley, respectively. Furthermore, the maximum height parameter (S_z) represents the distance between the highest peak and the deepest valley in the analyzed area. The illustration of these three roughness parameters is shown in Figure 20.

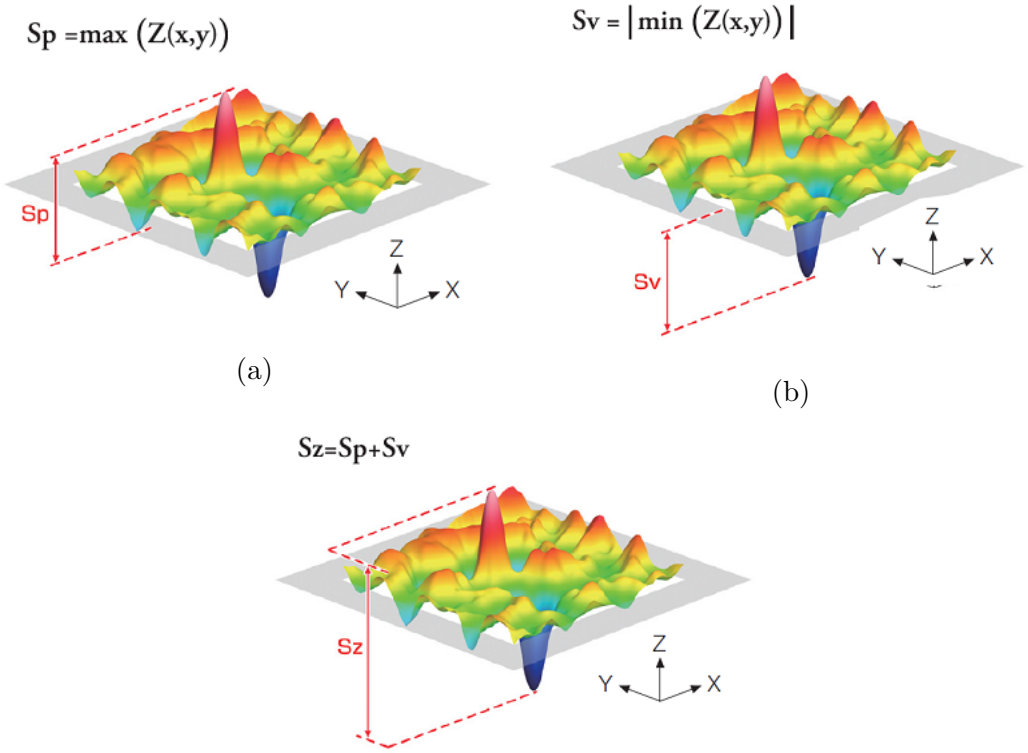

Figure 20: **(a)** S_p roughness, **(b)** S_v roughness and **(c)** S_z roughness. Source: Olympus [2021]

The skewness S_{sk} and kurtosis S_{ku} parameters are considered statistical parameters and they are related to the height distribution and to the peaks and valleys tip geometry, respectively [RODRIGUES; JASINEVICIUS, 2020; OLYMPUS, 2021]. A visual representation of their values influence on the surface profile is shown in Figure 21. In addition, the characterization of these and other parameters frequently applied in surface roughness measurements is defined according to ISO 25178 and ISO 4287 standards.

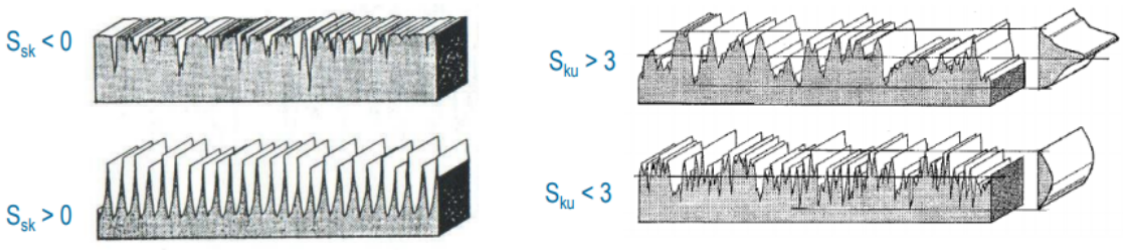

Figure 21: Surface profiles according to a variation on S_{sk} and S_{ku} values. Source: Rodrigues and Jasinevicius (2020 apud MUMMERY, 1992)

Seika and Kowalski [2014] and Silva [2004] reviewed the roughness parameters and their representations and use in surface analysis. From it, they pointed out:

- Since S_a is an average value, it cannot represent the punctual roughness profile;
- S_q is more sensitive than S_a to large height variations;
- A negative S_{sk} represents a predominance of valleys, and a positive S_{sk} a predominance of peaks;
- S_{ku} values above 3 represents a large concentration of amplitudes. Values below 3 indicate the absence of extreme peaks and valleys;
- The S_p, S_v and S_z parameters allow the analysis of the atypical peaks and valleys on a surface.

For measuring roughness on nanometric scales, contact-type surface roughness testers can damage microcomponents. So, it is suitable to use laser measurement systems or scanning microscopy for surface roughness measurements [BALDO, 2013]. According to Farias [2009], optical and mechanical instruments commonly used in engineering applications can take several minutes or hours to map the roughness of an area. These types of instruments become intolerable in practical applications. According to the author, optical interferometers, scanning and atomic force microscopes are fast enough to map 256×256 points in seconds.

2.3.3 Residual stress

Residual stresses (RS) are defined as the internal stresses that remain in the bodies in the absence of external load [SUGAHARA et al., 2018; WAN et al., 2017]. On a machined surface, these remained stresses are crucial on determining surface quality, as they can influence crack nucleation and material failure [BORDINASSI, 2006].

The RS can be either tensile or compressive, where tensile RS increases working tension and can lead to premature failure of the component. Although, compressive RS can increase the component's life as it acts against tensile stresses, reducing working tension, and increasing the fatigue performance of the material [BORDINASSI, 2006].

In machining processes, even though RS have an influence of thermal stresses, its origin is predominantly mechanical (LIU; BARASH, 1976 apud BORDINASSI, 2006). The RS are generated through deformation energy storage when the cutting tool passes on the surface. If the material ahead of the cutting tool presents predominantly compressive load, the cutting process will induce tensile residual stresses, due to the quick discharge of

deformation energy [BORDINASSI, 2006]. Although, predominant tensile loads generates compressive RS [KUMMAMKANDATH et al., 2020].

Regarding the RS measurements, various methods were developed for its estimation. The most common are: laser interferometry, blind-hole method and x-ray diffraction. The x-ray diffraction technique, using the $sin^2(\Psi)$ method, was applied for measuring the RS in the present work. The x-ray diffraction considers a selective reflection among certain crystallographic planes and it is described according to the Bragg's Law (BRINKSMEIER et al., 1982 apud BORDINASSI, 2006):

$$\lambda = 2d \cdot sen\theta \tag{2.9}$$

where d is the lattice parameter, θ is the refraction angle and λ is the x-rays wave-length.

Deriving Equation 2.9 it is possible to obtain the $\Delta\theta$ parameter, which represents the difference between the refraction angle of a material with RS and one without it. From that, it is possible to estimate the residual stress in a workpiece. To do so, the $sin^2(\Psi)$ method is applied. It consists on measuring the position of the diffraction peak regarding the inclination angle of the incident beam in relation to the surface of the analyzed material [TURIBUS et al., 2010]. From that relation, the residual stress can be written as:

$$\sigma = -K \cdot \lambda \tag{2.10}$$

where K is constant for the diffraction plane chosen and it is tabulated. λ is the line slope in the $2\theta \times sin^2\Psi$ graph (Figure 22), given by: $\frac{\partial(2\theta)}{\partial(sen^2\Psi)}$. The Ψ angle is formed due to the intersection of the sample's normal and the diffracting plane's normal. For each Ψ value, diffraction happens for certain lattice planes [BORDINASSI, 2006].

For the Ti-6Al-4V alloy, some works were done regarding the RS measurements. Kummamkandath et al. [2020] observed the influence of different lubrication methods on the RS results for a milling process. The authors measured the RS parallel and perpendicular to cutting direction using X-Ray Diffraction (XRD) analysis. There was no big difference on the RS magnitude considering both directions. The sample presented a compressive RS of -500 MPa on its surface that decreased with depth. Using the same XRD technique, Abboud et al. [2016] made a correlation among cutting parameters and RS results for turning Ti-6Al-4V. Their results show that RS were compressive in nature, and that machining at high feed rates enhanced compressive RS. On the same way, Sahu and And-

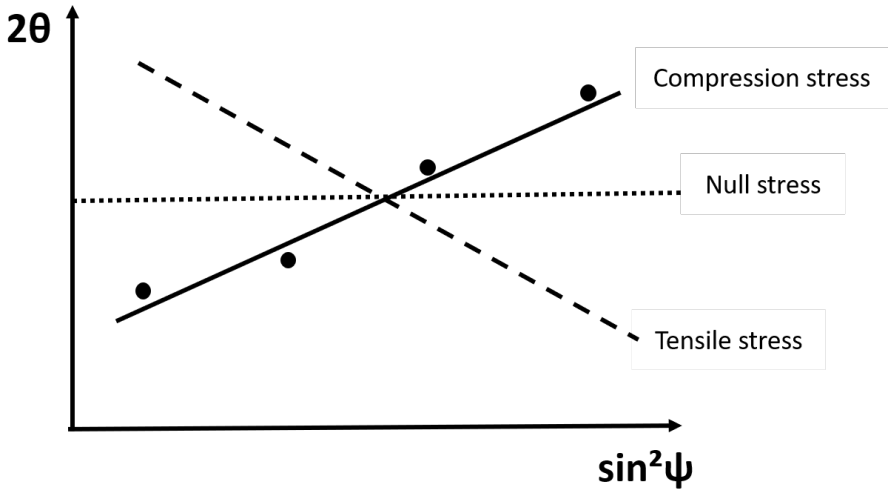

Figure 22: $2\theta \times sin^2\Psi$ graph. Source: Bordinassi [2006]

hare [2019] developed a RS prediction model for turning Ti-6Al-4V through 3D finite elements simulations. The authors also performed experiments using the XRD method, and their method error was around 11%. Their research found that the magnitude of surface compressive residual stress increases with cutting speed and depth of cut whereas it reduces with feed rate. Additionally, the RS result for the best set of cutting parameters was found to be -1495.97 MPa.

2.3.4 Tool wear

In machining processes, the cutting tool is placed under mechanical and thermal stresses, which causes it to wear and/or to damage. These damages are expected and, if wear limits are not established, they can lead to a total collapse of the tool [MARKUS, 2001]. Also, the surface roughness and cutting forces results are directly influenced by the tool wear/damage.

Some wear mechanisms are responsible for the appearance of the tool wear/damage. According to Altintas [2012], the predominance of a wear mechanism on a machining process depends on the tools, workpieces and cutting conditions used, but all of them can occur simultaneously at different rates. According to the authors, wear mechanisms can be classified into: abrasion, adhesion, diffusion, fatigue and oxidation. Below these mechanisms are detailed as presented by Altintas [2012]:

- **Abrasion:** It occurs due to friction between the workpiece and the tool. In this case, the tool, made of a harder material, generally removes the material from the

workpiece. Although, the opposite also occurs, albeit at a lower rate. In addition, the presence of hard carbides, oxides and nitrides in the tools and workpieces accentuates abrasion wear. These particles can become trapped between the part and the tool, causing additional wear;

- **Adhesion**: It happens when the softest work material (workpiece) adheres to the harder material (tool). For adhesion to occur, there must be a chemical affinity between the two materials and temperature and pressure must be in a favorable range;

- **Diffusion**: When tool and workpiece temperatures rise in the contact zones, atoms in the two materials become restive and migrate to the opposite material, where the concentration of the same atom is lower. This type of wear weakens the cutting edge and can lead to tool breakage;

- **Fatigue**: It occurs due to cyclic loading of the machining process. This type of loading, normally applied to the cutting tool, can cause it to crack or to fracture;

- **Oxidation**: It usually occurs at high temperatures and in the contact zone when the atoms present in tools and/or workpieces reacts with oxygen. Oxidation can be visually perceived, with the color change of the materials.

These five classic wear mechanisms are mainly applicable to continuous cutting operations. In the milling process, due to the intermittent nature of the cut, additional factors such as temperature cycling can influence tool wear [ALTINTAS, 2012]. Some common types of damage and wear in machining processes are illustrated in Figure 23.

The types of damage and wear shown in Figure 23 can be described as:

- **Flank wear**: The main mechanism involved in this type of wear is abrasion. It is caused by friction between the tool flank and the surface of the machined part. In this contact area, tool particles adhere to the workpiece surface and they are periodically sheared. This process intensifies at higher temperatures. Also, the abrasion of the tool flank and the machined surface augment in the presence of hard inclusions on workpiece or tool material, as the inclusions move through the contact area. The diffusion mechanism also occurs in flank wear, but adhesion and abrasion mechanisms are predominant in this type of wear [ALTINTAS, 2012];

- **Crater wear**: It is mainly caused due to abrasion and diffusion wear mechanisms. It occurs in the chip and tool contact area, where the tool is subjected to high

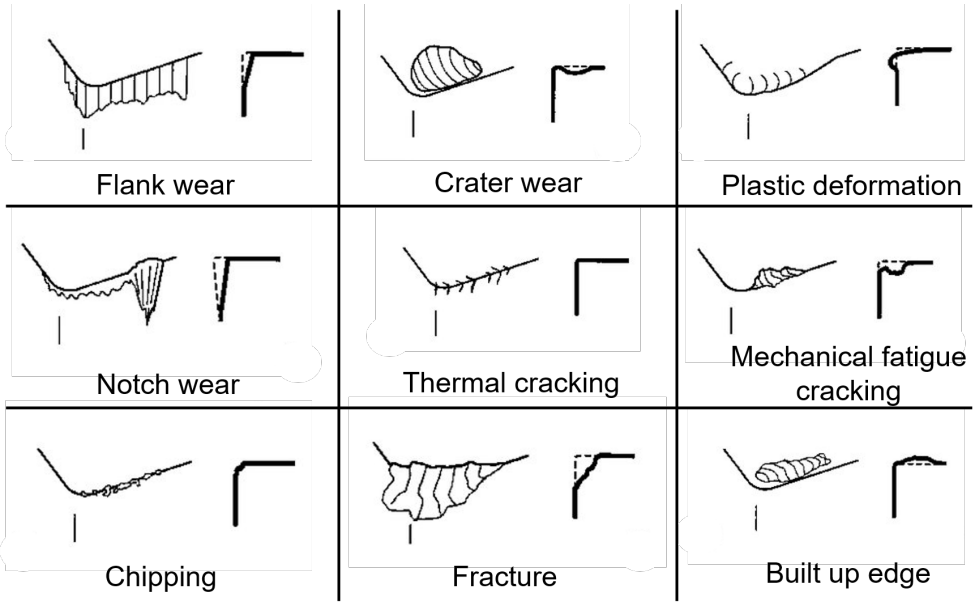

Figure 23: Cutting tools damage and wear types. Adapted from: Markus (2001 apud SANDVIK COROMANT, 1994)

frictional force caused by the moving chip. In addition, at the high temperatures and loads to which this process is subjected, the tool's atoms continually diffuse into the moving chip, intensifying the wear. Consequently, due to diffusion intensification, crater wear is bigger in higher temperatures regions. To reduce crater wear, a tool material with lower chemical affinity to the workpiece can be selected and lubricants can be also applied to reduce the process friction [ALTINTAS, 2012];

- **Plastic deformation**: At high temperatures and high cutting speeds, tools can also plastically deform. This type of failure is most common when machining metals with low machinability and heat resistant such as titanium and nickel alloys used in the aerospace industry [ALTINTAS, 2012];

- **Notch wear**: It is a special type of combined flank and rake face wear which occurs adjacent to the point where the major cutting edge intersects the work surface [BIJANZAD; KUZU; BAKKAL, 2014]. It is the result of the action of burrs produced on the edges of the chip, which have high hardness due to the high work hardening rate, favoring the adhesion and pullout of material [MARKUS, 2001]. This process occurs at the chip-workpiece-tool interface, which is subject to the oxidation mechanism and influences the formation of the notch [ALTINTAS, 2012];

- **Thermal cracking**: They appear mainly in interrupted cutting processes, such as milling. In this type of process, alternating thermal and mechanical stresses can lead to the appearance of cracks on the cutting edge, especially in tools made with

low tenacity materials. Also, it can be reduced by reducing the cutting speed or by using a tool with high thermal shock resistance [MARKUS, 2001; KÖNIG, 1990];

- **Mechanical fatigue cracking and fracture**: These damages are defined by a loss of most of the tool's wedge and it ends the tool's cutting ability [ALTINTAS, 2012]. Although, the mechanical fatigue cracking represents the loss of tool material due to the cyclic loading of the machining process. Both can be caused, for example, by not monitoring tool chipping and cracking;

- **Chipping**: It results from small particles loss on the tool edge. This malfunction is undesirable, but it does not impede the cut. It tends to occur in discontinuous cutting process, like milling, or in processes with high BUE formation. In general, chipping results in a friction increase on the tool flank, and if not identified, it can lead to fracture of the tool. Chipping can also occur when crater wear approaches the cutting edge, which weakens the wedge and causes chipping [ALTINTAS, 2012; MARKUS, 2001];

- **Built up edge**: At lower speeds, adhesion can generate a material built-up on the cutting edge. Then, this built-up material starts being the responsible for effectively cutting the material. The BUE can influence the cutting forces positively or negatively, depending on its stability and the new formed rake angle [ALTINTAS, 2012].

2.3.5 Burr formation

In order for a part to properly perform its function, finishing requirements related to its roughness and burrs are determined. Some optical, electronic, medical and biomedical applications require burr-free components. However, burrs in micromachining processes are more difficult to be removed than in conventional processes, due to their small size. Therefore, the control of burr formation in microcomponents manufacturing has a great importance [LEKKALA et al., 2011].

Burrs are the result of plastic deformation of the material under the cutting tool's action [KOU et al., 2015]. In end milling processes, burrs can occur on the edges identified in Figure 24 and the mechanism involved in their formation depends on the tool's rotation direction (up or down milling, Figure 18) . Furthermore, to measure burrs, its height and thickness are normally considered.

In Gillespie [1976]'s work on the end milling process, the author classifies burr forma-

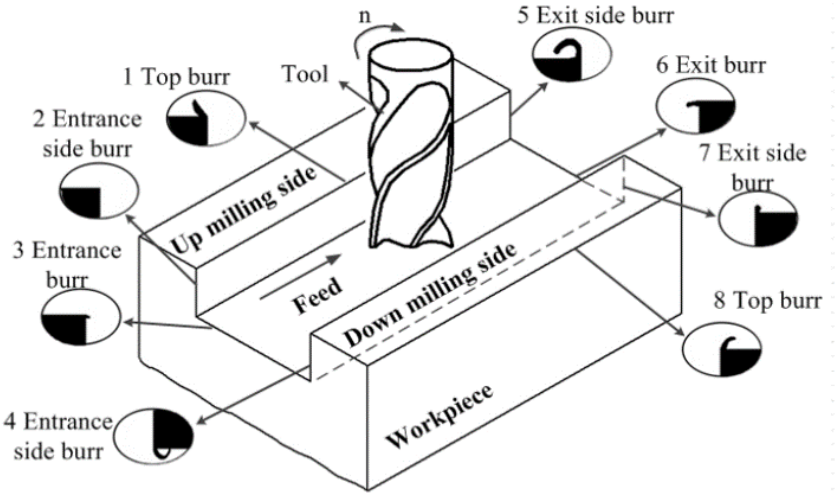

Figure 24: Types of milling burrs. Source: KOU et al. [2015]

tion mechanisms according to the edges on which they are formed. According to him, two types of mechanisms are responsible for the burr formation shown in Figure 24. On edges 4 and 5 the roll-over burrs appear. They are formed due to chip's rolling over rather than having been sheared from the workpiece. The burrs on edges 1 and 8 are the result of lateral deformation due to Poisson's ratio, known as Poisson burrs. Burrs along edges 2 and 7 are the result of material flowing 180° from cutting direction. They occur due to the entry of the tool into the material, and they are a form of Poisson burr. The burrs formed along edges 3 and 6 are a combination of Poisson and roll-over burrs [GILLESPIE, 1976] burr.

For estimating burr in a machined sample, the main geometric parameters to be considered are its height (h) and thickness (b), as illustrated in Figure 25. Burr thickness is considered the main burr dimension, as its removal process becomes more difficult when b increases [OLIVEIRA, 2015].

On burr formation in the micromilling process, Lekkala et al. [2011] carried out a study where the roll-over and Poisson burrs were observed. The most influential cutting parameters in their formation were, according to the authors, cutting depth and tool diameter. Cutting speed had a negligible effect on this process [LEKKALA et al., 2011].

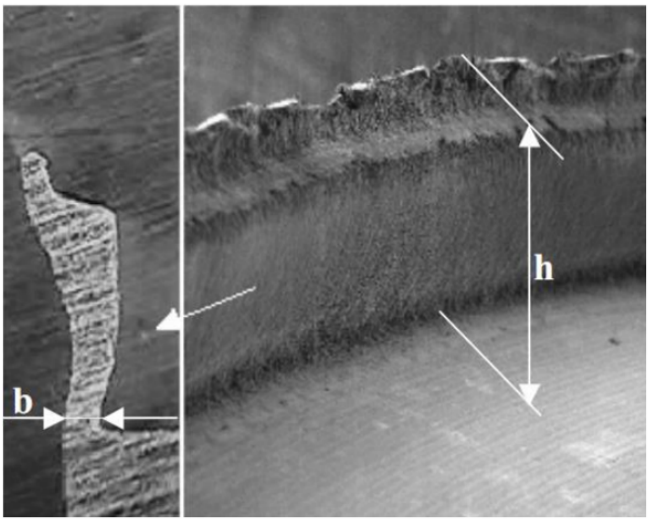

Figure 25: Burr thickness and height. Source: Machado et al. [2003]

2.4 Micromilling

2.4.1 Definition

Milling is a machining operation where the tool, with sharp edges around its axis and defined geometry, rotates in uniform motion to pull out chips [CIMM, 2018]. Thus, micromilling can be defined as a technology that aims to manufacture miniaturized features and components, deriving from a scale reduction of the traditional milling process [CUNHA, 2016]. This process has been applied in industries such as electronics, optics, aerospace, medical and biotechnology, as it allows the fabrication of complex parts in two and three dimensions, and in a wide variety of engineering materials [KURAM; OZCELIK, 2015]. Some authors, such as Jaffery et al. [2015], suggest that a milling process should be classified as micromilling if the cutting tool has a diameter smaller than 1 mm.

Despite the definition, the downscaling of a machining process is not just based on reducing the size of parts and components. When scale is reduced, the cutting dynamics become more complicated than in conventional processes. In the case of titanium alloys, for example, which have α and β grain structures, the microtool moves in between these grains causing a complicated dynamic on the tools and wear mechanisms, which are essentially different from macromachining processes [JAFFERY et al., 2015]. However, some authors point out that little research has been developed in the study of micromachining processes of titanium alloys, especially when compared to materials such as steel and aluminum [JAFFERY et al., 2015; KURAM; OZCELIK, 2015]. Therefore, there is a lack

of studies aimed at investigating the machinability, wear mechanisms, cutting dynamics and other requirements in the micromachining/micromilling process of this material.

2.4.2 Scale effect

The downscaling effects must be considered in micromachining operations, because even if the cutting parameters are proportional between the macro and micro scales, results equivalence is not guaranteed. The performance of miniaturized cutters, for example, is influenced by small vibrations and excessive forces, which can be crucial for tool life and for controlling part tolerances [CHAE; PARK; FREIHEIT, 2006].

In these processes, the chip must have a minimum thickness that takes into account the radius of the cutting edge and the material flow [GOWRI et al., 2007]. When the depth of cut does not reach a minimum chip thickness' value, no chip is formed and rubbing or burnishing takes place [JAFFERY et al., 2015]. If the chip thickness reaches a minimum value, but still smaller than the tool edge radius, the chip is formed subjected to a highly negative rake angle. This mechanism is known as *ploughing* [CUNHA, 2016]. These depth of cut influences on the chip formation can be better visualized in Figure 26.

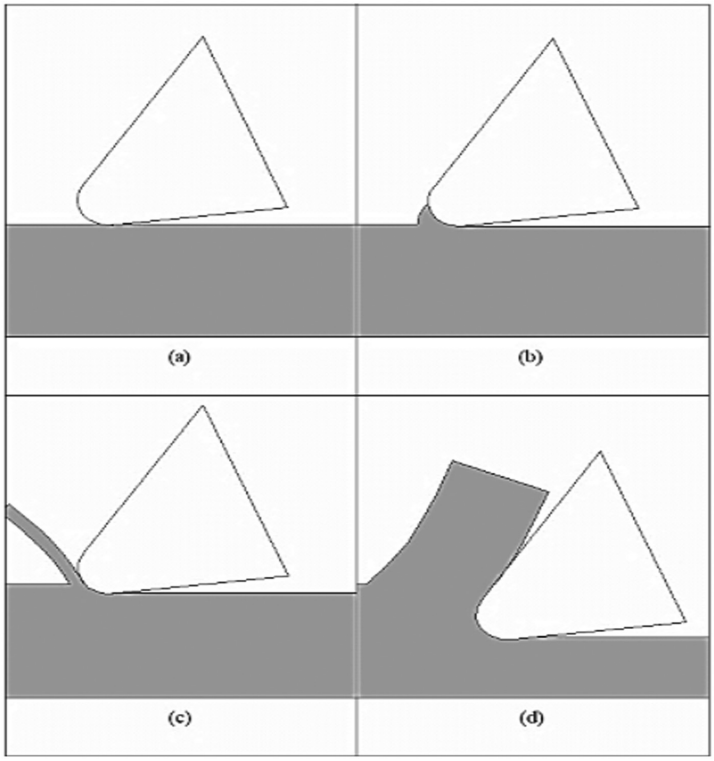

Figure 26: Mechanisms of tool-workpiece interaction for different depths of cut: **(a)** Rubbing, **(b)** Burnishing, **(c)** Ploughing (negative rake angle) and **(d)** Cutting (positive rake angle). Source: Jaffery et al. [2015]

Figure 27 shows better what happens on the burnishing and ploughing cases. It illustrates another effect that represents greater relevance in microscale: elastic deformation. During the cutting process, part of the material that comes into contact with the tool is elastically deformed and, subsequently, its elastic recovery occurs. Therefore, in order for the effective cut to happen, not only the depth of cut should be greater than a minimum value, but also the feed [GOWRI et al., 2007].

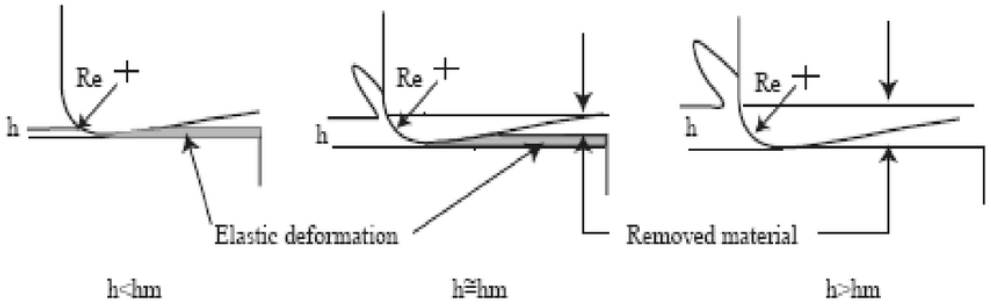

Figure 27: Schematic of the effect of the minimum chip thickness. Source: GOWRI et al. [2007]

2.4.3 Cutting parameters influence on the micromilling process

The cutting parameters directly influence the machining process and the obtained results. As Picarelli [2015] states, using higher values for the cutting parameters, such as speed, feed and depth, can increase the process productivity, but it can also lead to increased cutting forces, vibrations and tool damage. The use of parameters more conservatively, on the other hand, reduces cutting forces and other damage, but it can also lead the process to not reach the minimum chip thickness (ploughing) and reduce productivity [PICARELLI, 2015] .

In this line of research, Yun et al. [2011] proposed a method to detect the ploughing effect during micromachining. For this, the authors used the peak values variation of the cutting forces. In their experiments, performed with a 0.5 mm diameter end mill with two cutting edges for micromilling a copper sample, better surface finishing were obtained for lower feed values. However, according to Yun et al. [2011] there is a minimum feed so that the roughness of the piece is not harmed due to ploughing.

Regarding the cutting parameters' influence on the workpiece roughness, some researches reported that, in the machining of titanium and its alloys, a lower surface roughness is reached as the cutting speed increases [MOREIRA, 2012; KILICKAP; YARDIMEDEN; ÇELIK, 2017; YUN et al., 2011]. On the other hand, surface roughness increases as feed and depth of cut values increase. As observed by Moreira [2012] in their experiments,

feed was the most influential machining parameter on the roughness of a part, followed by cutting speed [MOREIRA, 2012].

Similarly, with regard to the cutting forces, higher feed values and depths of cut lead to higher cutting forces. However, at higher cutting speeds, cutting forces decrease [KILICKAP; YARDIMEDEN; ÇELIK, 2017]. Concerning chip formation, the most influential parameter is the workpiece material, but an increase in cutting speed, a reduction in feed, or an increase in rake angle tends to produce continuous chips [COELHO; SILVA, 2018]. In this topic, Coelho and Silva [2018] pointed out that feed is the cutting parameter that most influence chip formation, followed by the depth of cut.

2.5 Recent advances in Ti-6Al-4V micromachining

In literature, some studies were done analyzing the machinability of the Ti-6Al-4V alloy manufactured by LPBF, but few studies were found addressing its micromilling machinability. One of them was the work of Coz et al. [2017], which aimed to compare the machinability of titanium samples manufactured by SLM with and without heat treatment in the microturning process. To carry out the analysis, the authors used different speed and feed values for the machining process and investigated the cutting forces, morphology and formation of the chip and samples microstructure, comparing them with a conventional titanium sample.

In their conclusions, Coz et al. [2017] pointed out that, for the conditions used, the cutting forces of the SLM printed samples were 3 to 24% higher than for the conventional machined titanium samples. The authors concluded that for a cutting speed lower than 12 m/min and for a cutting thickness lower than 3 μm, there is an increase in forces and in the friction coefficient. Furthermore, as can be seen in Figure 28, the authors concluded that the chip morphologies were similar, in terms of chip segmentation and deformation, for the SLM and conventional samples. Another conclusion was that the microstructure was not particularly affected by the cutting process.

Another work that presents a study of the microstructure, chemical composition and mechanical properties of the titanium alloy Ti-6Al-4V forged and produced by SLM was made by Shunmugavel, Polishetty and Littlefair [2015]. In their work, the yield and ultimate strengths, elongation and hardness were analyzed and the effect of printing direction on these properties were considered. From the Shunmugavel, Polishetty and Littlefair [2015]'s work, it is possible to conclude that the SLM printed titanium samples

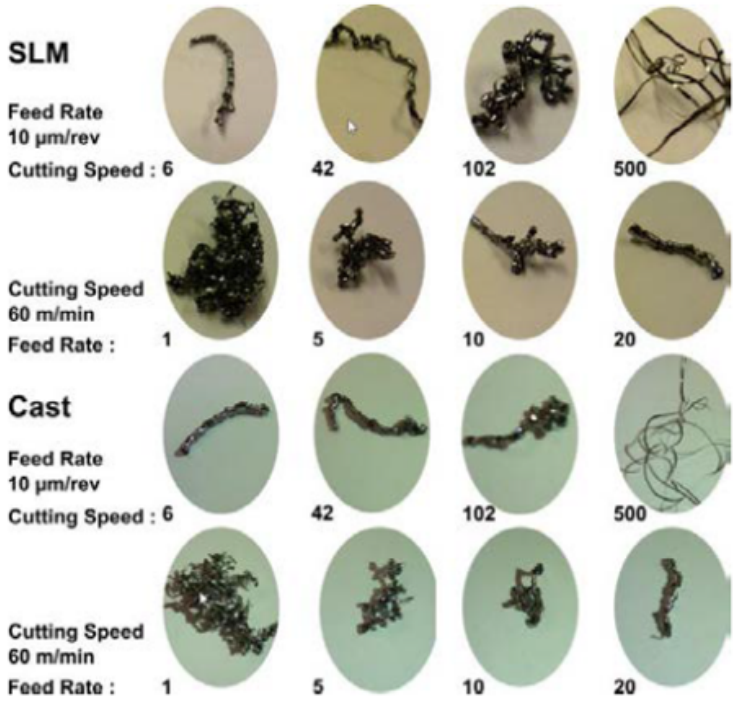

Figure 28: Chip morphology comparison when micro cutting Ti-6Al-4V cast and SLM for different feed and speeds. Source: Coz et al. [2017]

presents elongated grains, which is a result of a growth that occurs in the direction of material deposition, following its same structure and orientation. This is called epitaxial growth, and it happens because of the layer by layer printing process. On the other hand, the forged specimens presented equiaxed microstructures with elongated grains in the forging direction.

Because of this microstructural difference, the results of yield and ultimate strengths were higher for specimens printed by LPBF compared to the forged ones. Furthermore, due to the material's anisotropy, the results of the tensile tests also varied when the SLM printed specimens were tested in different directions [SHUNMUGAVEL; POLISHETTY; LITTLEFAIR, 2015]. Concerning the types of fracture, the printed specimens exhibited transgranular fractures as a result of their fragile nature. Later, Shunmugavel et al. [2017] studied the effect of microstructure and processing conditions of Ti-6Al-4V samples produced by SLM on chip formation, highlighting its morphology and segmentation during turning.

In the area of milling LPBF printed titanium, the work of Milton et al. [2016] compares the milling of SLM and hot rolled samples in regard to its roughness, cutting forces and hardness in the sub-surface of the samples. The influence of printing directions on the micromilling process was also studied. In Milton et al. [2016]'s work, for the SLM

printed specimens, few or no changes in microstructure were observed in the three different directions of the machined surfaces, unlike the hot rolled specimens, which showed changes in the microstructure after machining. Also, the printing directions of the specimens printed by SLM influenced the roughness and hardness of the sample, in addition to producing higher axial cutting forces (22% higher than the hot rolled sample), leading to greater wear and shorter tool life.

CAMPOS, ARAUJO and KAPOOR [2019] addressed the micromilling machinability of the Ti-6Al-4V alloy and pure titanium in terms of their mechanical properties, measured forces, surface roughness, top burr height, and chip morphology. In their results no significant differences in surface roughness and burr formation were found for the compared materials. In addition, both of them produced long chips for smaller feeds. Although, the Ti-6Al-4V alloy led to higher machining forces if compared to the pure metal. Another work from [CAMPOS, 2014] shows a deep study on the machining forces during the micromilling process, though performed on a 6351-T6 aluminum alloy.

Regarding the parameters used for micromilling the Ti-6Al-4V alloy, the work of Aslantas, Ekici and Çiçek [2018] aimed to optimize the cutting parameters for this process, focusing on reducing surface roughness and burr formation. According to the authors, the best result was obtained for a speed of 20000 RPM , feed of 0.25 μm/tooth and depth of 0.05 mm. Furthermore, the most influential parameter on roughness and burr formation was the depth of cut, with a contribution of 37.92% in the authors' results.

3 MATERIALS AND METHODS

3.1 Laser Powder Bed Fusion process

3.1.1 Powder characterization

To obtain a part from the Additive Manufacturing process with the desired quality and properties, it is necessary to guarantee the quality of the input material, that is, the powder used. This control is done because the chemical composition and morphology of the powder influence the fusion process, the porosity, the geometry and the final properties of the part.

Therefore, the raw material characterization methods described in Section 2.1.4 were used to ensure the quality of the material used in this work. The chemical composition analysis was performed using the X-ray fluorescence spectroscopy (XRF) technique, the average particle size was obtained using the Fraunhofer method and the Scanning Electron Microscope (SEM) was used to analyze the particle's morphology and format. These techniques and other procedures were used by Podestá [2018] in the characterization of the raw material of the samples used in this work.

For manufacturing the samples, a titanium alloy powder Ti-6Al-4V grade 23 Extra Low Interstitial (ELI) was used. The printing process was carried out on OMNITEK premises, which is a company operating in the field of industrial automation and laser systems, and works together with the Nuclear and Energy Research Institute (IPEN) developing researches in 3D printing.

The composition of the powder used for printing the samples was previously analyzed in partnership with researchers from IPEN and the results obtained are shown in Table 5. This powder composition meets the specification Ti64 ASTM F3001, which regulates the composition of the Ti-6Al-4V powder. This standard states that the powder must have between $5.5 - 6.5$ wt% of aluminum, $3.5 - 4.5$ wt% of vanadium plus other elements in smaller quantities and Ti balanced.

Table 5: Powder's chemical composition analysis XRF (wt%). Source: Podestá [2018]

Element [%]	Ti	Al	V	Fe	O_2	N_2	H_2	C
	90,2	5,8	3,75	$< 0{,}25$	$< 0{,}10\%$	0,03%	0,012%	0,08%

In addition, three morphological characteristics of the used titanium powder were determined: particle size range, density and shape. To characterize the particle size range, the particle analyzer equipment Cilas Particle Size Analyzer - Model 1064 located at IPEN was used. Using the Fraunhofer method, the powder samples were analyzed in relation to their average size. For this, four particle size parameters were measured: 10%, 50%, 90% and average particle size - D_{10}, D_{50}, D_{90} and D_{Med}. Where D_{50} represents the median of the distribution and D_{10} and D_{90} imply that, respectively, 10% and 90% of the measured particles had a diameter smaller than the presented value. The results showed that the mean particle size of the powder was 43.47 μm and its particle size distribution is displayed in Table 6.

Table 6: Particle size distribution of Ti-6Al-4V powder. Source: Podestá [2018]

Particle size [μ**m**]	D_{10}	D_{50}	D_{90}	D_{Med}
	26,68	42,41	61,77	43,47

Density analysis was performed by helium pycnometry in an AccuPyc 1330 Micromeritics pycnometer. The obtained Ti-6Al-4V powder density was $4.39 \pm 0.001\ g/cm^3$.

Regarding the particles shape, a scanning electron microscope (Philips XL30 model) was used to examine it. The powder used in this process was mainly spherical in shape, as shown in Figure 29. This spherical nature of the gas-atomized powder ensures even distribution and good flowability of the powder during the process.

Information about the performed printing process, including power, laser diameter, scan speed, tools, and other information is covered in the following subsection.

3.1.2 Printing process

Samples were manufactured via Selective Laser Melting using a OmniSint-160 printer from the Brazilian company Omnitek (Figure 30a). For this process, a protective argon atmosphere was used and a printing strategy that employs a sequential sweeping band of 5 mm and an interlayer rotation of 67° was applied. This strategy was chosen because previous tests [PODESTÁ, 2018] show that it leads to a better outcome homogeneity and

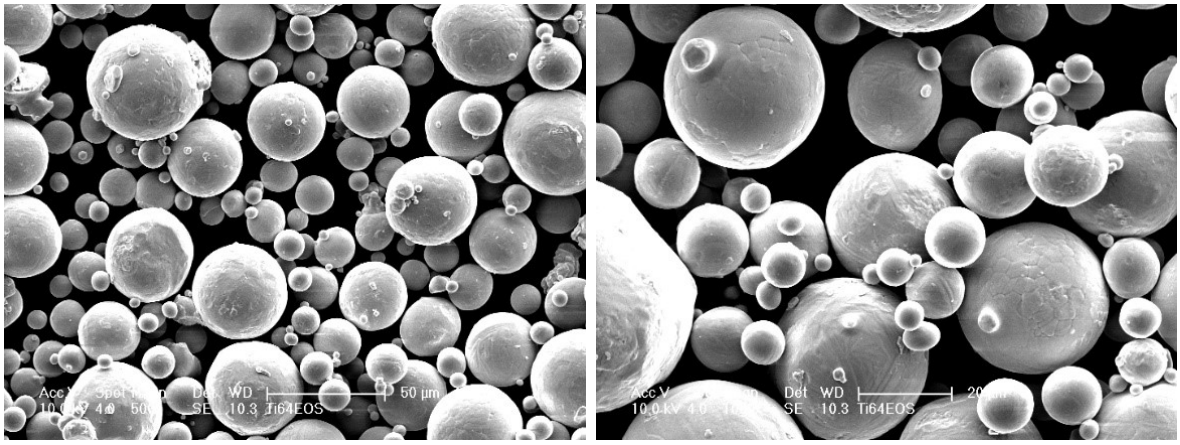

Figure 29: SEM image of the used Ti-6Al-4V powder. Source: Podestá [2018]

it approximates the most to the mechanical properties of a conventional titanium alloy. An illustration of the samples and the printing direction used is shown in Figure 30b.

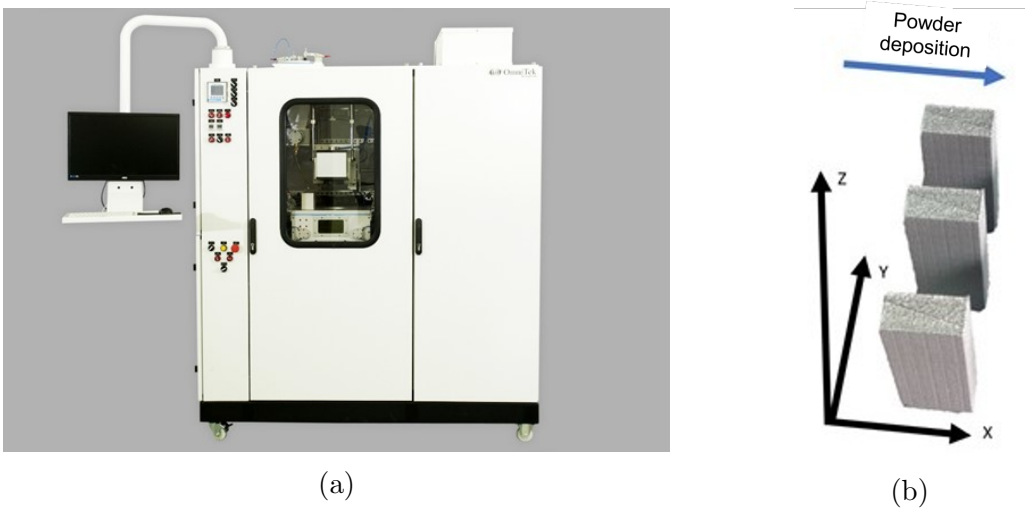

(a) (b)

Figure 30: (**a**) 3D OmniSint-160 printer. (**b**) Printed samples without heat treatment.

The LPBF equipment used has a Ytterbium fiber laser with a nominal power of 200 W and the diameter of the laser beam focus of approximately 70 μm. Regarding the parameters used for the printing process, a laser power of 155 W, scanning speed of 950 mm/s, distance between scans of 80 μm and layer thickness of 30 μm were used. The main printing parameters were arranged in Table 7. After the printing process, some samples were submitted to a heat treatment of 950°C for 60 min.

Table 7: LPBF process parameters.

Laser power [W]	**Scanning speed [mm/s]**	**Layer thickness [μm]**	**Laser diameter [μm]**
155	950	30	70

3.2 Samples characterization

After the LPBF process, the properties and anisotropy of the printed samples were analyzed by measuring its hardness and surface roughness and by examining its microstructure using the Optical Microscope (OM) and the SEM. The same procedure was followed on the conventional sample.

3.2.1 Hardness measurements

Hardness measurements were performed with the aid of a durometer and the Vickers hardness was estimated on the printed and conventional samples. For the first one, the sample was subjected to a load of 30 kgf for fifteen seconds and this procedure was repeated three times for each sample. For the second one, the same procedure was followed, except that six measurements were made and with a load of 50 kgf.

The Vickers hardness measurements performed on the printed and conventional samples are displayed in Tables 8 and 9, respectively.

Table 8: Average hardness of all three LPBF printed samples without heat treatment (Vickers Hardness, load of 30 kgf, time 15s, three repetitions)

Sample	**Average hardness [HV/30]**	**Average hardness [HRC]**
1	373.0 ± 2.73	38.1 ± 0.29
2	364.8 ± 10.66	37.1 ± 1.14
3	369.1 ± 5.36	37.6 ± 0.58
Mean	**369.1 ± 5.36**	**37.6 ± 0.42**

Table 9: Hardness measurements on the conventional Ti-6Al-4V sample (Vickers Hardness, load of 50 kgf, time 15s)

Measurement	**Average hardness [HV/50]**	**Average hardness [HRC]**
1	323.8	32.6
2	329.1	33.2
3	334.6	33.8
4	342.3	34.7
5	330.5	33.3
6	335.6	33.9
Mean	**332.5 ± 2.6**	**33.5 ± 0.3**

The hardness values are within the range found in the literature for the Ti-6Al-4V, which is from 30-41 HRC [JAFFERY et al., 2015]. It can also be noticed a small variation between the hardness averages of the different printed samples, which can be attributed to the associated measurement errors.

In addition, hardness measurements were performed by rotating the sample to verify the influence of the sample's anisotropy on the results. Thus, a variation of approximately 10% was observed in the Vickers hardness results depending on the measurement direction.

3.2.2 Roughness measurements

Before micromilling the printed samples, 3D surface roughness was measured at three different random points by optical interferometry, using a Taylor Hobson 3D CCI profilometer. The measurements were made in a scan area of 1.71×1.71 mm and considering the roughness mean of 512 profiles. Using the same equipment, 2D roughness parameters were also estimated in two different directions: one parallel to printing direction (vertical roughness) and the other perpendicular to printing direction (horizontal roughness) (Figure 31). All measurements were repeated three times in random regions for good statistical representation.

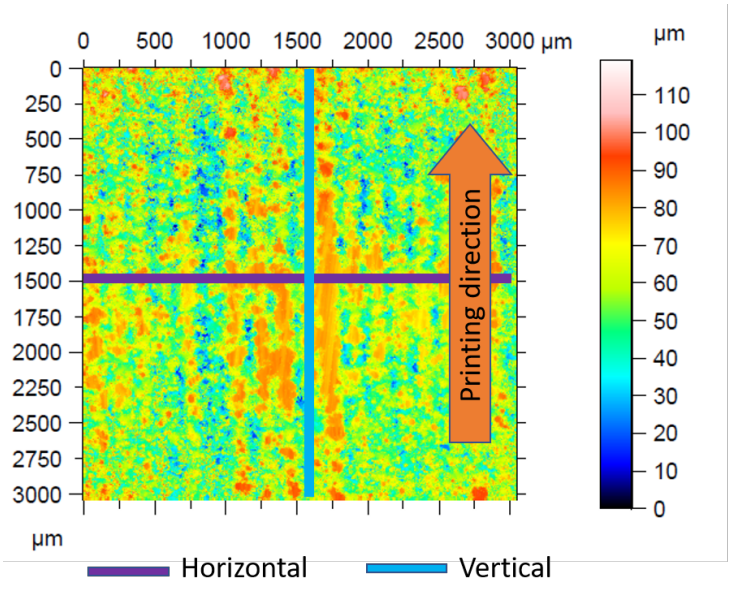

Figure 31: Considered profiles for 2D surface roughness measurements before machining.

The 2D roughness parameters measured in each sample's direction are shown in Table 10.

Table 10: Roughness parameters measured in each direction of the specimen before machining.

Parameters	**Average vertical roughness**	**Average horizontal roughness**
Ra [μ**m**]	1,43 ± 0,34	4,34 ± 0,92
Rq [μ**m**]	1,80 ± 0,42	5,34 ± 1,15
Rp [μ**m**]	3,01 ± 0,69	5,89 ± 0,64
Rv [μ**m**]	3,06 ± 0,68	7,43 ± 1,73
Rz [μ**m**]	9,30 ± 2,07	21,75 ± 4,68
Rsk	0,06 ± 0,20	-0,33 ± 0,38
Rku	3,09 ± 0,11	2,85 ± 0,08

It is possible to notice that surface roughness parameters differ according to the measured direction, due to the sample's anisotropy. From Table 10, it is observed that the highest roughness values were obtained for the horizontal profile, that is, perpendicular to printing direction. This occurs due to the waviness caused by the action of the laser, since in this direction the 2D roughness is measured overlying the cast material fillets. Thus, Figure 32 presents a comparison of these two profiles in one of the analyzed samples. Furthermore, with the Ra values obtained, the roughness of the printed samples fits into the roughness class N8/N9, according to the NBR 8404/84 [ABNT, 1984] standard.

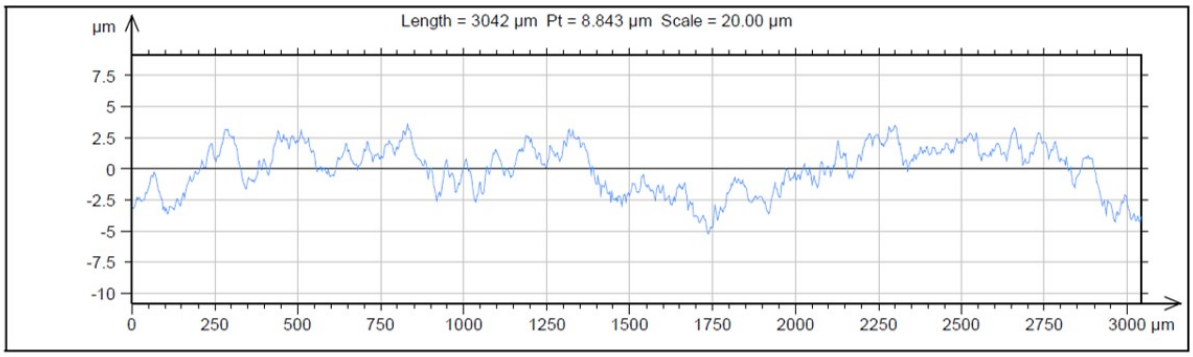

(a)

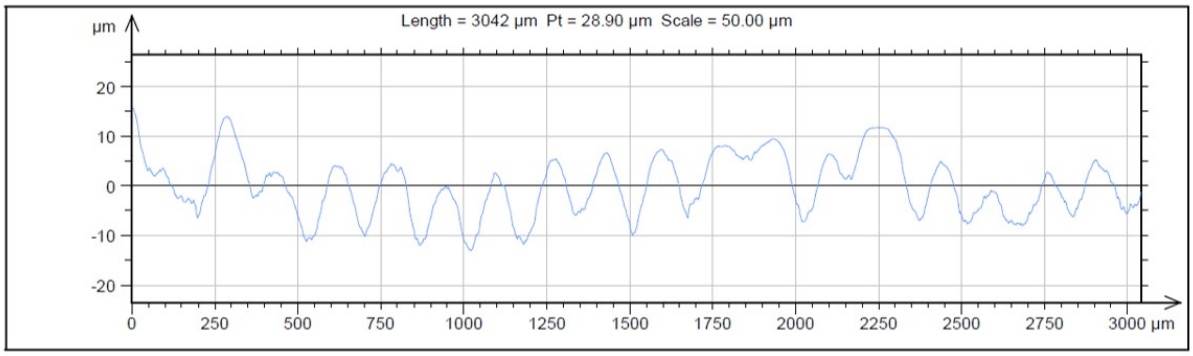

(b)

Figure 32: Roughness profiles before machining: (**a**) Parallel to printing direction (vertical) and (**b**) Perpendicular to printing direction (horizontal)

In addition, the 3D roughness parameters of the three printed samples were analyzed. Table 11 shows its results, as well as the mean between them. The 3D profiles obtained for the three analyzed samples can be seen in Figure 33. From that, it can be observed that the samples surfaces presented a similar aspect before the machining.

Table 11: 3D roughness parameters obtained for the printed samples before machining. Adapted from: Gonçalves et al. [2019]

Parameters	**Samples**			**Mean**
	1	**2**	**3**	
Sa [μm]	22,42	20,72	22,93	**22,02 ± 1,16**
Sq [μm]	28,02	25,97	29,65	**27,88 ± 1,84**
Sp [μm]	98,77	96,25	115,33	**103,45 ± 10,37**
Sv [μm]	99,65	92,14	114,30	**102,03 ± 11,27**
Sz [μm]	198,43	188,40	229,60	**205,48 ± 21,48**
Ssk	0,067	0,075	-0,075	**0,022 ± 0,08**
Sku	2,76	2,82	3,19	**2,92 ± 0,23**

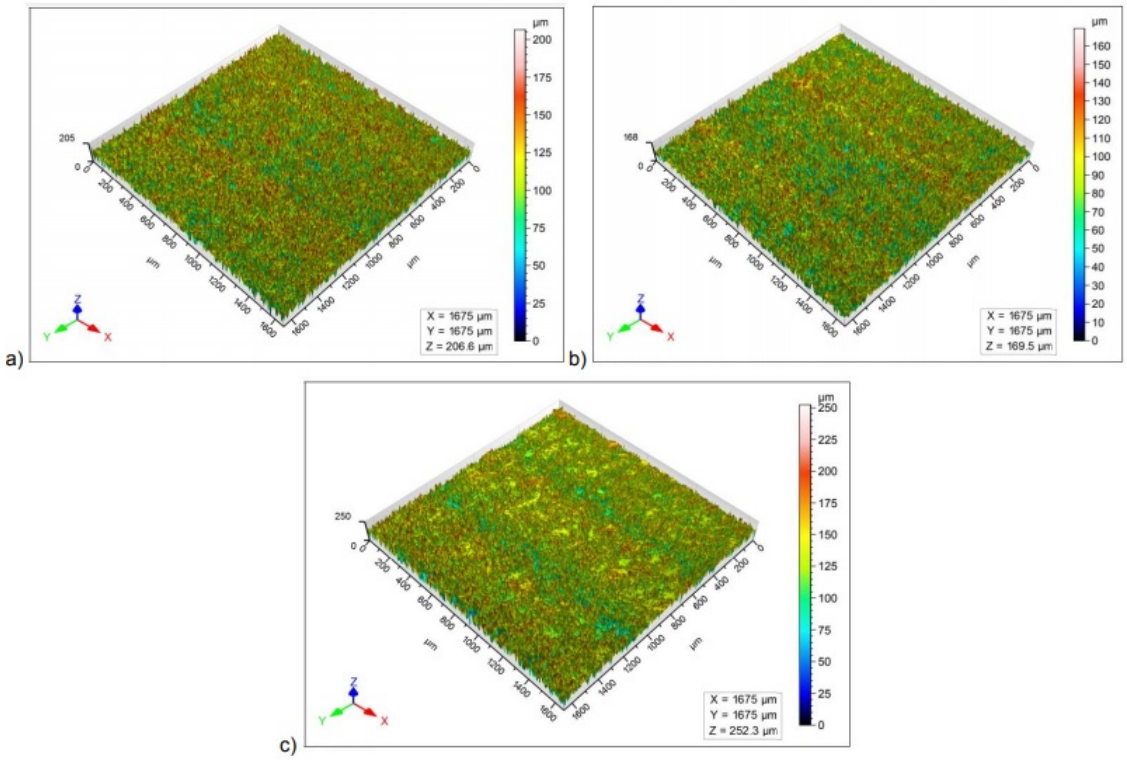

Figure 33: 3D roughness profile before machining: (**a**) Sample 1, (**b**) Sample 2 and (**c**) Sample 3. Source: Gonçalves et al. [2019]

3.2.3 Microscopy analysis

In addition to hardness and roughness measurements, a metallographic sample preparation was carried out, followed by a chemical attack with the Keller reagent for 20 seconds, in order to show the samples' microstructure. To visualize the microstructures, SEM analyzes were performed using secondary electrons (SE) and Backscattered Electrons (BSE) . Furthermore, the Energy Dispersion Spectroscopy (EDS) technique was used to map the chemical elements in the samples. The microstructural analysis was done on a printed sample and the conventional one.

From the analysis of the images obtained by Optical Microscope and SEM (Figure 34a and 35a) it is possible to observe the formation of α' martensite in the printed alloy, result of a difusionless transformation due to rapid cooling of the LPBF process. This result was also observed by Yang et al. [2016] in the microstructural analyzes of printed titanium. As stated by the authors, the presence of these thin martensites with tight spacing between them prevents dislocations motion, resulting in low ductility of the material. On the other hand, the columnar beta grains observed by the authors are not as visible in the analyzed samples, possibly due to the difference on printing strategies.

The microstructure of the heat treated samples were not analyzed in the present research, though it is expected to present betta columnar grains filled with lamellas of α + β matrix, as observed by Frkan et al. [2019] for the LPBF printed Ti-6Al-4V with heat treatment at 900°C. The fatigue life of the heat treated samples tend to be higher than the printed material without heat treatment due to its greater ductility.

For the conventional sample, the equiaxial microstructure was observed. This microstructure was characterized by the presence of α grains in a lamellar matrix $\alpha + \beta$ (Figures 34b and 35b), and it leads to a material good ductility due to a small percentage of the lamellar matrix [ATTANASIO et al., 2013].

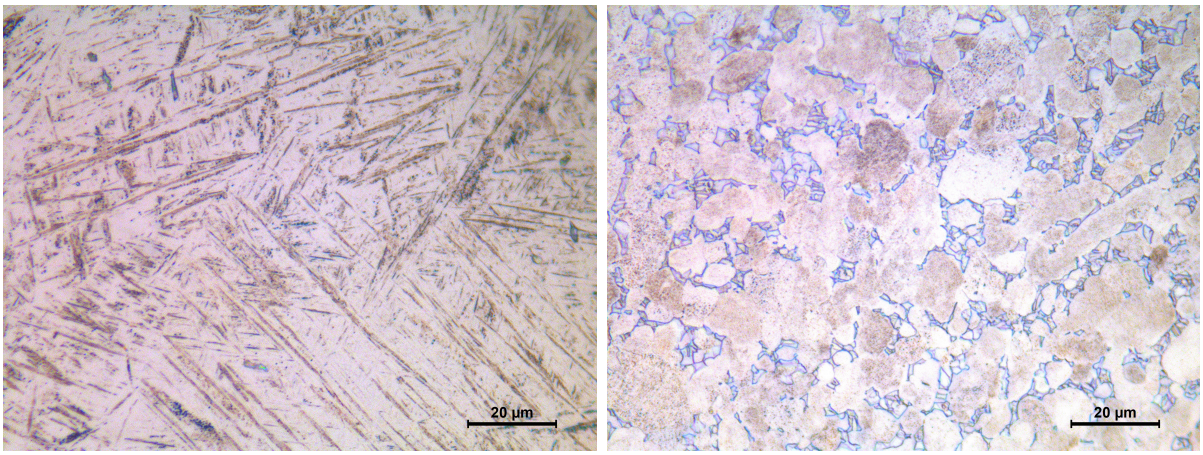

(a) (b)

Figure 34: OM images of the: (**a**) printed sample and (**b**) conventional sample.

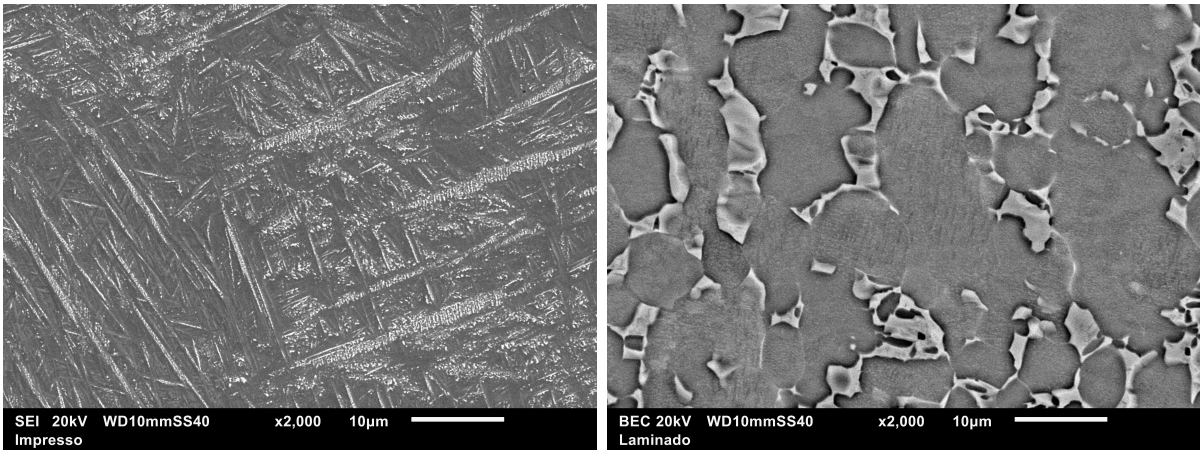

(a) (b)

Figure 35: SEM images of the: (**a**) printed sample and (**b**) conventional sample.

The samples composition were confirmed by an EDS spectrum. Figure 36 shows the results of these analyses for the printed and conventional samples. As expected, titanium,

aluminum and vanadium were the predominant elements detected, and the EDS results were very similar for both alloys.

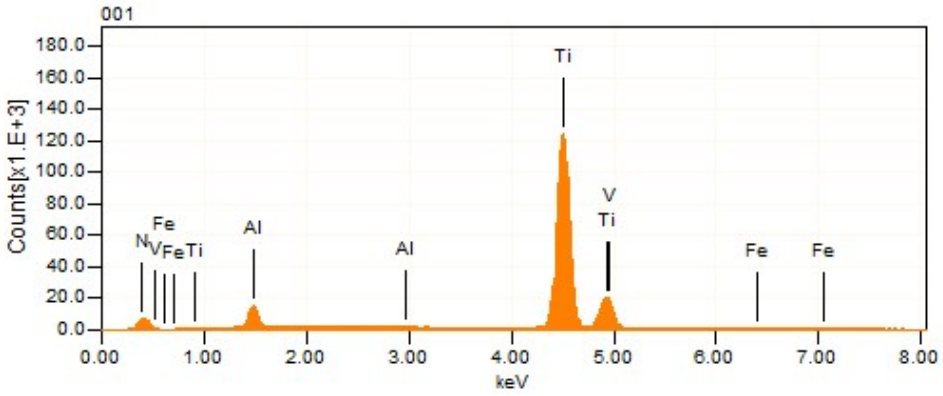

(a)

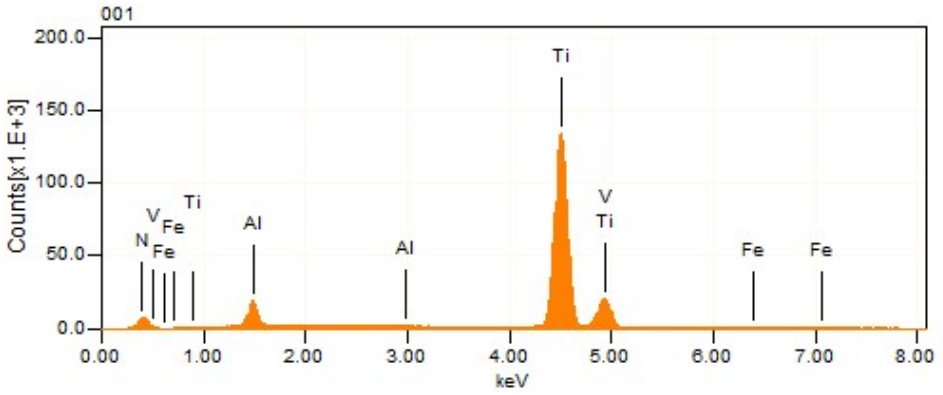

(b)

Figure 36: EDS spectrum of the: (**a**) printed sample e (**b**) conventional sample.

3.3 Micromilling process

3.3.1 Materials used

The micromilling process was carried out in a CNC Mini-mill/GX by Minitech Machinery Corporation available at the Federal University of Uberlândia. This machine presents a maximum feed rate of 1000 mm/min and a maximum spindle speed of 60000 rpm, with a motor model EM-3060 from Nakanishi brand. The positioning error associated with the machine is 0.1 μm and it is controlled through a Mach3Mill CNC.

Regarding the micromilling procedure, no cutting fluid was applied, and the surface of all samples were previously machined with a mill of $\varnothing$2 mm to guarantee surface flatness. Also, the room temperature was kept at 20^{o}C to avoid linear thermal expansion changes.

The cutting and feed forces generated during the process were measured with a Mini Dynamometer from Kistler (MiniDyn type 9256C2). For the force acquisition system, it was used a connector block USB 6221 and a multichannel charge amplifier type 5019 both from Kistler. A scheme on how the equipments were connected is shown in Figure 37.

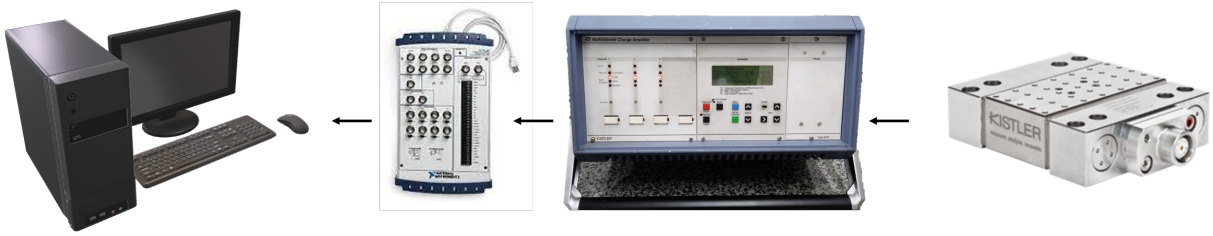

Figure 37: Scheme of the forces acquisition system. Images taken from Kistler [2021b] e NI [2021a]

For making the tests, a total of 12 tungsten carbide micro-end mills with two cutting edges and a TiAlN coating were used. Generally, carbide tools are coated with aluminum or titanium, for example Al_2O_3, TiN, TiC and TiAlN coatings. These coatings, with thickness around 5 μm, present low friction coefficients and they act as a temperature barrier between the tool and the workpiece, which can significantly increase the productivity of the process [YOUSSEF; EL-HOFY, 2008].

The tools, from Rewiid brand, present a helix angle of 35^{o} and its geometry is illustrated in Figure 38. Two different tool diameters (D) were adopted for the experiments: 0.5 mm and 0.8 mm. To check the tool integrity before the experiments, they were observed in the magnifying glass and in the SEM (Figure 39). From the SEM images, their nose radius was determined using ImageJ software. For 0.5 mm cutters the nose radius was approximately 1 μm and for 0.8 mm cutters, 5 μm (Figure 40). Furthermore, in between the experiments, the integrity of the tools were periodically monitored, to assure there were no significant tool wear or tool damage affecting the process.

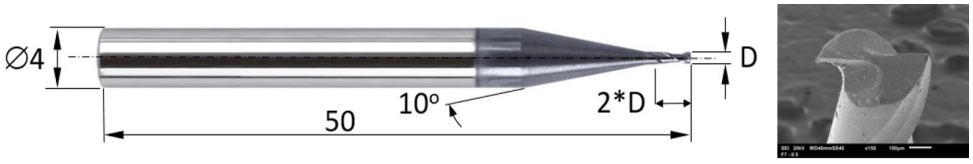

Figure 38: Micromill geometry.

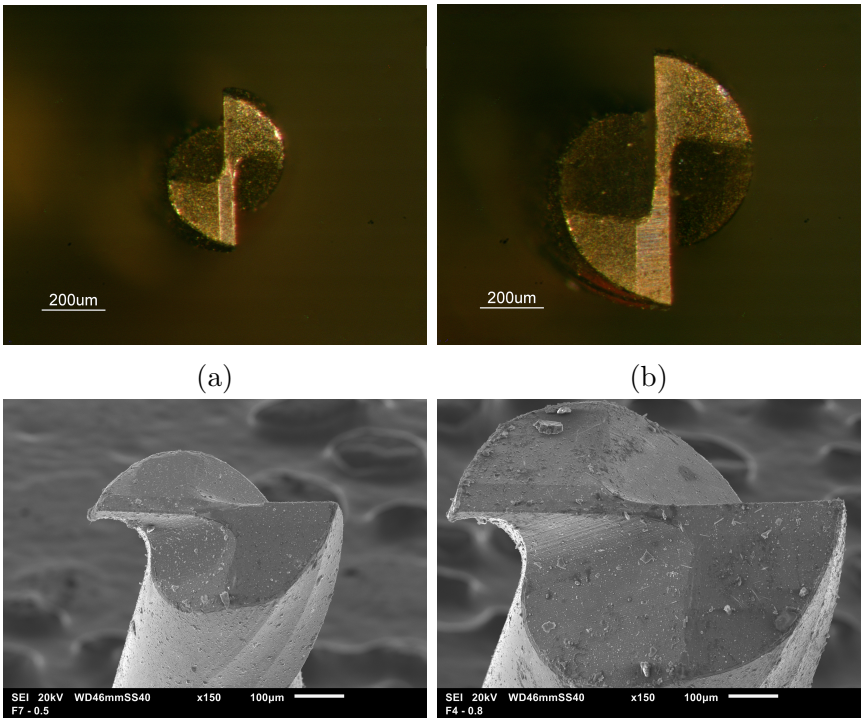

(a) (b)

(c) (d)

Figure 39: Micromills used for the experiments: (**a**) 0,5 mm e (**b**) 0,8 mm (images from the magnifying glass), (**c**) 0,5 mm e (**d**) 0,8 mm (images from SEM).

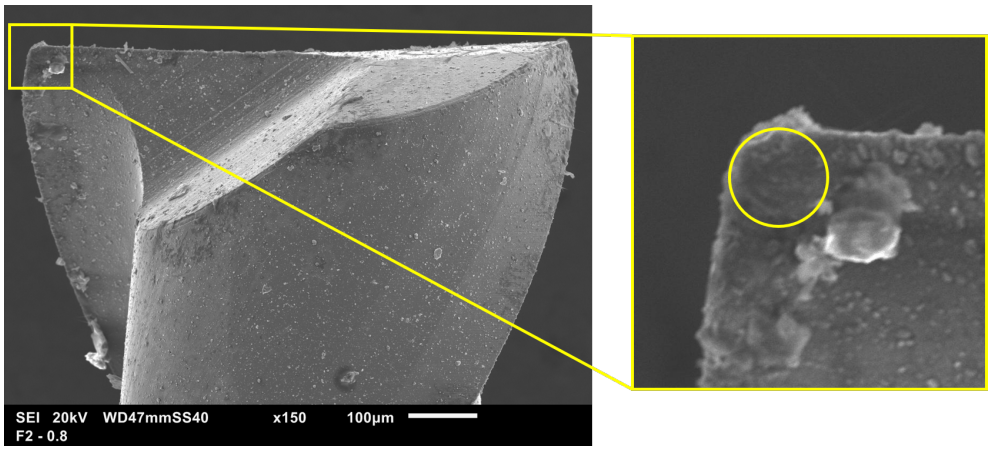

Figure 40: Methodology used to estimate the tool nose radius.

The experimental setup, showing the machine along with the tool, workpiece and dynamometer is illustrated in Figure 41.

Figure 41: Experimental setup

Some micromilling tests were also made in a Schaublin 48 V CNC 3-axis vertical machining center, which presents a maximum power and speed of 7.5 kW and 10000 RPM, respectively. The tests were made for comparisons purposes, since due to this machine restrictions, micromilling was carried out at low speeds of 5000 and 7500 RPM, also without cutting fluid. To measure the cutting forces in this machine, a force measurement system was set up with a Kistler model 9367C dynamometer, an amplifier from the same manufacturer model 5070A11000, a PCI board with RS-232 serial input and a National Instruments data acquisition board model PCIe-6321. In Figure 42 there is an illustration of the connection between this system's components. The software used to collect the data and to filter it in this configuration was the Kistler's DynoWare.

For theses tests, Figure 43 shows the machine in which the experiments were carried out and the assembly of the dynamometer in it and Figure 44 shows the experimental setup in this configuration. The dial gauge in Figure 43b was used during assembly to assure the samples' flatness. From the measurements made with it, the error associated with the tilt of the assembled part was ± 0.003 mm.

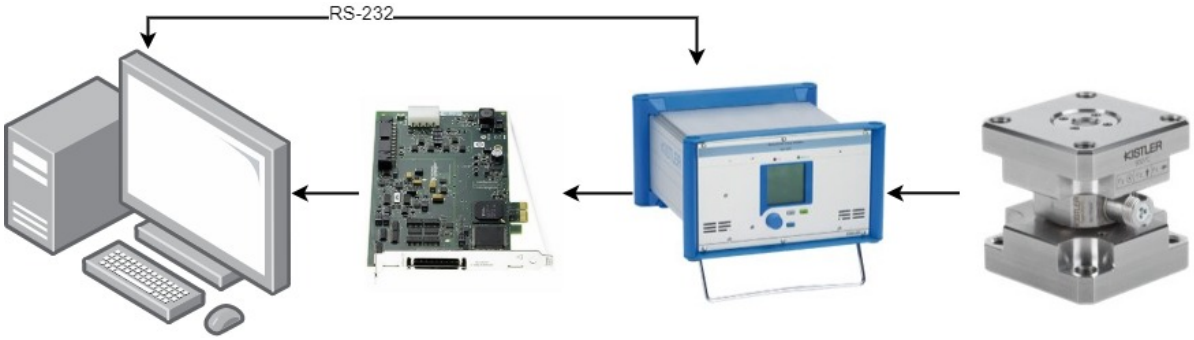

Figure 42: Force acquisition system used for the tests at Schaublin CNC machine. Images taken from Kistler [2021a] e NI [2021b].

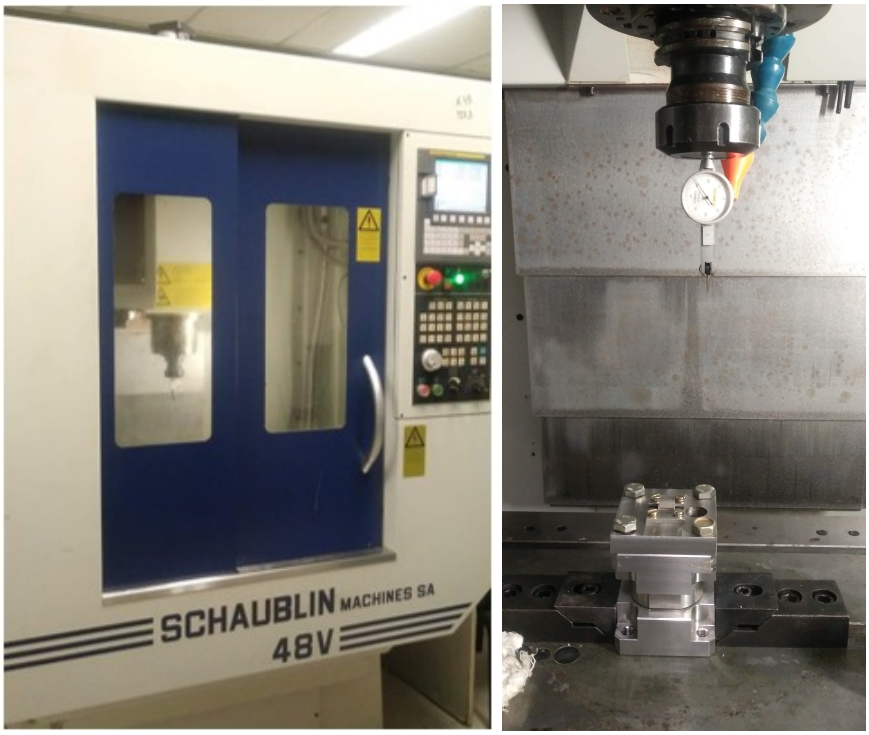

(a) (b)

Figure 43: (**a**) Schaublin CNC machine and (**b**) dynamometer and dial gauge.

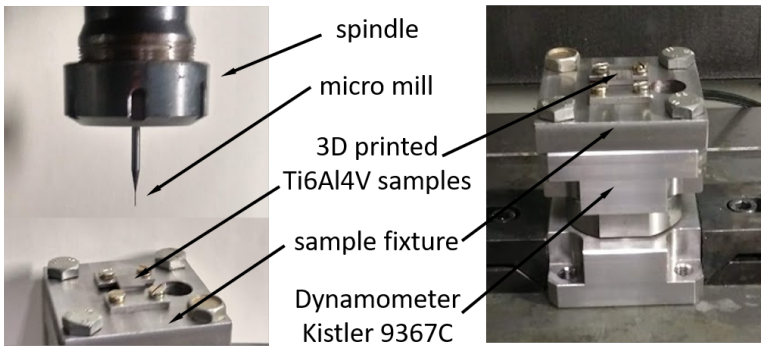

Figure 44: Experimental setup for experiments in the Schaublin CNC machine.

For measuring the machining forces, two dynamometer models were used: model 9256C2 for the tests in the Mini-mill CNC and model 9367C for the Schaublin CNC experiments. Figure 45 illustrates the Kistler piezoelectric dynamometer model 9367C and the quartz transducers of its system. These pressure-sensitive and shear-sensitive quartz disks allow the measurement of force variations in a simple, direct and accurate way. The disks are mounted in a compartment to form a three-way measuring element, where the quartz disks measuring the F_x and F_y forces are shear sensitive and the one measuring the forces F_z, is pressure sensitive (Figure 45) [YOUSSEF; EL-HOFY, 2008; KISTLER GROUP, 2017]. This and other dynamometer models that operate on the same principle are often used in the acquisition of cutting forces from machining processes.

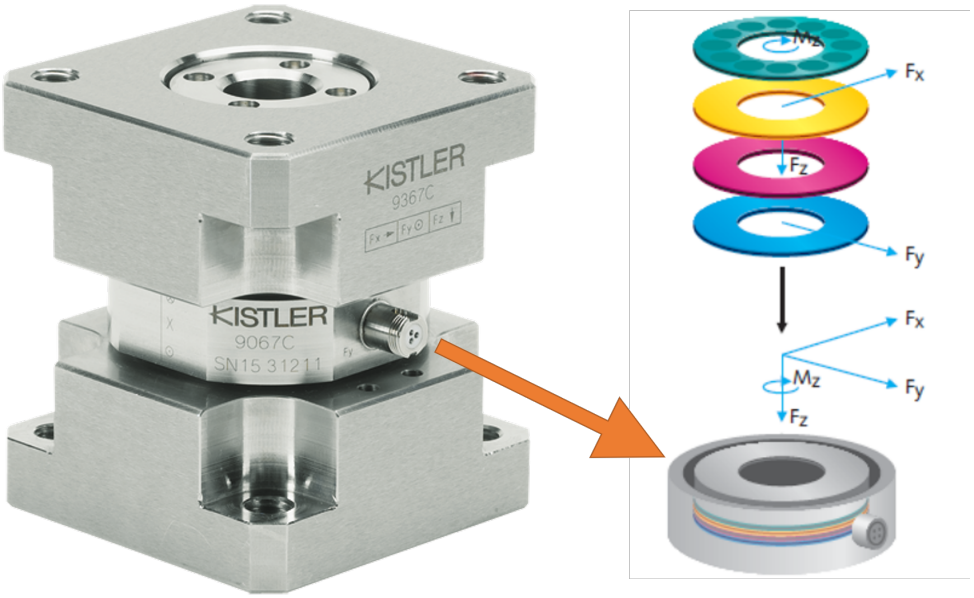

Figure 45: Three-component piezoelectric dynamometer. Source: Kistler Group [2017]

For measuring the cutting forces in micromilling processes it is necessary to apply a dynamometer with high natural frequency. This way, accurate measurement of small forces with minimal influences of thermal effects can be made [KISTLER GROUP, 2003]. The Kistler MiniDyn Model 9256C2 is shown in Figure 46. This dynamometer consists of four 3-component force sensors mounted under high preload between the cover plate and the two lateral base plates. Each force sensor contains three crystal rings, of which the y-direction one is pressure sensitive and the two others are shear sensitive. This way, forces are measured practically without displacement [KISTLER GROUP, 2003].

Figure 46: MiniDyn multicomponent dynamometer. Source: Kistler Group [2003]

Regarding the milling operations, the cutting forces collected from the dynamometers are cyclical, due to the type of intermittent cutting generated by the mill rotation. Thus, the cutting forces tend to increase gradually, generating peak forces for the action of each cutter tooth. This effect is caused due to the gradual accumulation of unremoved material [BALDO, 2013].

3.3.2 Design of experiments

In order to proceed with the micromilling process analysis, microchannels were made in the printed, conventional and printed with heat treatment (HT) samples. The same design of experiments (DOE), was set for the printed and conventional samples. A reduced amount of experiments were made on the heat treated samples, only for comparison purposes. Also, another set of experiments were made on the Schaublin CNC, with the parameters adaptation for lower speeds. The samples and its dimensions are shown in Figure 47. A total of 6 printed samples, 3 without HT and 3 with HT, plus one conventional specimen were used for making all the experiments. For the experiments, the samples were attached to the dynamometer using a fixture designed for this purpose.

The DOE followed a factorial design, varying the cutting speed, the feed per tooth, the tool diameter and the sample's manufacturing process. The set of parameters used for each experiment are shown in Table 12, and the depth of cut was set constant at 0.025 mm. On the workpieces, the spacing between each experiment was the same as the tool diameter size. It should be pointed out that all experiments were repeated for analyzing the experiments repeatability, what leads to a total of 60 experiments on the CNC Mini-mill/GX.

On the Schaublin CNC only the printed samples without heat treatment were tested.

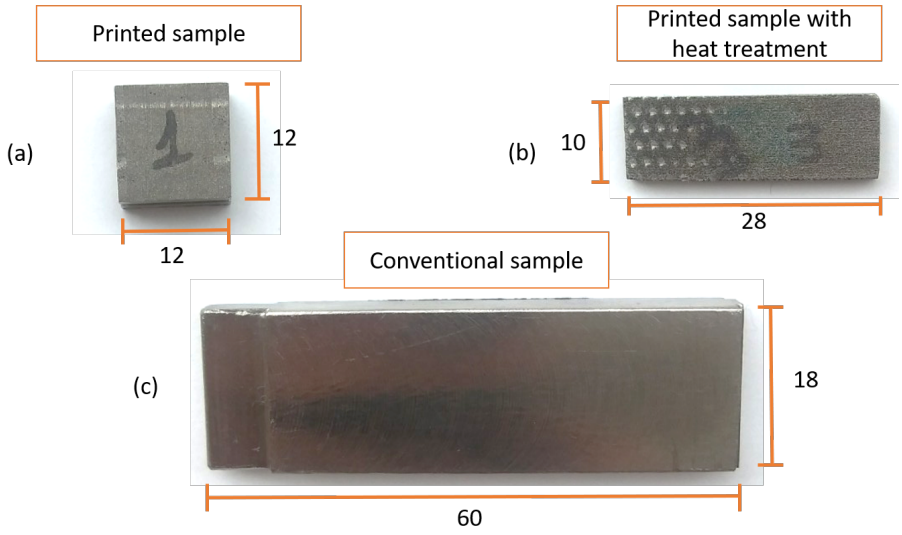

Figure 47: Samples dimensions.

Due to this machine restrictions, the varied parameter was the spindle speed (RPM). Every experiment was repeated once. Counting these experiments, a total of 68 experiments were made.

Table 12: Experiments' factorial design.

Workpiece	**Tool diameter [mm]**	**Cutting speed [m/min]**	**Feed [μm/tooth]**
Printed	0.5 - 0.8	40 - 60	1 - 1.5 - 2
Conventional	0.5 - 0.8	40 - 60	1 - 1.5 - 2
Printed HT	0.5 - 0.8	60	1 - 1.5 - 2
Printed (Schaublin CNC)	0.5 - 0.8	7.8 - 11.8 - 12.6 - 18.8 (5000 & 7500 RPM)	1

3.4 Procedures for data analysis

The cutting and feed forces were acquired at a frequency of 100 kHz through the Labview Express software. Since the data measurements were made with the MiniDyn, presented in Section 3.3.1, no data filtering was applied.

For the Schaublin CNC experiments, an acquisition rate of 1000 Hz was used and the forces in the dynamometer X, Y and Z directions were acquired. As the force data was noisy, a Savitzky Golay filter of a polynomial order 3 to data frames of length 51 was applied. This filter acts as a low-pass filter that smooth the data by extracting the

original signal from a noisy environment while retaining the shape of the signal as close as possible to the original [LIU et al., 2016].

After collecting the forces data for all set of experiments, the surface roughness of each milled channel was measured following the same procedure. For that, the CCI Taylor Hobson 3D profilometer was applied for measuring the 3D roughness by confocal optical interferometry. For each experiment, three measurements in random regions of the channel were made. According to Souza [2016] the roughness parameter S_a is the most suitable for analyzing surfaces that present a texture with a periodic pattern. In fact, the 3D roughness measurements were more conclusive than the 2D ones, so it was the type of measurement adopted in the analysis of the channel's roughness. For the 3D profile, mainly the parameter S_a, S_q, S_{sk} and S_{ku} were analyzed.

After the tests, the workpieces were analyzed in SEM and CCI profilometer, in order to observe burr formation. For a quantitative analysis, burr area from the channels' top view were estimated with ImageJ software, using SEM images. Also, the burr's height was measured with the CCI profilometer.

Also, after the tests, the workpieces were subjected to residual stresses measurements. For that, the x-ray diffractometer Shimadzu, model XRD-7000, from FEI University Center was applied (Figure 48). The measurements were made on the conventional, printed and printed TT samples. For all samples, the tests were carried out on the surface with the microchannels grooves and the measurements were done parallel and perpendicular to it. The parameters used for measuring the RS on the diffractometer are available in Table 13.

Table 13: Diffractometer parameters.

Parameter	**Value**
2θ	53.5° (for printed samples) and 141.5° (for conventional sample)
Sweep range	52° - 54°
Sweep speed	3°/min
ψ	0°, 5°, 10° and 15°
K	-21.6 $kg/mm^2/deg$
Voltage	30 kV
Current	40 mA

After collecting the experimental data, a statistical analysis of correlation was made to identify the influence of the input variables on the results obtained. This analysis was performed for forces, surface roughness and data. Tool wear was visually analyzed from SEM images.

Figure 48: Shimadzu diffractometer available at FEI University Center.

To perform a statistical comparison between the cutting forces magnitude, the effective value of the machining forces were estimated following the same methodology applied by Antonialli [2009]. For that, the Root Mean Square (RMS) of the force's data were calculated following Equation 3.1:

$$F_{RMS} = \sqrt{\frac{1}{N}\sum_{i=1}^{N} F_i^2} \tag{3.1}$$

where N is the number of measurements of each of the instantaneous values of force F_i. F_{RMS} values were the effective values used for making the statistical analysis.

In the correlation analysis, the Pearson correlation coefficient was estimated. This analysis will be presented in more detail below.

3.4.1 Pearson correlation coefficient

The population correlation coefficient, $\rho(X, Y)$, is a statistic that allows measuring the interdependence relationship between two random variables X and Y, defined by the equation 3.2. Its estimator $r(X, Y)$ can be calculated from samples using equation 3.3 and this was the calculated coefficient for the experiments [DEVORE, 2010].

$$\rho = \frac{\mathrm{cov}(X, Y)}{\sigma_X \sigma_Y} \tag{3.2}$$

$$r = \frac{\sum_{i=1}^{n}(x_i - \overline{x})(y_i - \overline{y})}{\sqrt{\sum_{i=1}^{n}(x_i - \overline{x})^2(y_i - \overline{y})^2}} \tag{3.3}$$

Pearson's correlation coefficient, r, represents the degree and direction in which the X and Y variables are linearly associated in a sample [DEVORE, 2010]. This coefficient assumes values in the interval [-1,1], whose interpretation can be seen in Table 14 and in Figure 49. When r takes on a negative value, this indicates that when one variable increases, the other decreases, while for $r > 0$, both increase or decrease together.

Table 14: Pearson's correlation coefficient interpretation. Source: Vieira [2012]

r	**Meaning**
1 or -1	ideal positive/negative correlation
$0,75 < r < 1,00$ or $-1,00 < r < -0,75$	strong correlation
$0,50 < r < 0,75$ or $-0,75 < r < -0,50$	moderate correlation
$0,25 < r < 0,50$ or $-0,50 < r < -0,25$	weak correlation
$0 < r < 0,25$ or $-0,25 < r < 0$	small correlation
0	null correlation

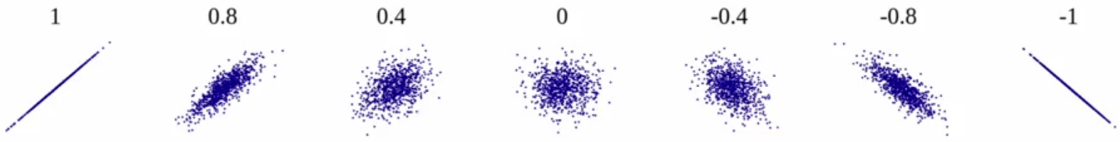

Figure 49: Hypothetical examples of the Pearson correlation coefficient. Source: Gunderson, West and Shedden [2020]

The representation of the Pearson correlation in this work was presented using heat maps. These maps are used to analyze the influence of several variables on each other, as it is a visually intuitive way to present correlations. A heat map is represented by a table A_{ij} where its rows and columns represent the variables analyzed and a cell a_{ij} is filled with the correlation of the variable in row i with that in column j. From this construction, the diagonals a_{ij}, when $i = j$, represent the correlation between the same variables and therefore must be equal to 1. Finally, the table entries are colored in a scale of colors to provide intuitive visual interpretation of correlations.

The Python language offers tools that allow plotting heat maps without much effort. Thus, these graphs were plotted for each analysis made: forces, surface roughness, residual stresses and burr formation.

4 RESULTS AND DISCUSSION

4.1 Machining forces analysis

The following subsections present the machining forces results for the conventional, printed and printed HT samples. It is followed by a statistical analysis of correlation between the results. At the end, the cutting forces results for the samples machined in the Schaublin CNC are shown.

4.1.1 Conventional sample

To have an overview on how the machining forces behave, the cutting and feed forces results were zoomed on the middle of the experiment, around 7 mm of channel length. The outcomes are shown in Figures 50 and 51. From these results, it can be observed the influence of each tooth of the tool on the machining forces results. Also, the influence of the feed per tooth is also seen, as for higher feeds each tooth is removing more material.

For all experiments made on the conventional sample, the machining force results are shown in Table 15. The error was calculated considering the replica. The forces variation with the cutting parameters will be further analyzed in Section 4.1.4.

The influence of the action of each cutting edge of the tool on the cutting forces can be better visualized in Figure 52. As it can be seen, in one rotation of the tool, the cutting edge comes into contact with the workpiece causing a initial crushing of the material and, gradually, the chip thickness increases until reaching its maximum value. After that, the peak force decays, as chip thickness decreases. Then, the processes of plastic deformation, elastic recovery, chip formation and material removal start again on the second cutting edge. In this dynamic, as the chip load increases, the cutting forces increases and vice-versa, what leads to the sinusoidal shape of the force curve. According to Baldo [2013], in conventional milling operations the peak values are around the same magnitude. Although, for some set of cutting parameters in micromilling, the gradual

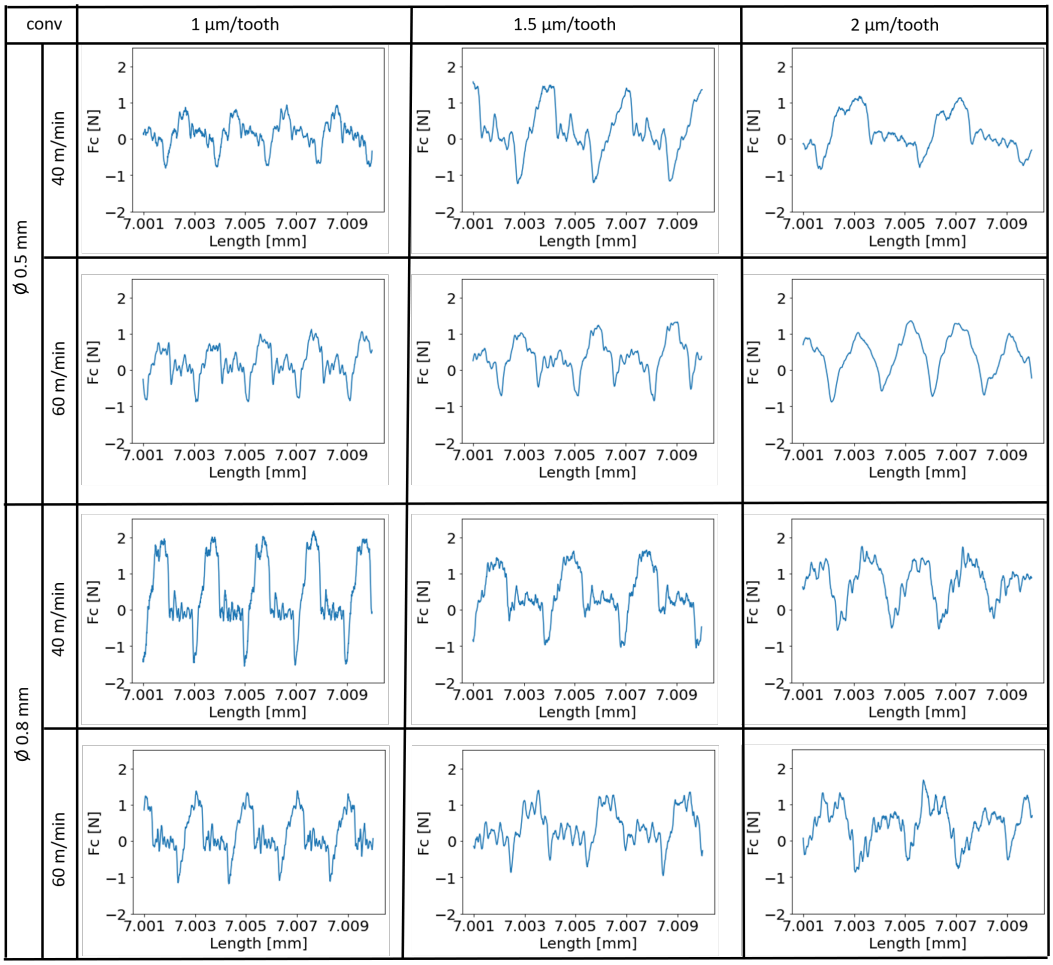

Figure 50: Cutting forces results for the conventional sample.

accumulation of material that is not removed can become more critical, what causes differences in cutting force peaks for some experiments. This cutting force behavior can be further extended to feed forces.

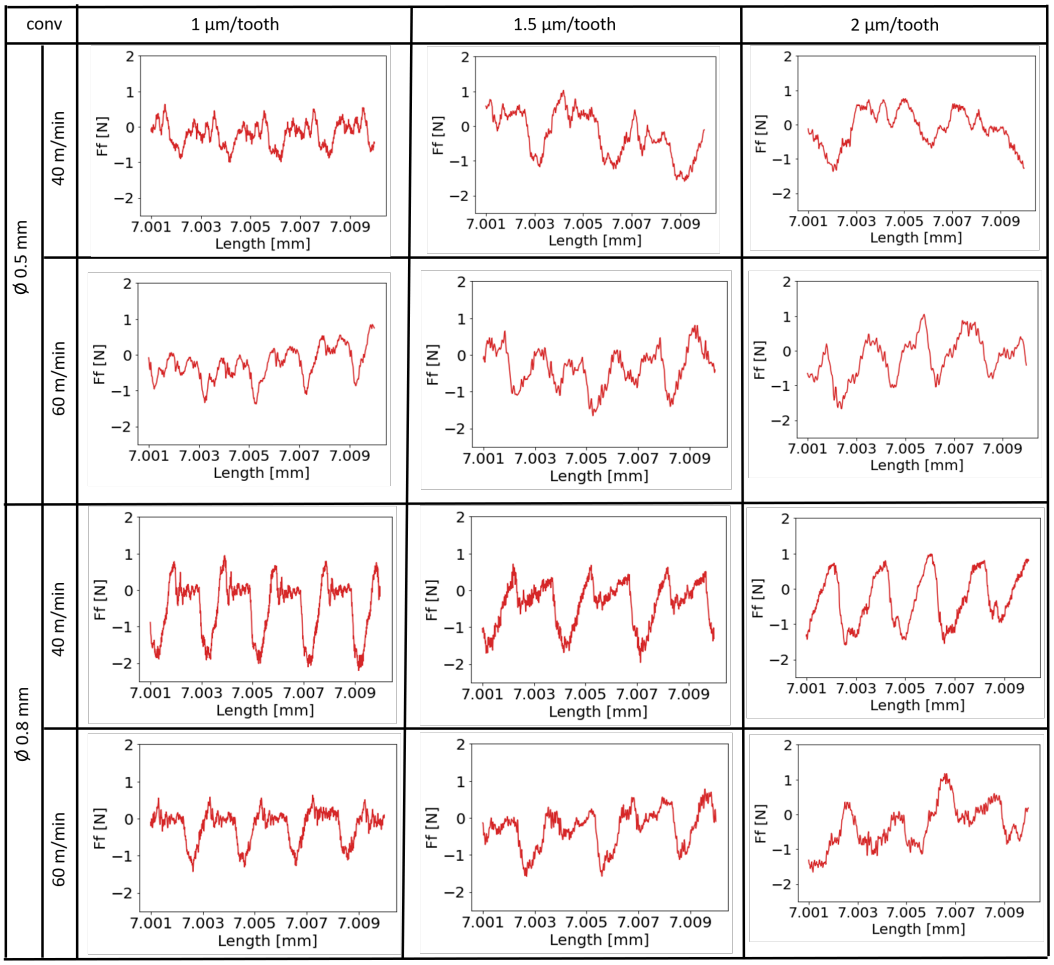

Figure 51: Feed forces results for the conventional sample.

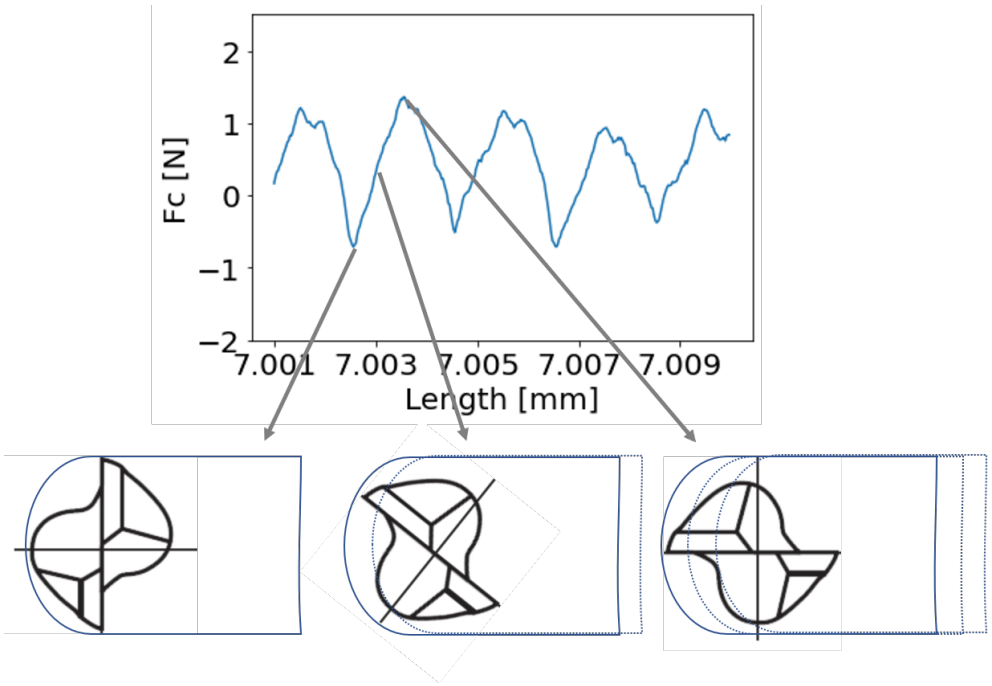

Figure 52: Result of the cutting edge motion on cutting forces.

Table 15: Machining force results for the conventional sample.

Tool (mm)	**Feed (μm/tooth)**	V_c **(m/min)**	Fc_{rms} **(N)**	Ff_{rms} **(N)**
0.5	1	40	0.517 ± 0.031	0.351 ± 0.002
0.5	1	60	0.530 ± 0.025	0.455 ± 0.013
0.5	1.5	40	0.833 ± 0.005	0.600 ± 0.015
0.5	1.5	60	0.619 ± 0.002	0.609 ± 0.012
0.5	2	40	0.637 ± 0.007	0.617 ± 0.003
0.5	2	60	0.773 ± 0.037	0.805 ± 0.005
0.8	1	40	0.966 ± 0.001	0.739 ± 0.001
0.8	1	60	0.700 ± 0.036	0.482 ± 0.019
0.8	1.5	40	0.833 ± 0.002	0.641 ± 0.007
0.8	1.5	60	0.558 ± 0.007	0.445 ± 0.013
0.8	2	40	0.821 ± 0.011	0.657 ± 0.017
0.8	2	60	0.600 ± 0.017	0.626 ±0.001

4.1.2 Printed samples

On the same way, the cutting and feed forces results for the printed samples, are shown in Figures 53 and 54. Comparing the forces results of the printed and conventional samples, they visually present the same behavior for the same set of cutting parameters. Regarding values, cutting and feed forces apparently are in the same magnitude range (varying up to 2 N). Although, the cutting forces results seems more reliable, as the action of each tooth is more clear in these results.

The same way, the machining force results are shown in Table 16 for the printed samples.

Table 16: Machining force results for the printed samples.

Tool (mm)	**Feed (μm/tooth)**	V_c **(m/min)**	Fc_{rms} **(N)**	Ff_{rms} **(N)**
0.5	1	40	0.473 ± 0.015	0.317 ± 0.009
0.5	1	60	0.491 ± 0.038	0.432 ± 0.021
0.5	1.5	40	0.863 ± 0.015	0.648 ± 0.034
0.5	1.5	60	0.601 ± 0.018	0.554 ± 0.012
0.5	2	40	0.587 ± 0.020	0.540 ± 0.010
0.5	2	60	0.764 ± 0.018	0.764 ± 0.027
0.8	1	40	0.738 ± 0.032	0.557 ± 0.033
0.8	1	60	0.688 ± 0.016	0.513 ± 0.026
0.8	1.5	40	0.810 ± 0.018	0.638 ± 0.007
0.8	1.5	60	0.554 ± 0.002	0.430 ± 0.004
0.8	2	40	0.874 ± 0.032	0.713 ± 0.006
0.8	2	60	0.569 ± 0.004	0.571 ± 0.011

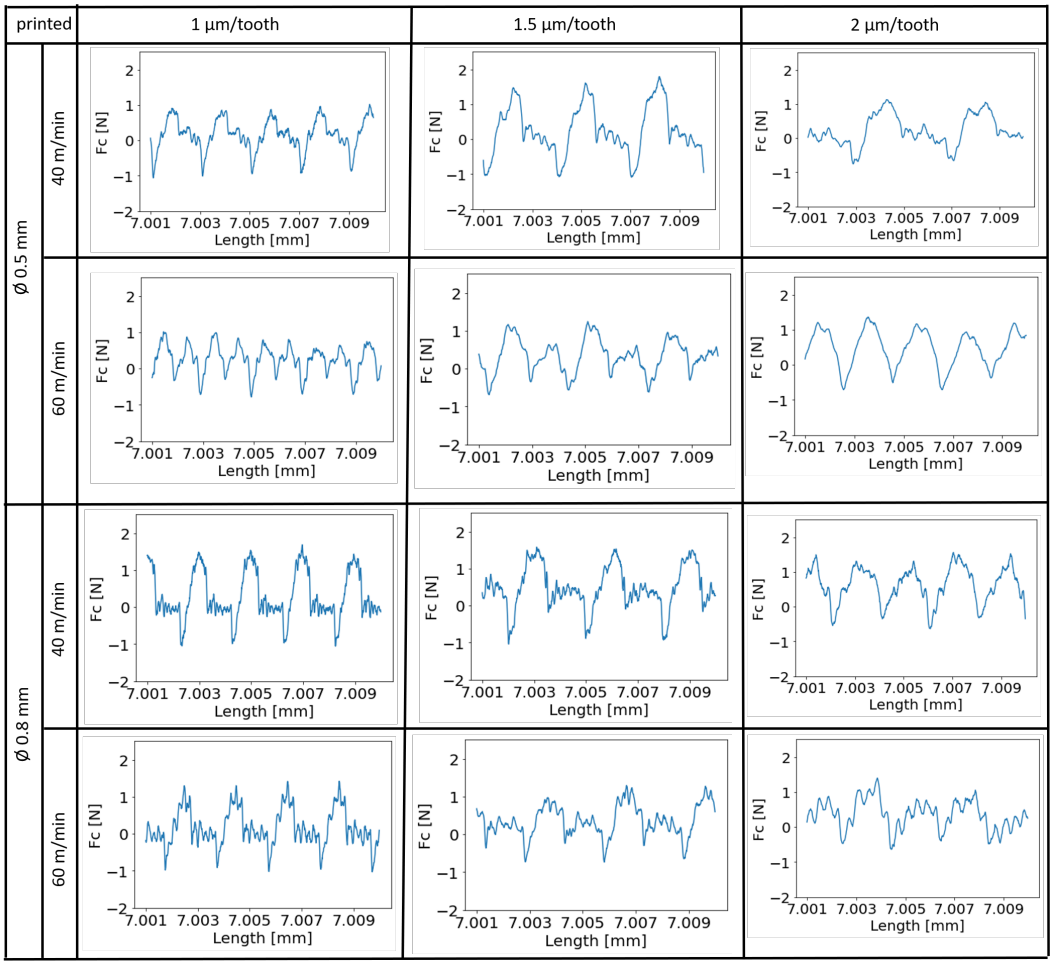

Figure 53: Cutting forces results for the printed samples.

4.1.3 Printed samples with heat treatment

For the printed samples with heat treatment, the cutting and feed forces results, are shown in Figures 55 and 56. In comparison to the other forces results presented, the action of each cutting edge on the machining forces are not easily distincted. Although, its magnitudes are still in the same range, as it can be seen in Table 17.

Table 17: Machining force results for the printed samples with heat treatment.

Tool (mm)	**Feed (μm/tooth)**	V_c **(m/min)**	Fc_{rms} **(N)**	Ff_{rms} **(N)**
0.5	1	60	0.544 ± 0.044	0.475 ± 0.015
0.5	1	40	0.543 ± 0.036	0.385 ± 0.042
0.5	1.5	60	0.765 ± 0.019	0.635 ± 0.025
0.5	2	60	0.640 ± 0.002	0.663 ± 0.023
0.8	1	60	0.659 ± 0.003	0.478 ± 0.008
0.8	1.5	60	0.869 ± 0.020	0.612 ± 0.001
0.8	2	60	0.773 ± 0.018	0.644 ± 0.029

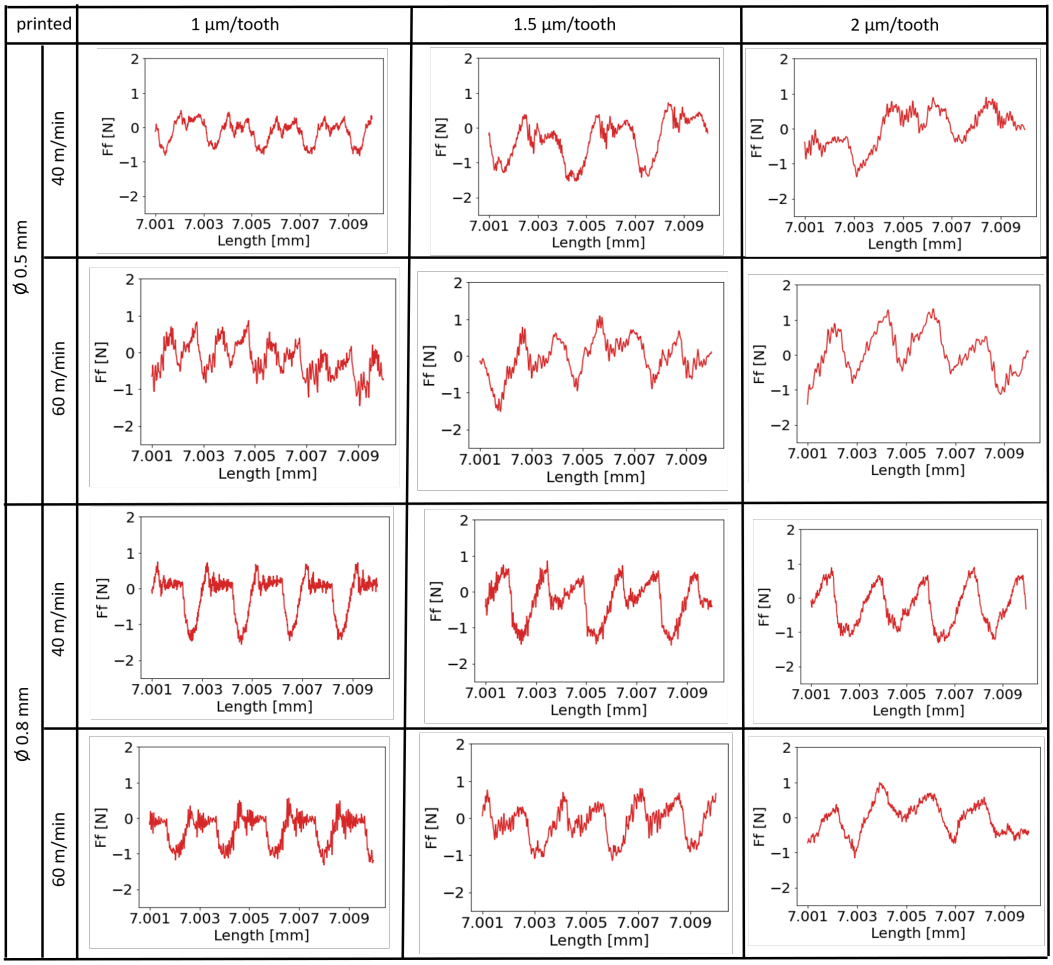

Figure 54: Feed forces results for the printed samples.

4.1.4 Analysis and comparisons of machining forces data

Visually comparing the results among the conventional and printed samples, no significant changes on the cutting forces results are seen. Although, taking into account the HT printed sample, forces behavior seems to differ. For example, Figure 57 shows the cutting forces comparison between the conventional and printed materials under the sets: Vc = 60 m/min, fz = 2 μm/tooth, and $\varnothing$ = 0.5 mm; and Vc = 60 m/min, fz = 1 μm/tooth, and $\varnothing$ = 0.8 mm.

To analyze if samples' manufacturing processes were significantly influencing cutting and feed force's results, correlation analyses were done and the Pearson's coefficient obtained for both cases were less than 0.1 (Figures 58a and 58b, respectively). Intuitively, the variation on the microstructure should lead to cutting forces variations. Although, the printing strategies applied for manufacturing the printed samples aimed to achieve mechanical properties results as close as possible to the conventional manufactured alloy. For this reason, the strategy applying the 67^{o} interlayer rotation and a sweep range of 5

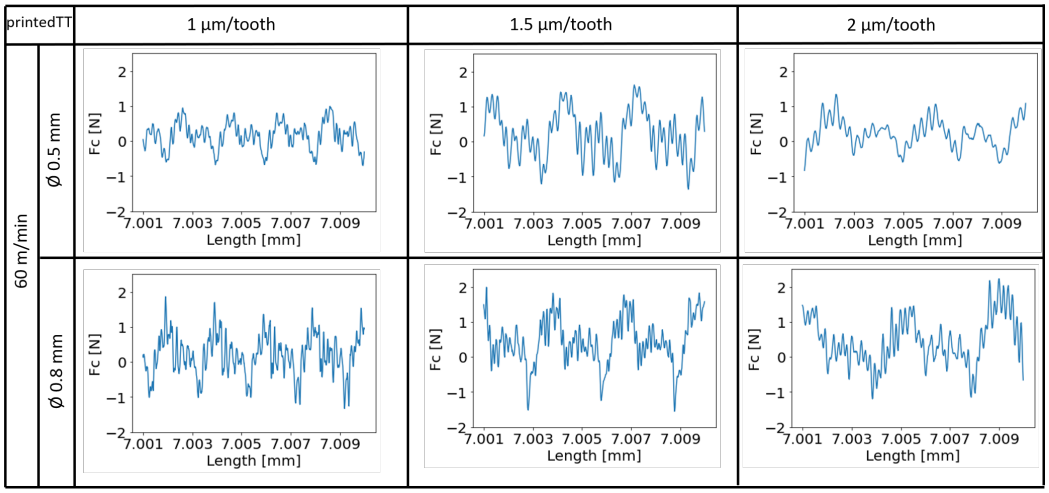

Figure 55: Cutting force results for the printed samples with heat treatment.

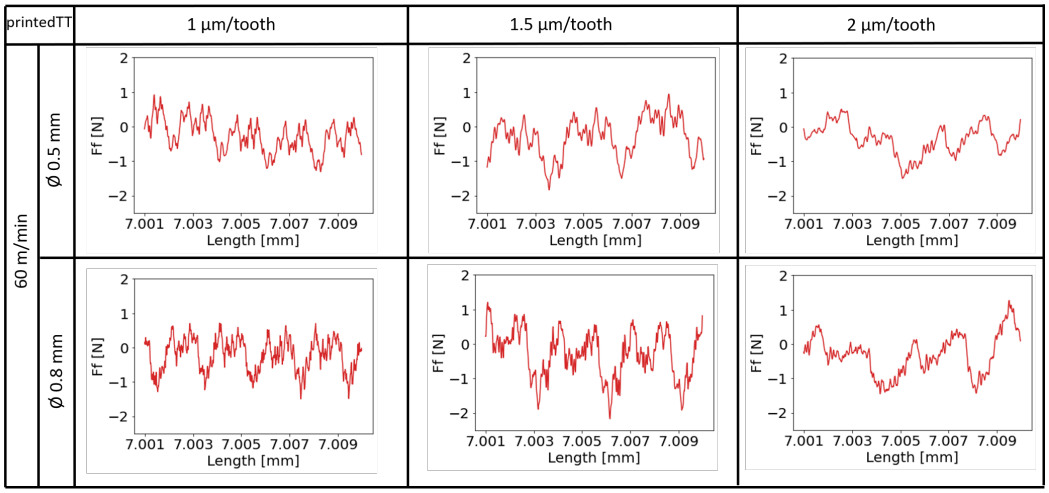

Figure 56: Feed force results for the printed samples with heat treatment.

mm, leads to a good material's homogeneity, what makes the cutting forces results very close for both printed and conventional alloys. Also, the heat treatment does not seem to influence the micromilling forces results. For this reason, the correlation analyses presented here will cover only the influence of the tool diameter, feed per tooth and cutting speed.

In addition, from Figures 57d or 57e, it becomes clear that, for some experiments, the contribution of one cutting edge is very low to negligible. It means that one tooth of the tool is not effectively cutting the material. This behavior was addressed to the scale effect, because it was observed for the bigger tool diameter, which presents a greater tool nose radius. In this case, the feed rate is too low and one cutting edge is only rubbing and burnishing the material and no effective cut is happening. Once the next edge enters the material, it removes the material left by the other cutting edge. This behavior harms the surface roughness and increase burr formation.

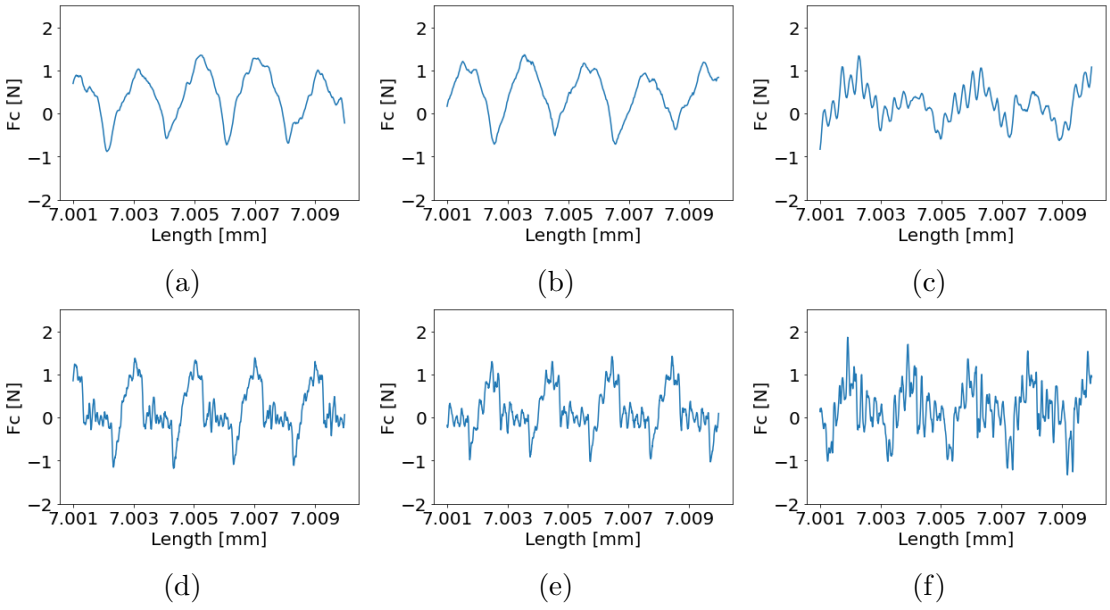

Figure 57: Cutting forces results for: (**a**) conventional sample, (**b**) printed samples and (**c**) printed HT samples with Vc = 60 m/min; fz = 2 μm/tooth; and $\varnothing$ = 0.5 mm and (**d**) conventional sample, (**e**) printed samples and (**f**) printed HT samples with Vc = 60 m/min; fz = 1 μm/tooth; and $\varnothing$ = 0.8 mm.

Another mechanism observed in the experiments was tool run-out. Since the tool run-out modifies the theoretical position of mill cutting edges during machining [MAUREL-PANTEL et al., 2013], the channel width will usually be greater than tool diameter. Following the same methodology as Attanasio [2017] for confirming the tool run-out in micromilling, Figures 59a and 59b compares the tool diameter measurements and the effective channel width for the 0.5 and 0.8 mm tool diameters, respectively. From that, it can be observed that the channels' width are few micrometers larger than tool diameter, what is due to tool run-out. This phenomenon directly influences the surface roughness, geometrical accuracy, tool wear and cutting stability and it can be reduced by optimizing

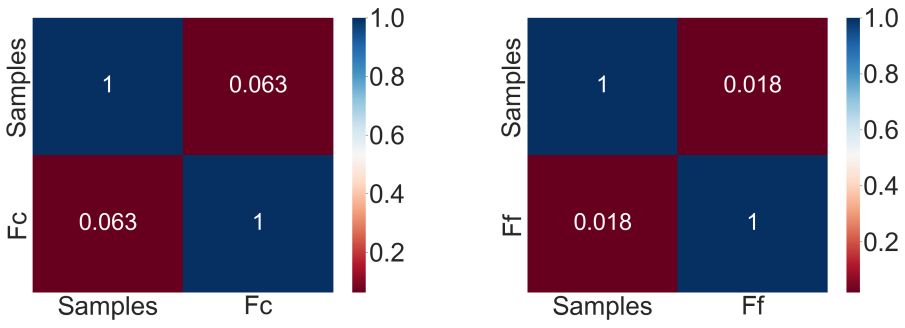

Figure 58: Heat map for analyzing the correlation among the samples manufacturing process and **(a)** cutting forces and **(b)** feed forces results.

cutting parameters [ATTANASIO, 2017].

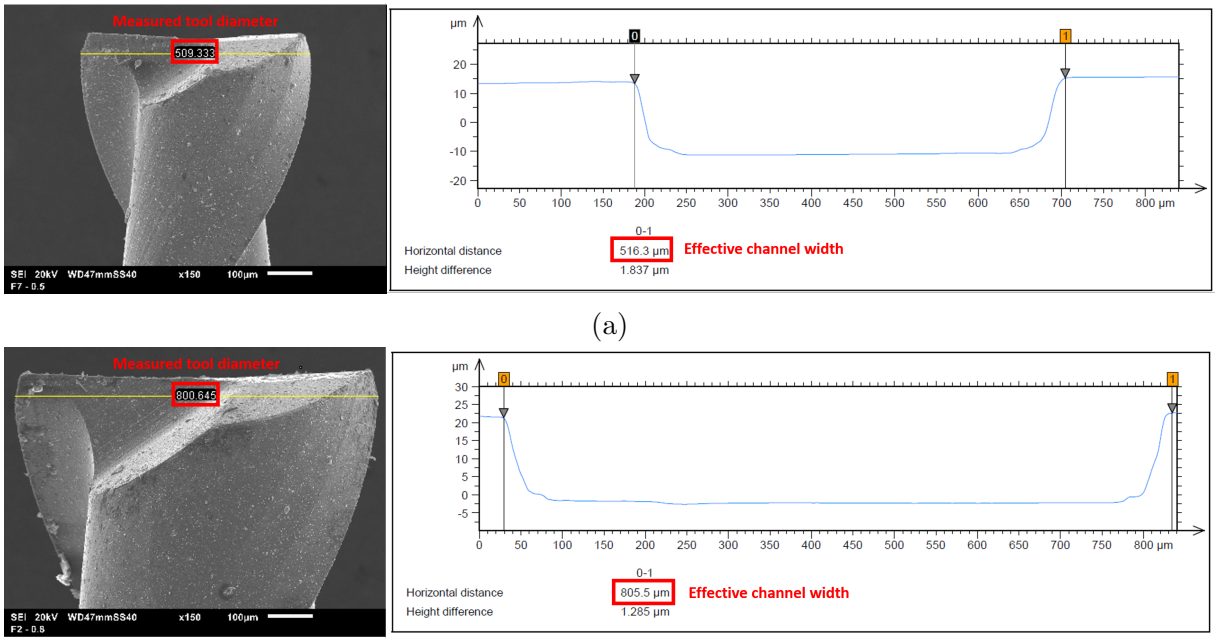

Figure 59: Tool diameter measurements (μm) and effective channel width for the: (**a**) 0.5 and (**b**) 0.8 tools.

To analyze the influence of the cutting parameters on the cutting forces results, the Pearson's correlation coefficients were estimated. The obtained results are presented in the heat map shown in Figure 60. By the correlation analysis, it can be observed that:

- The cutting forces present a weak correlation to the cutting speed, according to Silvia and Shimakura [2006]'s classification (Table 14);
- The negative signal of Pearson's correlation coefficient among cutting force and cutting speed means that as cutting speed increases, cutting forces tend to decrease or vice-versa;
- The second parameter that influences the cutting forces is the tool diameter and the positive correlation indicates that as the tool diameter increases, cutting forces tend to increase.
- Feed per tooth presented a small to null correlation to the cutting forces.

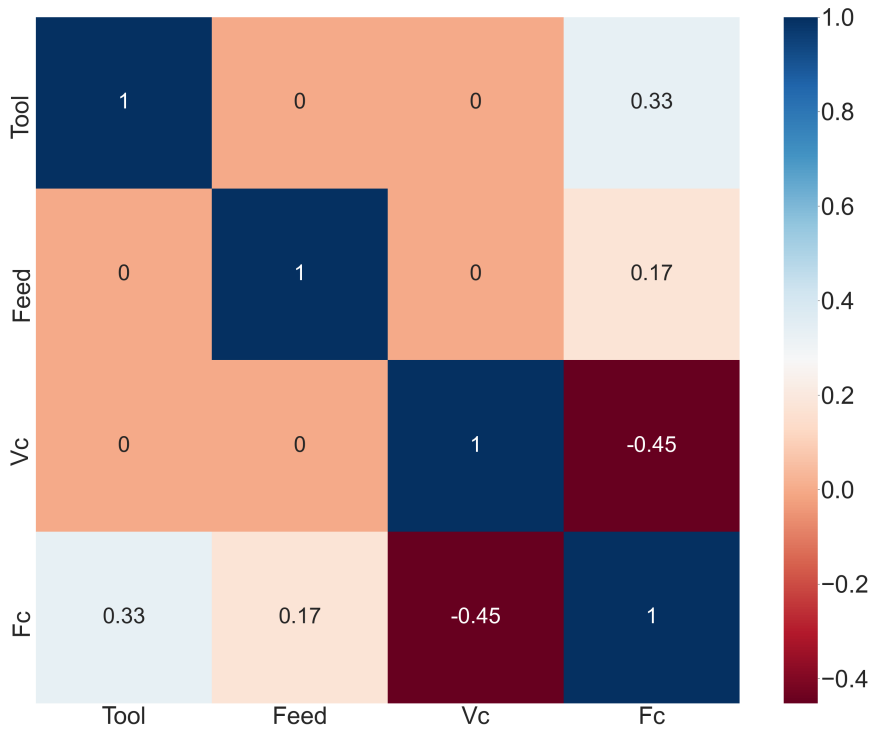

Figure 60: Heat map for analyzing the correlation among the cutting parameters and cutting forces.

To better visualize the relationship between the most influencing parameter (Vc) on cutting forces, a joint plot between them was made (Figure 61). This plot shows the data distribution in a $Fc \times Vc$ graph, showing that as Vc increases, Fc reduces. Also, it shows the p-value statistic equals 0.026. Meaning that there is a 2.6% probability that the results are due to chance [SINGH, 2013]. Considering a 5% significance level, statistical inferences indicate that, for a p-value of 0.026, the null hypotheses should be rejected. The null hypothesis in the Pearson test is that there is no correlation between the analyzed variables. In this case, rejecting the null hypothesis indicates that there is a statistical evidence that the cutting speed influences the cutting forces results in micromilling.

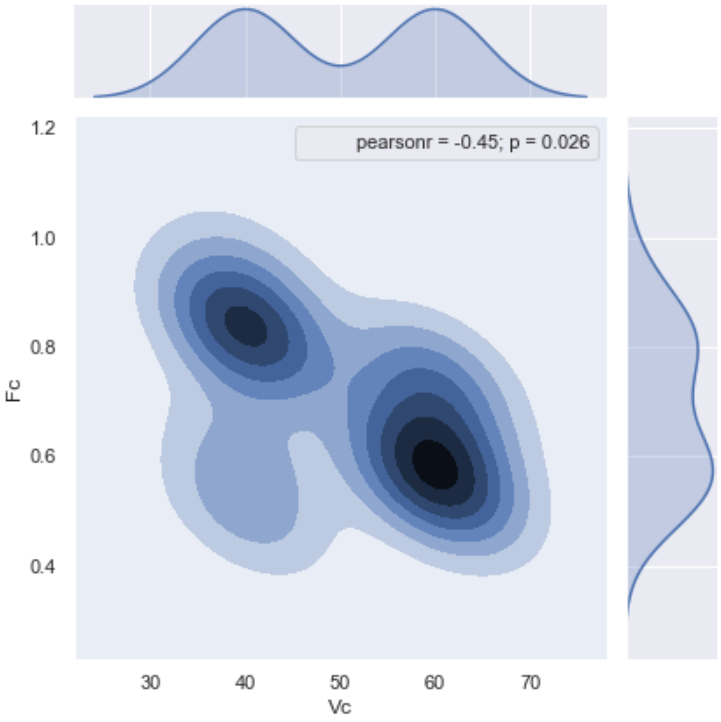

Figure 61: Joint plot of Fc x Vc.

Regarding the feed forces, the same analysis was made. For this case, the heat map and joint plot are shown in Figures 62 and 63. From that, it can be seen that the feed was the most influencing variable on the feed forces, with a moderate and positive correlation. This means that feed forces increases with feed per tooth. From the p-value of 0.0034, the null hypothesis is rejected meaning that the feed per tooth influences the feed force results.

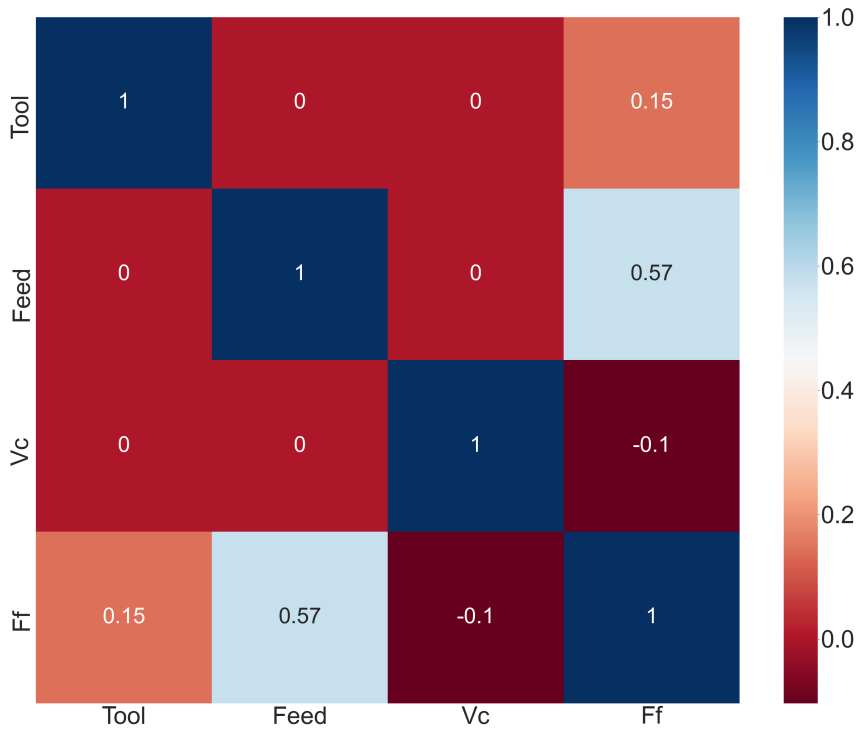

Figure 62: Heat map for analyzing the correlation among the cutting parameters and feed forces.

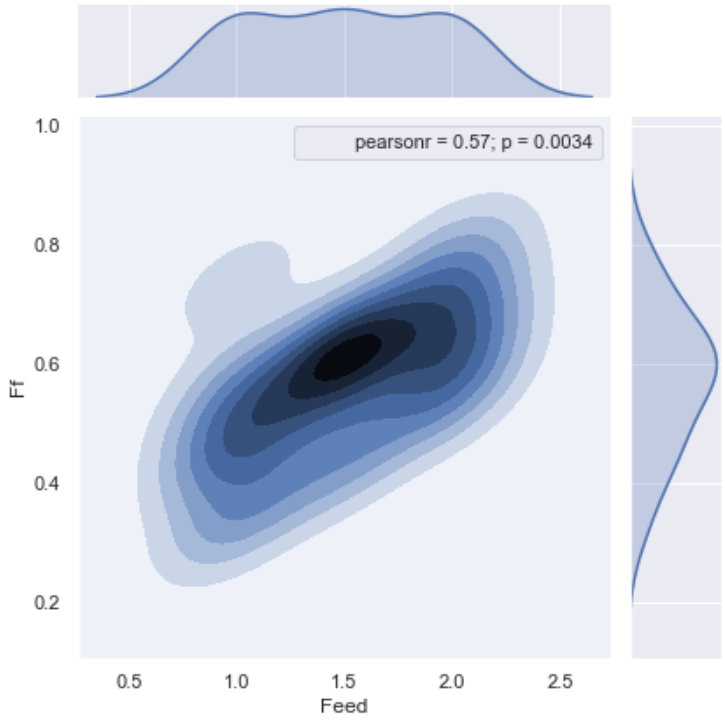

Figure 63: Joint plot of Ff x Feed.

4.1.5 Cutting forces results for Schaublin CNC experiments

Figures 64 and 65 present the cutting and feed forces for the experiments made in the Schaublin CNC, respectively. This machine is more robust and limited than the Mini-mill CNC used for the previous experiments. Also, the dynamometer used for these experiments (type 9256C2) is indicated for measuring forces in a range of ±10 kN (while the MiniDyn measures forces up to 250 N), consequently, it presents a lower sensitivity than the MiniDyn. In addition to that changes, the cutting speeds used were lower, because of the CNC limitation. All that influences the machining forces and explains why the results presented in this section are different from the the ones for the printed sample presented before.

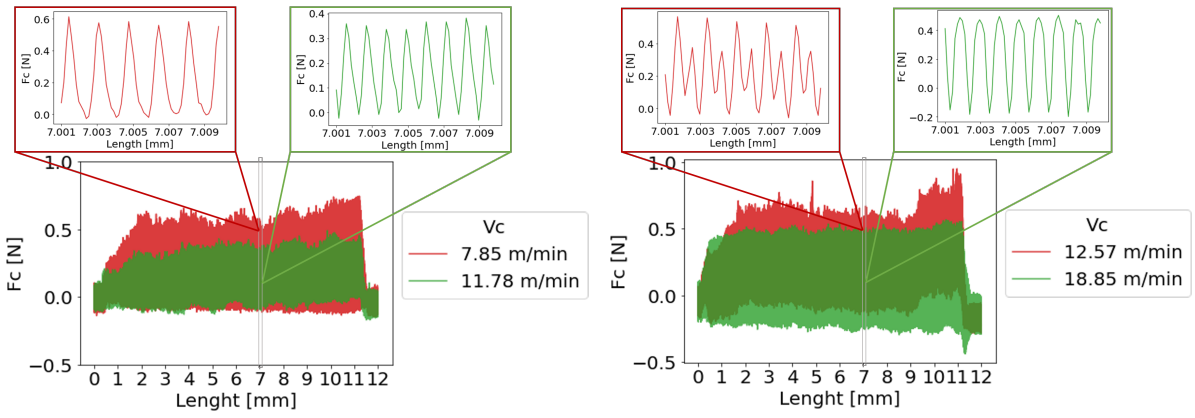

(a) (b)

Figure 64: Cutting forces for the Schaublin experiments with a tool diameter of: (**a**) 0.5 and (**b**) 0.8 mm.

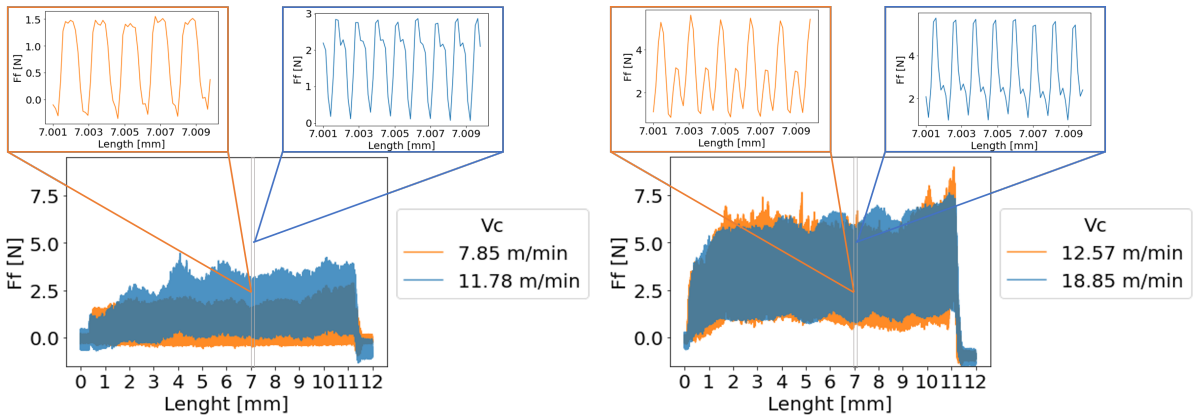

(a) (b)

Figure 65: Feed forces for the Schaublin experiments with a tool diameter of: (**a**) 0.5 and (**b**) 0.8 mm.

The first thing to notice from Figures 64 and 65 is that the feed forces were distinctively

higher than the cutting forces. This was not observed on the experiments done with the MiniDyn. Considering the feed force range, the results were much higher than for the forces measured with the MiniDyn, reaching around 7.5 N. Although, no concrete statement can be concluded from this results, because the cutting speeds were lower for this experiments, and the setup changed, so the forces were expected to be higher. Another point to notice is the action of each tool teeth on the cutting forces' zooms, that even in a conventional CNC machine with a more robust dynamometer, could be observed.

In addition, the measured cutting and feed forces were visually higher for the highest tool diameter. As other researches approached [MEHDI, 2018], this can be attributed to the natural frequency of the system with a bigger mass, that can lead to instabilities of the system and, consequently, a higher machining force. Indeed, for the experiments in the robust system, the Pearson correlation coefficient results (Figures 66 and 67) show that the tool diameter was the parameter with highest influence on cutting and feed forces results. For analyzing the forces results, the F_{RMS} values were calculated from the filtered data. The results show that cutting speed also had a correlation to the cutting forces. Since feed was set constant, its influence on feed forces could not be observed.

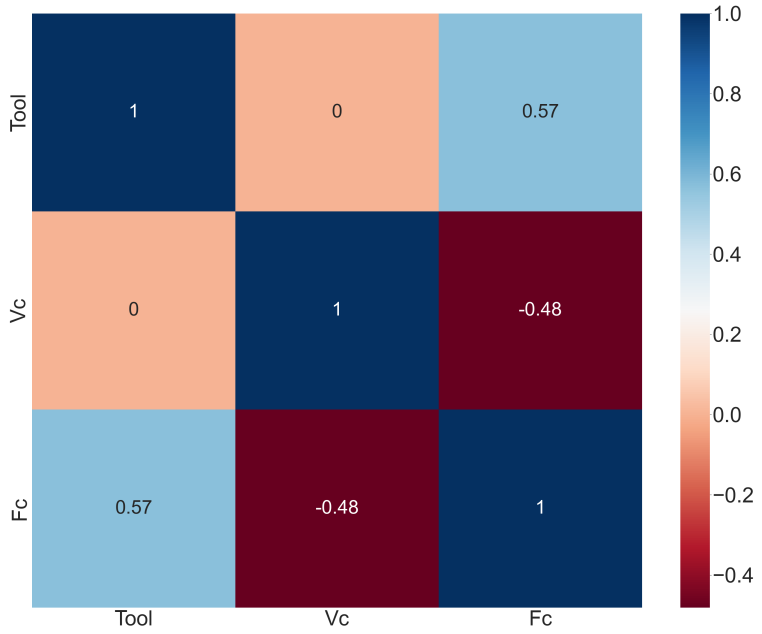

Figure 66: Heat map showing the correlation among the cutting forces, cutting speed and tool diameter for the Schaublin CNC experiments.

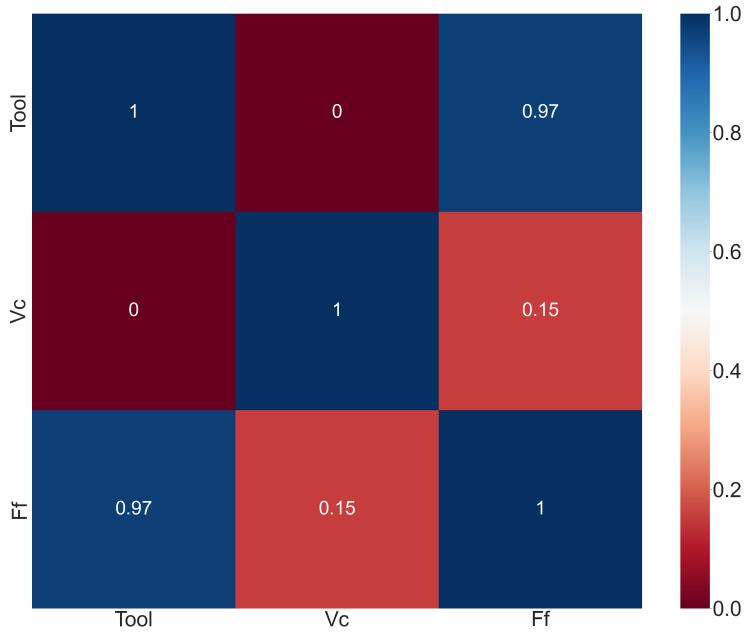

Figure 67: Heat map showing the correlation among feed forces, cutting speed and tool diameter for the Schaublin CNC experiments.

4.2 Surface roughness analysis

In the following subsections, the surface roughness results are presented separately for the conventional, printed and printed with heat treatment samples.

4.2.1 Conventional sample

For each experiment, the average results of the arithmetic mean of the area (S_a) and the root mean square height (S_q), which is more sensible to higher heights variation, for the conventional sample are plotted in Figures 68 and 69. Their numerical results are shown in Table 18. As it can be seen, the surface roughness increases for lower speed and the best surface roughness results are achieved with lower diameter tools. Although, no relation can be settled between feed per tooth and surface roughness values.

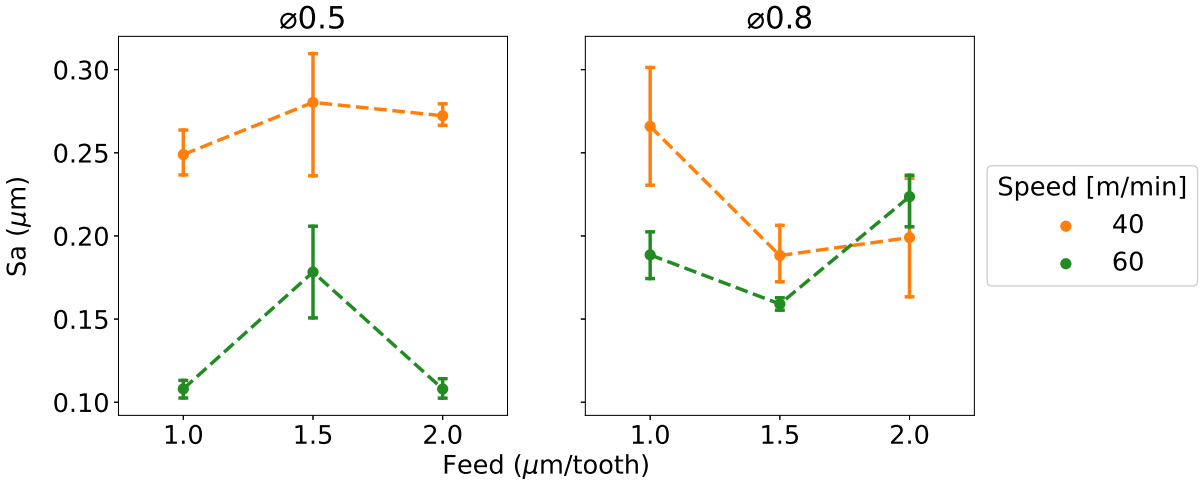

Figure 68: S_a average results for the conventional sample.

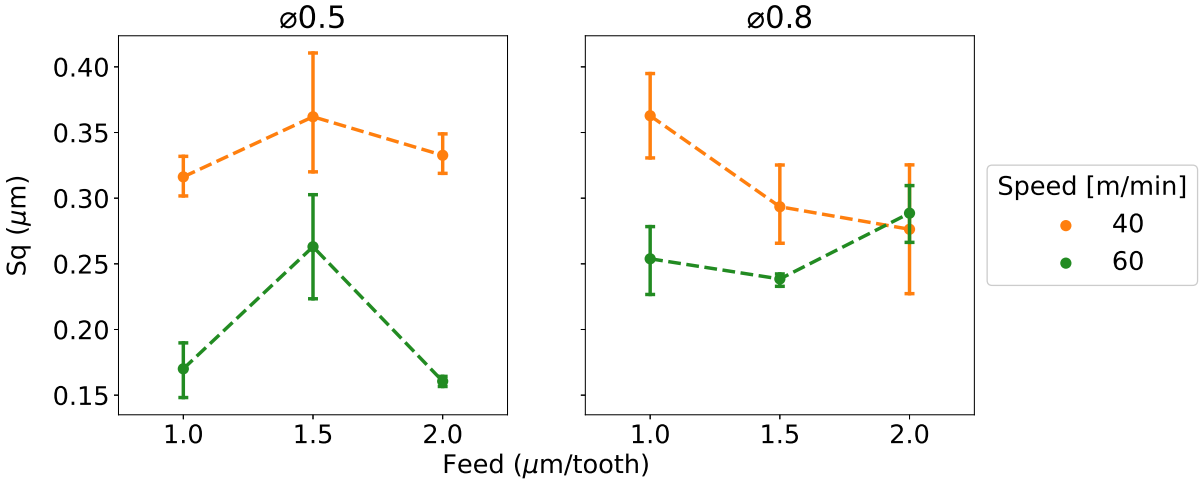

Figure 69: S_q average results for the conventional sample.

Table 18: Surface roughness results for the conventional sample.

Tool (mm)	**Feed (μm/tooth)**	V_c **(m/min)**	S_a **(μm)**	S_q **(μm)**
0.5	1	40	0.25 ± 0.02	0.32 ± 0.02
0.5	1	60	0.10 ± 0.01	0.17 ± 0.02
0.5	1.5	40	0.31 ± 0.01	0.36 ± 0.06
0.5	1.5	60	0.18 ± 0.02	0.26 ± 0.05
0.5	2	40	0.28 ± 0.01	0.33 ± 0.02
0.5	2	60	0.11 ± 0.01	0.16 ± 0.01
0.8	1	40	0.27 ± 0.04	0.36 ± 0.04
0.8	1	60	0.19 ± 0.01	0.25 ± 0.03
0.8	1.5	40	0.17 ± 0.01	0.29 ± 0.04
0.8	1.5	60	0.16 ± 0.01	0.24 ± 0.01
0.8	2	40	0.21 ± 0.06	0.28 ± 0.06
0.8	2	60	0.21 ± 0.02	0.29 ± 0.02

Indeed, the cutting speed affects the surface roughness, because the material removal rate increases with the increase of cutting speed [CHEN et al., 2014], what makes the surface smoother for higher velocities. Although, the relationship between the surface roughness and cutting speed is not analytical [ARAUJO; MOUGO; CAMPOS, 2021]. In addition, for micromilling operations it is not unusual to find works in which higher surface roughness were acquired for higher velocities, as in Wang, Kweon and Yang [2005] research. In this cases, the high frequencies vibration of the system can cause the surface quality to become lower for higher speeds.

Other major contributing factor to the final surface roughness is the tool diameter, as showed in literature [WANG; KWEON; YANG, 2005; MANSO et al., 2019]. In Wang, Kweon and Yang [2005] research, the surface roughness increased with tool diameter, what is due to the tool deformation that becomes bigger for smaller tool diameters. Nevertheless, no clear relationship between tool diameter and surface roughness could be observed in the tests from the present work. Although, the better surface finishing was achieved for the lower tool diameter combined with higher cutting speed.

Other observations about the surface can be made in regard to its height distributions (S_{sk} parameter) and its peaks and valleys geometries (S_{ku} parameter). The results of S_{sk} and S_{ku} are shown in Figures 70 and 71, respectively. Then, it can be concluded that for all experiments there was a peak predominance on the surface (since S_{sk} values are greater than zero). However, for the lower tool diameter, the S_{sk} values were distinctly greater for higher speed, which was not observed for the 0.8 mm tool diameter.

Furthermore, the S_{ku} results show a large amplitude variation of the peaks and valleys, in other words, the surface presented extreme peaks and valleys results. The same

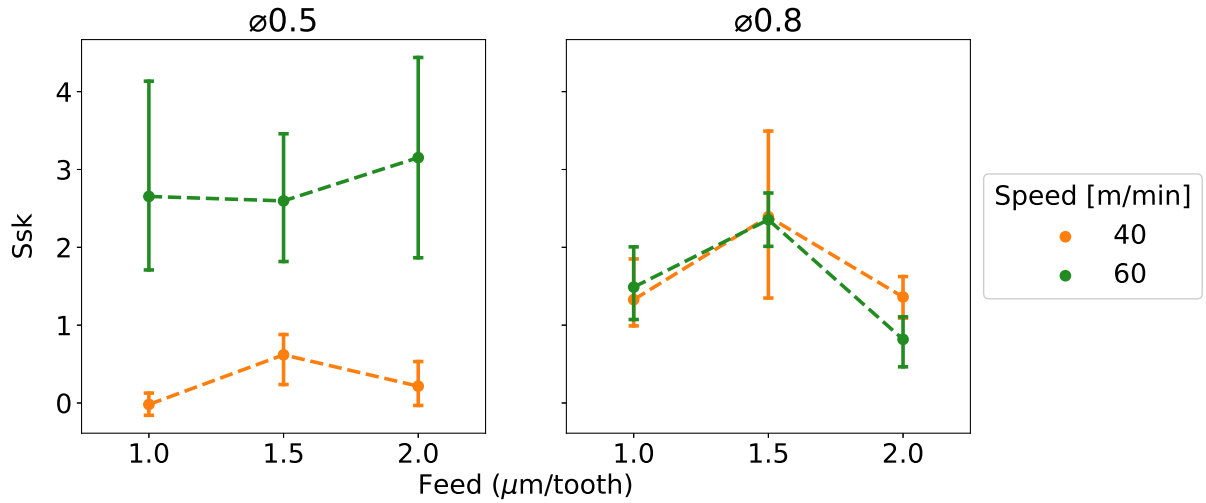

Figure 70: S_{sk} average results for the conventional sample.

way, the lower tool diameter presented higher S_{ku} values for higher speed. These results may have an influence of the chips left on the surface, that were not removed with the ultrasonic cleaning. This way, the surface presents extreme peaks and valleys results. For that reason, the S_v, S_p and S_z results were not considered in this analysis, since the measurements were not conclusive.

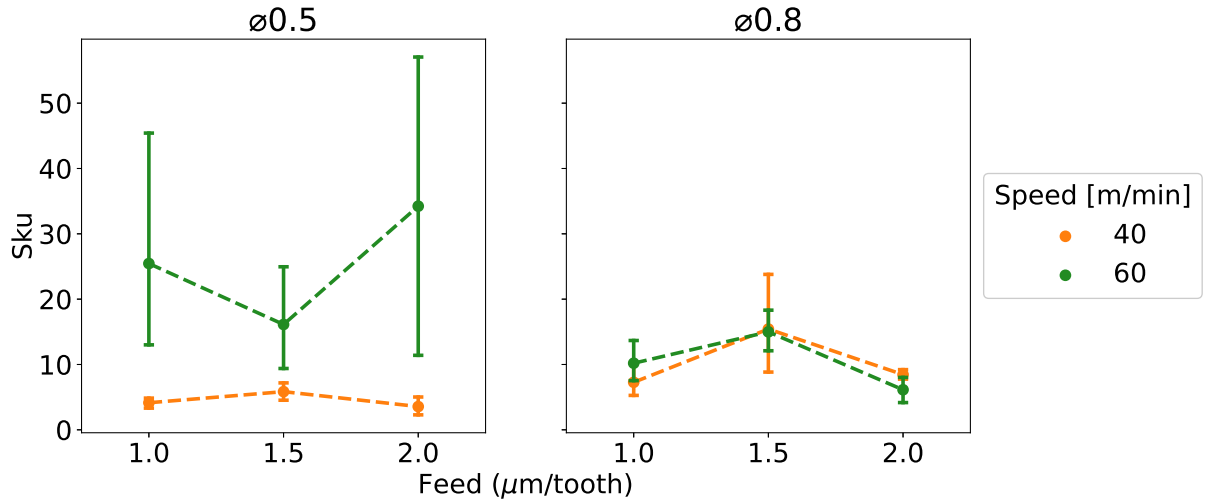

Figure 71: S_{ku} average results for the conventional sample.

In Figure 72 it is possible to see a 3D view comparison of the surface roughness for different speeds and different tool diameters for the feed of 2 μm/tooth.

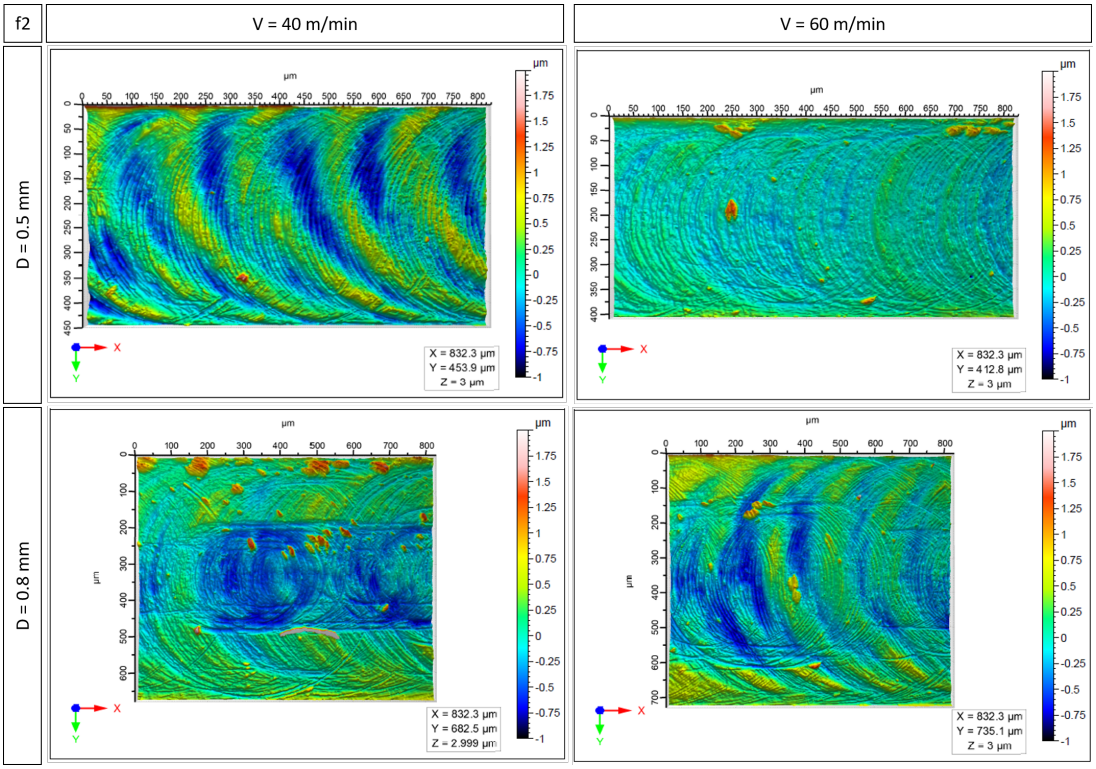

Figure 72: 3D surface images for f = 2 μm/tooth for the conventional sample.

4.2.2 Printed samples

The same way, the surface roughness was analyzed for each experiment on the printed samples. The average results graphs of the arithmetic mean of the area (S_a) and the root mean square height (S_q) are presented in Figures 73 and 74 and in Table 19. As it can be seen, the behavior of S_a and S_q maintains the same as for the conventional sample, since the surface roughness is increasing for lower speed, as expected.

As in the conventional sample, there is a peak predominance on the surfaces, which can be concluded by observing the S_{sk} results (Figure 75). Also, there is a large amplitude variation of the peaks and valleys for all experiments (Figure 76). The S_{sk} and S_{ku} were also distinctly greater for the highest speed for the smaller tool diameter.

From Figure 77, it can be seen that a better surface roughness was achieved for higher velocities, as observed with the S_a measurements. For this reason, and because of the left chips on the surface, the S_a roughness results are more reliable for analyzing the surface quality in this work. The better surface roughness for higher velocities maintains when feed is changed, but no relation between feed and surface roughness was observed.

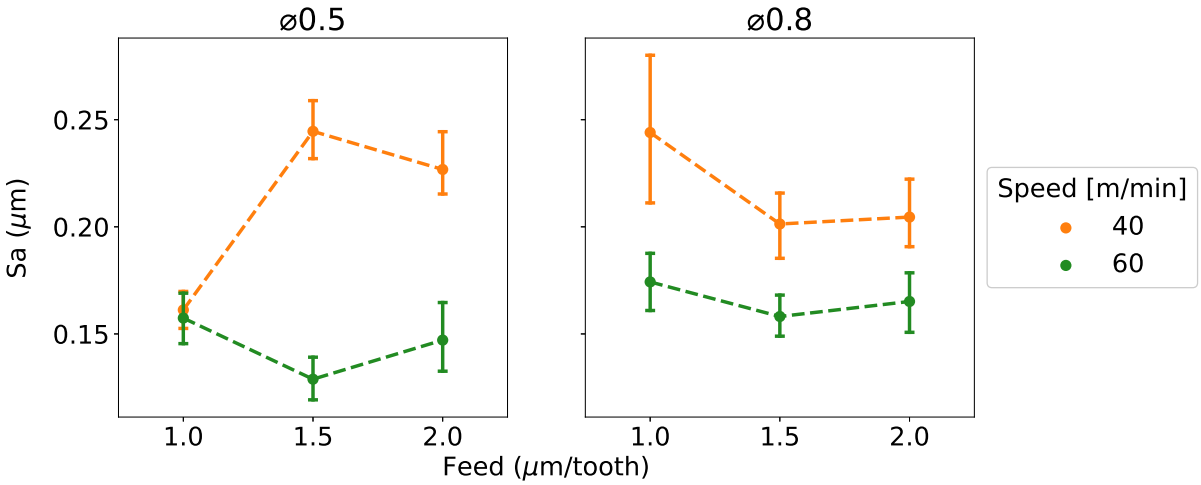

Figure 73: S_a average results for the printed samples.

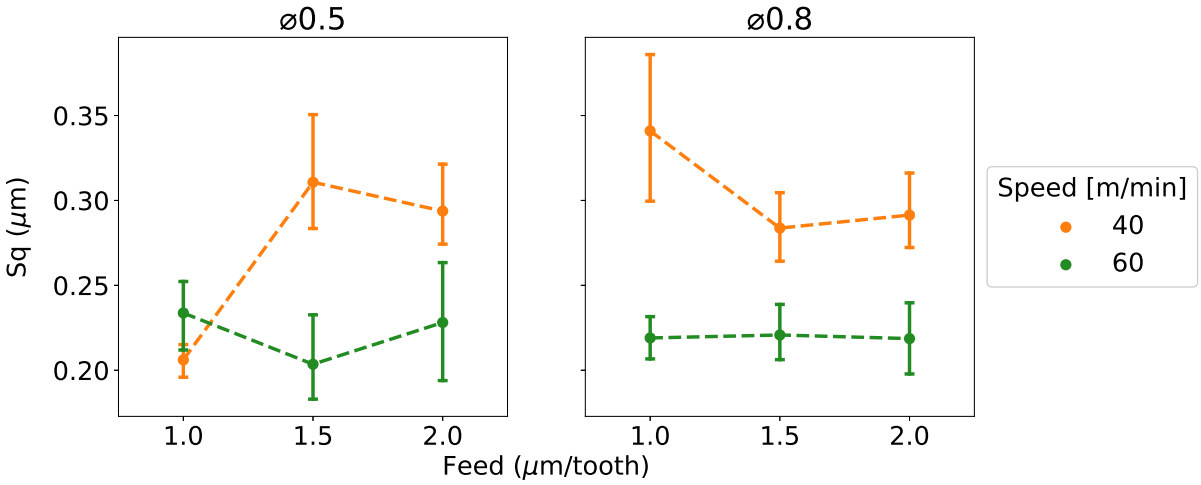

Figure 74: S_q average results for the printed samples.

Table 19: Surface roughness results for the printed samples.

Tool (mm)	**Feed (μm/tooth)**	V_c **(m/min)**	S_a **(μm)**	S_q **(μm)**
0.5	1	40	0.17 ± 0.02	0.20 ± 0.01
0.5	1	60	0.17 ± 0.01	0.23 ± 0.03
0.5	1.5	40	0.22 ± 0.01	0.32 ± 0.06
0.5	1.5	60	0.14 ± 0.02	0.21 ± 0.04
0.5	2	40	0.24 ± 0.03	0.28 ± 0.01
0.5	2	60	0.13 ± 0.01	0.22 ± 0.06
0.8	1	40	0.24 ± 0.01	0.32 ± 0.05
0.8	1	60	0.19 ± 0.01	0.21 ± 0.01
0.8	1.5	40	0.20 ± 0.02	0.28 ± 0.02
0.8	1.5	60	0.15 ± 0.01	0.22 ± 0.01
0.8	2	40	0.19 ± 0.01	0.30 ± 0.03
0.8	2	60	0.16 ± 0.01	0.21 ± 0.02

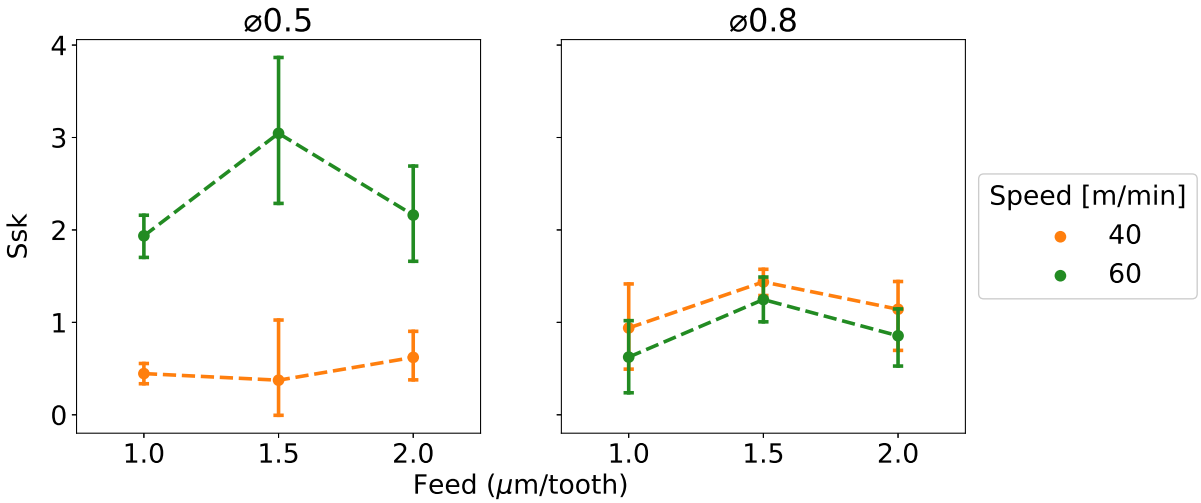

Figure 75: S_{sk} average results for the printed samples.

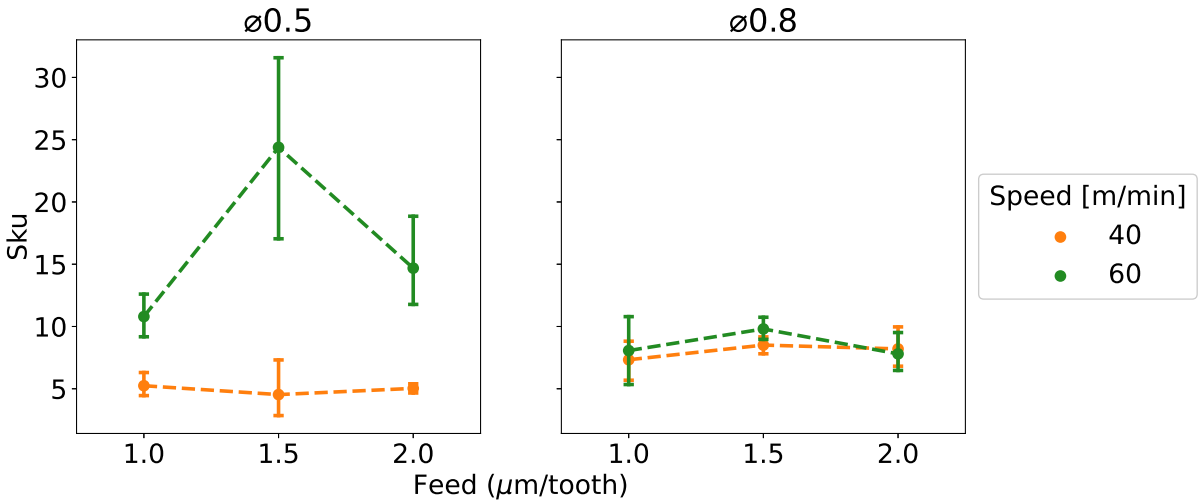

Figure 76: S_{ku} results for the printed samples.

4.2.3 Printed samples with heat treatment

To make a comparison between the results of the printed samples with and without heat treatment, some experiments were made considering the higher tool diameter and speed. As it can be seen from the S_a and S_q results presented in Figure 78 and in Table 20, the surface roughness for the printed allow without heat treatment was slightly higher.

In Figure 79, regarding the surface texture, it can be concluded that the surface presents a predominance of peaks ($S_{sk} > 0$), as observed for the conventional and printed alloys. Also, there is a presence of inordinately high peaks and/or deep valleys, which can present an interference of the chips left on the surface. Observing Figure 80, a

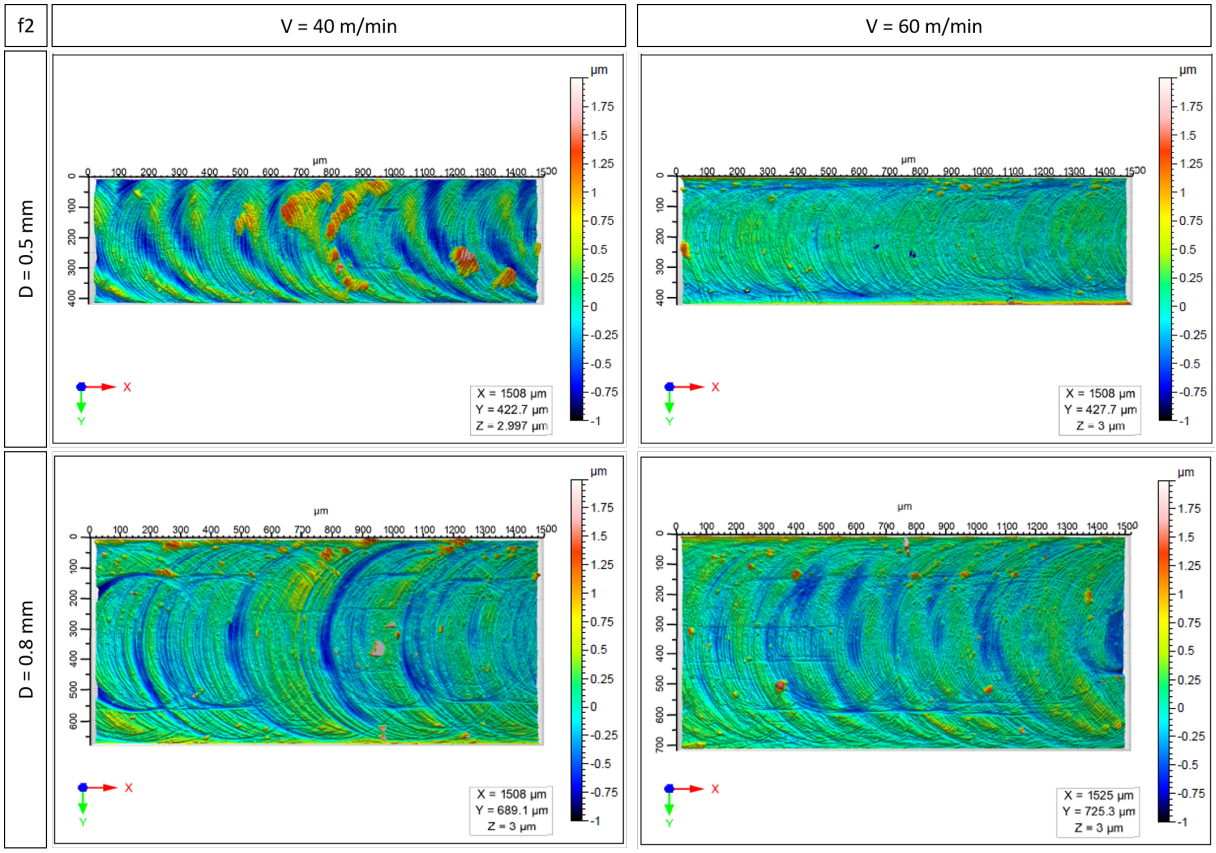

Figure 77: 3D surface images for f = 2 μm/tooth for the printed samples.

slight difference in terms of surface quality can be observed between the analyzed printed samples for the same micromilling conditions.

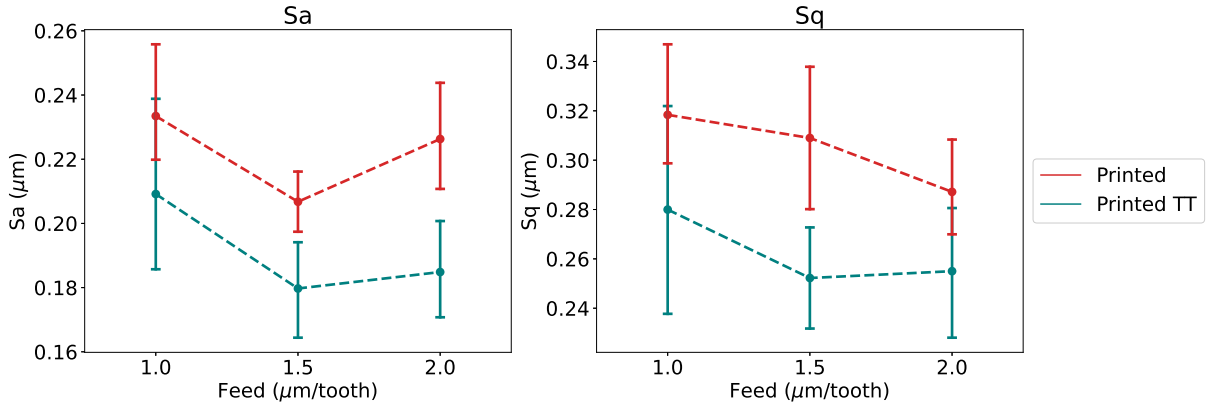

Figure 78: S_a and S_q results comparison between the printed sample with and without heat treatment for experiments with the 0.8 mm diameter tool and speed of 60 m/min.

Table 20: Surface roughness results for the printed samples with heat treatment.

Tool (mm)	**Feed (μm/tooth)**	V_c **(m/min)**	S_a **(μm)**	S_q **(μm)**
0.5	1	60	0.11 ± 0.01	0.20 ± 0.02
0.5	1	40	0.25 ± 0.01	0.36 ± 0.01
0.5	1.5	60	0.13 ± 0.01	0.22 ± 0.03
0.5	2	60	0.11 ± 0.01	0.23 ± 0.08
0.8	1	60	0.24 ± 0.03	0.32 ± 0.03
0.8	1.5	60	0.20 ± 0.01	0.31 ± 0.04
0.8	2	60	0.24 ± 0.01	0.29 ± 0.02

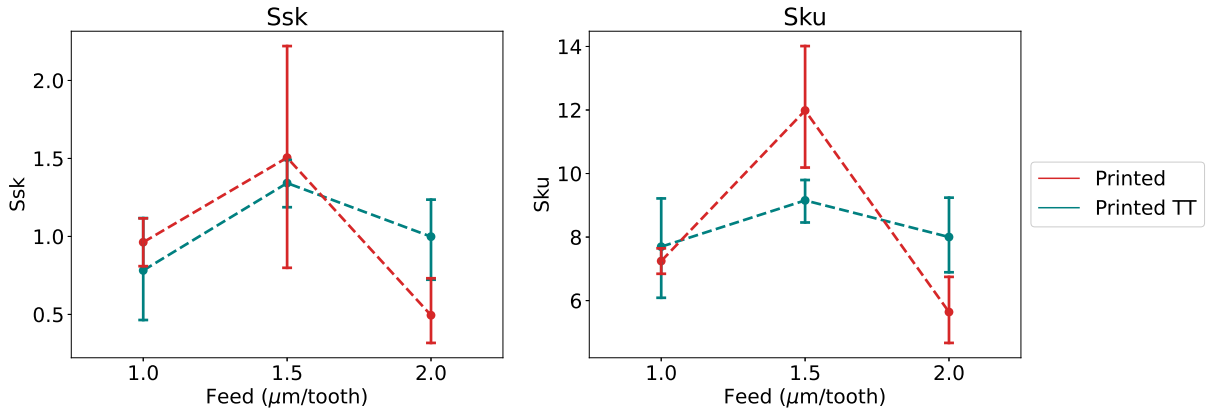

Figure 79: S_{sk} and S_{ku} results comparison between the printed sample with and without heat treatment for experiments with the 0.8 mm diameter tool and speed of 60 m/min.

4.2.4 Surface roughness results for Schaublin CNC experiments

The surface roughness results for the samples machined in the Schaublin CNC are shown in Figures 81 and 82. The same way as the previous surface roughness results, a better surface roughness was achieved for higher speeds, as cutting forces tend to be lower in this case. Also, if comparing the surface roughness S_a for the printed samples machined in the CNC Mini-mill (Figure 73), the surface roughness results were generally higher for the samples machined on the Schaublin CNC. This is addressed to this system robustness, that leads to higher system's vibration and instabilities, what damages surface quality. Figure 83 shows the 3D surface images of the machined samples.

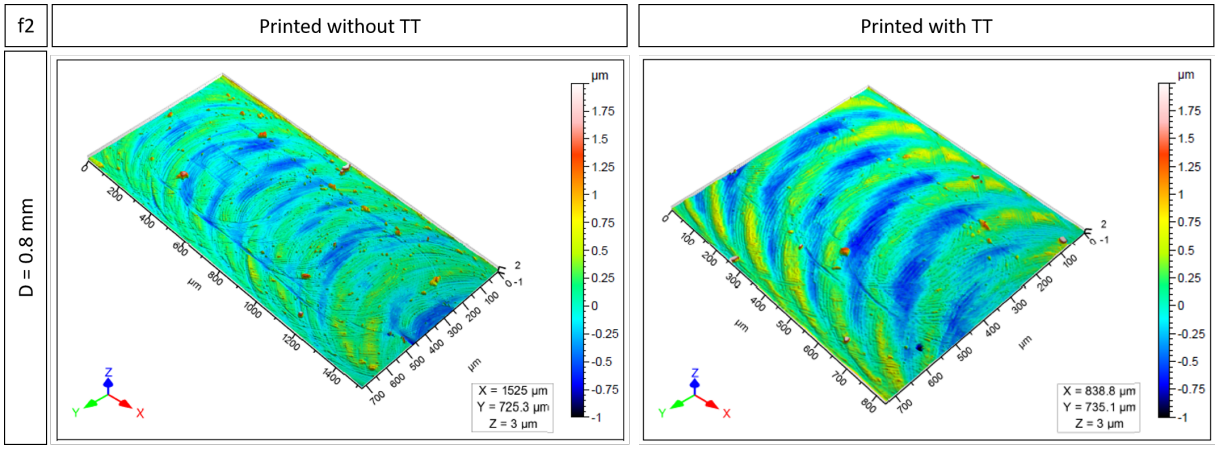

Figure 80: 3D surface images for for the printed sample with and without heat treatment for the cutting parameters of f = 2 μm/tooth, Vc = 60 m/min and D = 0.8 mm.

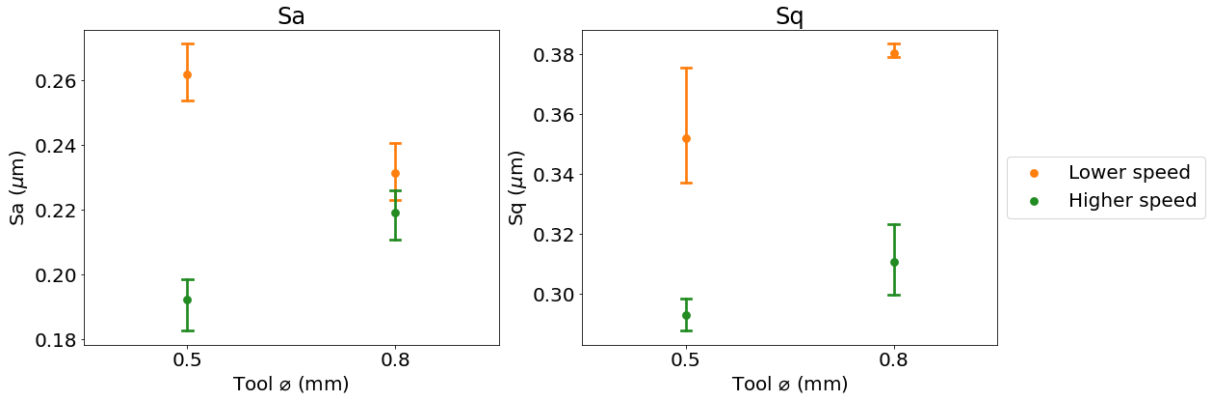

Figure 81: S_a and S_q results for the printed samples machined on the Schaublin CNC.

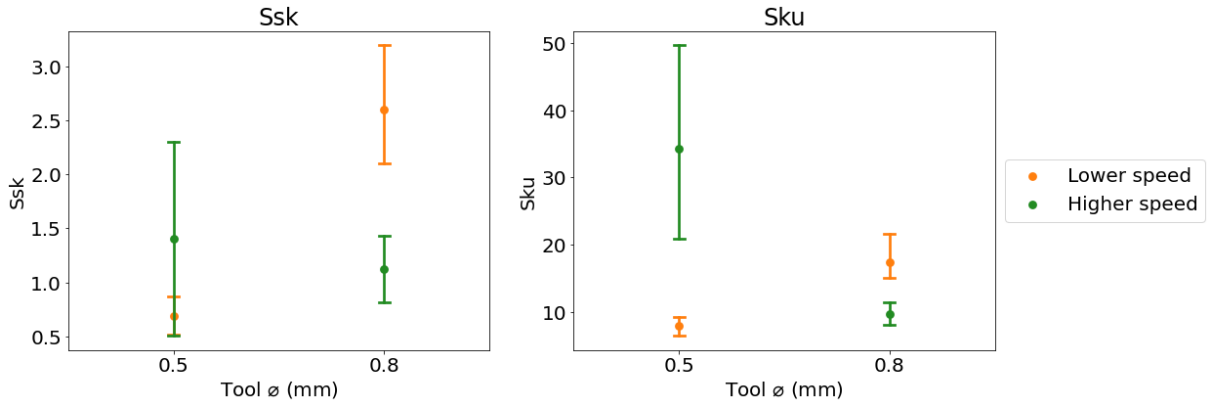

Figure 82: S_{sk} and S_{ku} results for the printed samples machined on the Schaublin CNC.

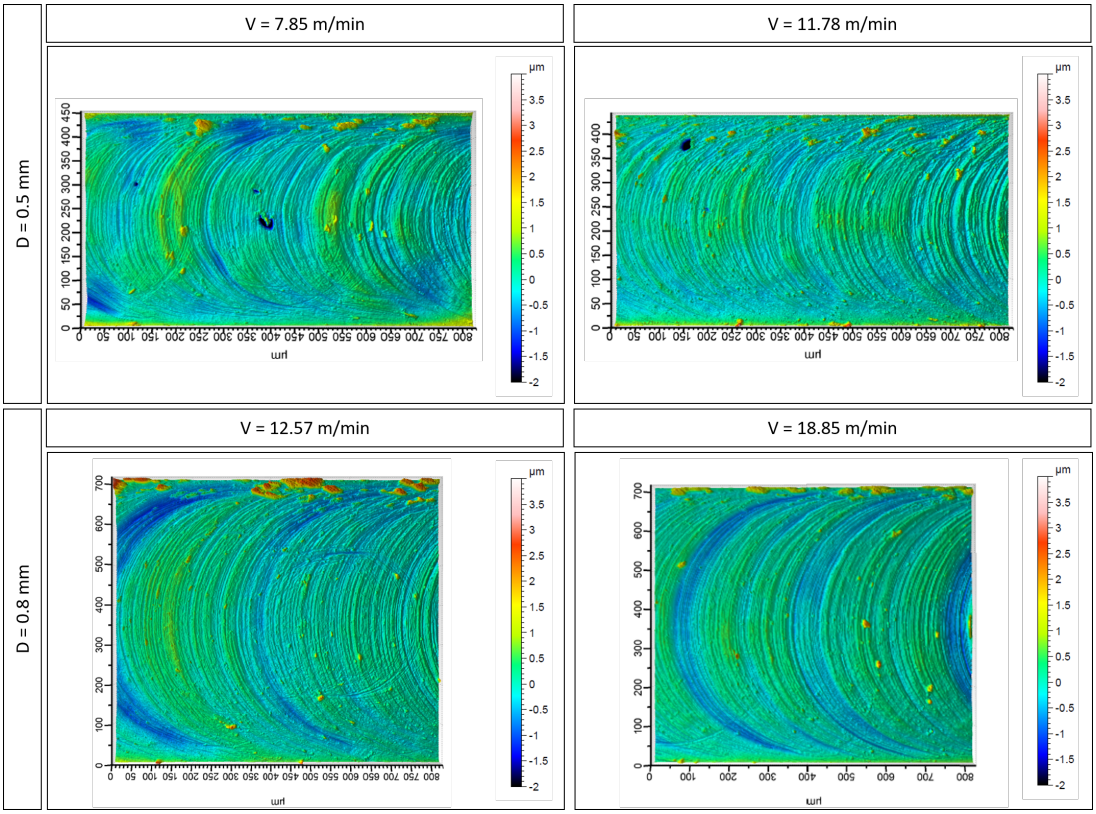

Figure 83: 3D surface images for f = 1 μm/tooth for the printed samples machined on the Schaublin CNC.

4.2.5 Cutting parameters influences on surface roughness data

Besides the comparisons already made, it is interesting to analyze the influence of the cutting parameters on the surface roughness of the materials. For that reason, the Pearson coefficient was calculated considering the roughness data acquired for all samples machined on the CNC Mini-mill and for the samples machined on the Schaublin CNC. These analyses were made to see if there was one particular parameter influencing the results the most. The results are shown in Figures 84 and 85, respectively. From that, it can be seen that the surface roughness was mostly influenced by cutting speed, with moderate to strong correlations for both cases. On the other hand, a negligible correlation of feed and tool diameter was found with regard to surface roughness. Indeed, as reported by other researchers, the cutting speed directly influences the surface roughness [PARHAD et al., 2015; SEKER; HASIRCI, 2006]. Since, at lower cutting speeds BUE formation increases, what deteriorates surface quality.

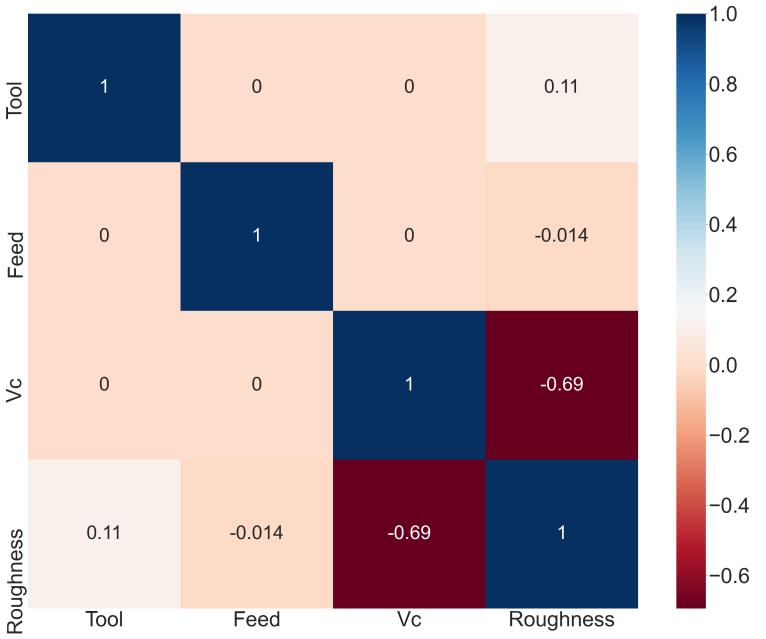

Figure 84: Heat map showing the correlation among surface roughness and the cutting parameters for the CNC Mini-mill experiments.

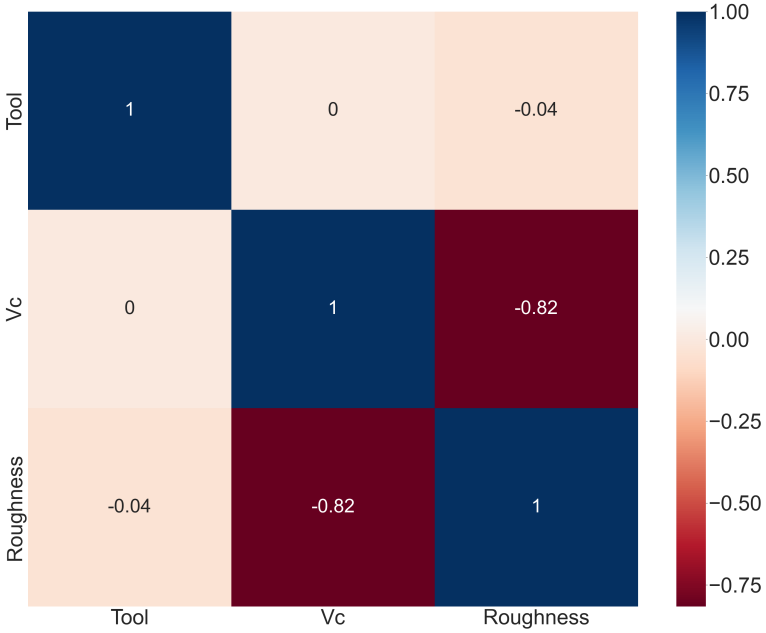

Figure 85: Heat map showing the correlation among surface roughness and the cutting parameters for the Schaublin CNC experiments.

4.3 Residual stress results

In the evaluation of surface integrity of machined components, residual stresses are the most critical response as it affects fatigue life of component [SAHU; ANDHARE, 2019]. The results of the residual stresses measured in this work are shown in Table 21. The RS obtained for all samples were compressive in nature, which have a positive effect on the component's life. Some experiments were also made in a surface of the material without the micromilling grooves. Although, there was no significant difference between the results of the surface with and without the micromilling grooves. This leads to the conclusion that the micromilling process does not significantly change the residual stresses of the material, due to this process low deformation energy storage.

Table 21: Residual stress results.

Sample	**Direction**	**Residual Stress (MPa)**
Conventional	Parallel	-967.398 ± 54
Conventional	Perpendicular	-505.947 ± 79
Printed	Parallel	-555.658 ± 77
Printed	Perpendicular	-642.602 ± 80
Printed HT	Parallel	-384.314 ± 35
Printed HT	Perpendicular	-317.216 ± 77

Figure 86 presents a better visualization of these results behavior. As expected, the heat treatment reduced the residual stresses of the printed material. This happens because the material yield strength is reduced as temperature increases, leading to microscopic plastic deformations inside the material, that results in stress relief [METALLURGISTS, 2021].

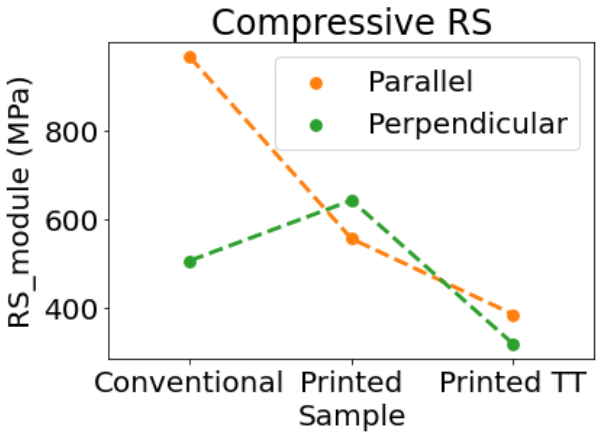

Figure 86: Residual stress results variation with samples.

In addition, the correlation analysis between the acquired residual stresses with the different samples and measurement direction is shown in Figure 87. In this analysis, the samples were enumerated as follows: (1) Conventional; (2) Printed; and (3) Printed HT. As it can be observed, the measured direction had a weak influence on the results, but the samples manufacturing process had a strong correlation to it. From that, it can be concluded that for higher sample's numeration, the compressive residual stresses reduced.

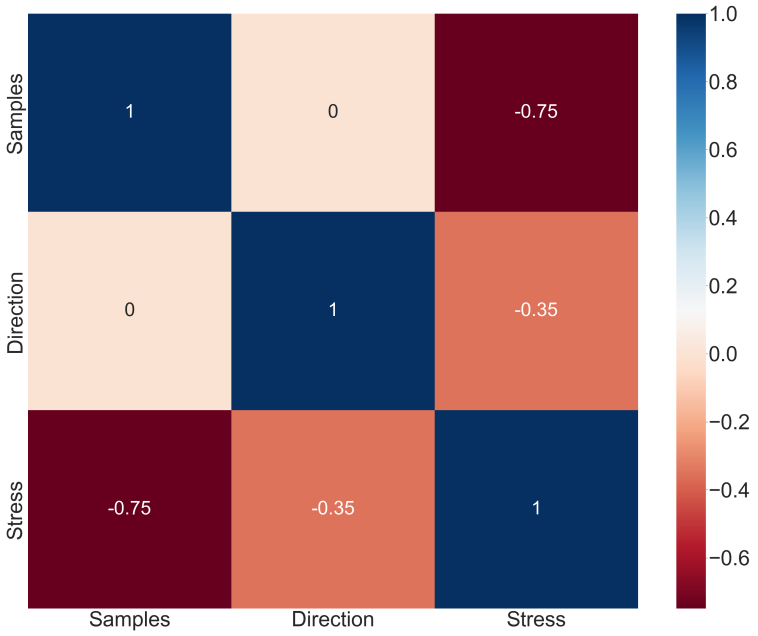

Figure 87: Heat map showing the correlation between the RS results, samples and measured direction.

4.4 Burr formation

Burr formation was observed through an estimative of its mean height and area. The results for each of these analysis are shown in the following sections.

4.4.1 Burr height results

Burr height is one of the main parameters to be analyzed in burr formation. For that reason, applying the CCI profilometer, burr height for the experiments done in the Mini-mill CNC was estimated. This estimation considered the mean burr height in an area of 800 × 800 μm. It should be noted that, in this work, the burr height stands for the distance from the bottom of the channel up to its maximum burr peak. In addition, burr height was measured on the up-milling side, as illustrated in Figure 88. For each experiment, the results obtained are shown in Table 22.

It should be pointed out that the burr height measurement is just an estimative of burr formation. During the measurements, due to the irregular surface generated by the top burr formation, the reflection of the laser beam is impaired, resulting in many unmeasured points in this region. Although, still, it is possible to see the burr peak from the results. From the results, it was found a correlation between the burr height and the tool size, meaning that for the bigger tool diameter, burr height tended to decrease (Figure 89).

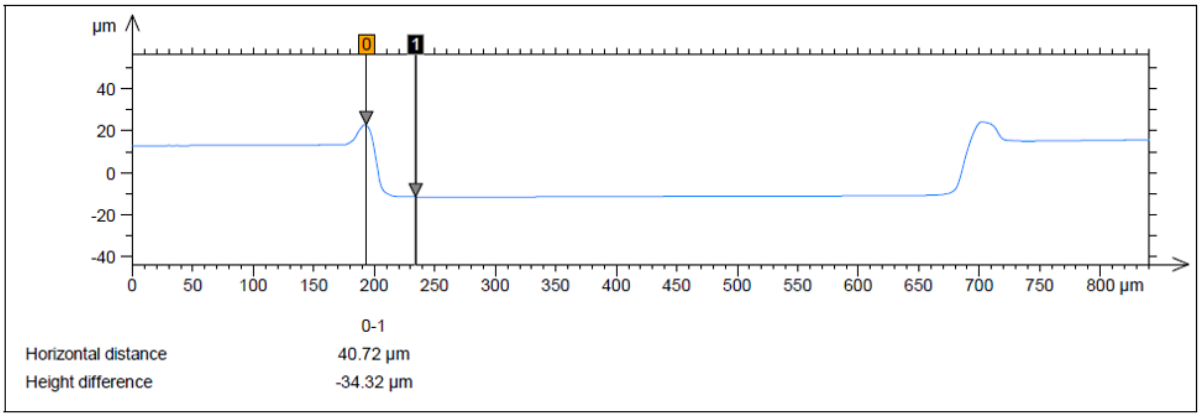

Figure 88: Mean burr height estimation for conventional sample with Vc = 60 m/min and fz = 1 μm/tooth.

Table 22: Burr height results.

Sample	V_c **(m/min)**	**Feed (μm/tooth)**	**Burr height (μm)**	
			⌀0.5 mm	**⌀0.8 mm**
Conventional	40	1	32.87	24.29
Conventional	40	1.5	23.22	18.25
Conventional	40	2	30.64	33.1
Conventional	60	1	34.32	34.91
Conventional	60	1.5	28.13	24.23
Conventional	60	2	34.86	23.52
Printed	40	1	28.07	6.435
Printed	40	1.5	24.04	5.55
Printed	40	2	25.14	7.179
Printed	60	1	26.84	4.126
Printed	60	1.5	24.94	3.296
Printed	60	2	24.58	10.35
Printed TT	60	1	38.12	39.71
Printed TT	60	1.5	51.24	13.55
Printed TT	60	2	41.61	31.87

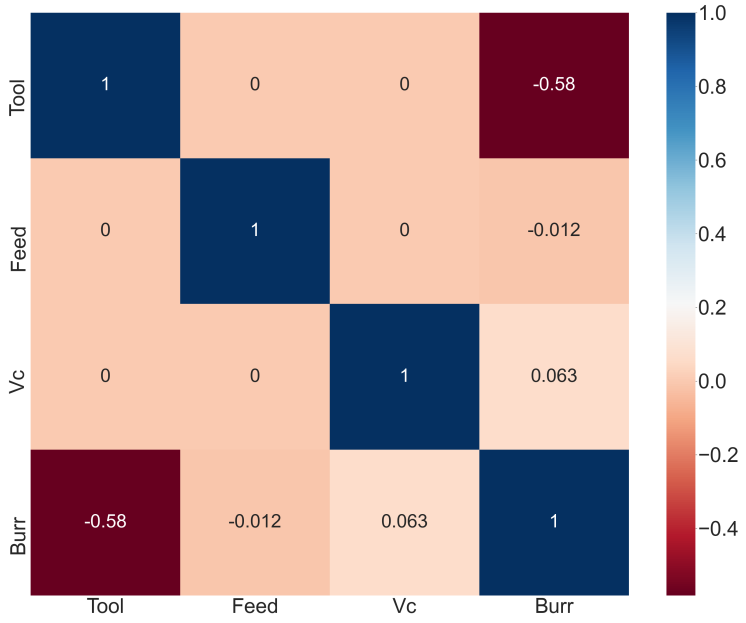

Figure 89: Heat map showing the correlation among cutting parameters and burr height.

4.4.2 Burr area results

For the experiments done in the Mini-mill CNC, the SEM images of the channels for each condition used are shown in Figures 90 and 91, for tool diameters of 0.5 and 0.8 mm, respectively. Aiming to quantify the burr area from these figures, ImageJ software was applied. From there, each image was separately scaled and converted into a binary image for making its analysis easier. This way, the burr stood highlighted (Figure 92) and its pixel's percentage was estimated, allowing an comparison between the acquired images.

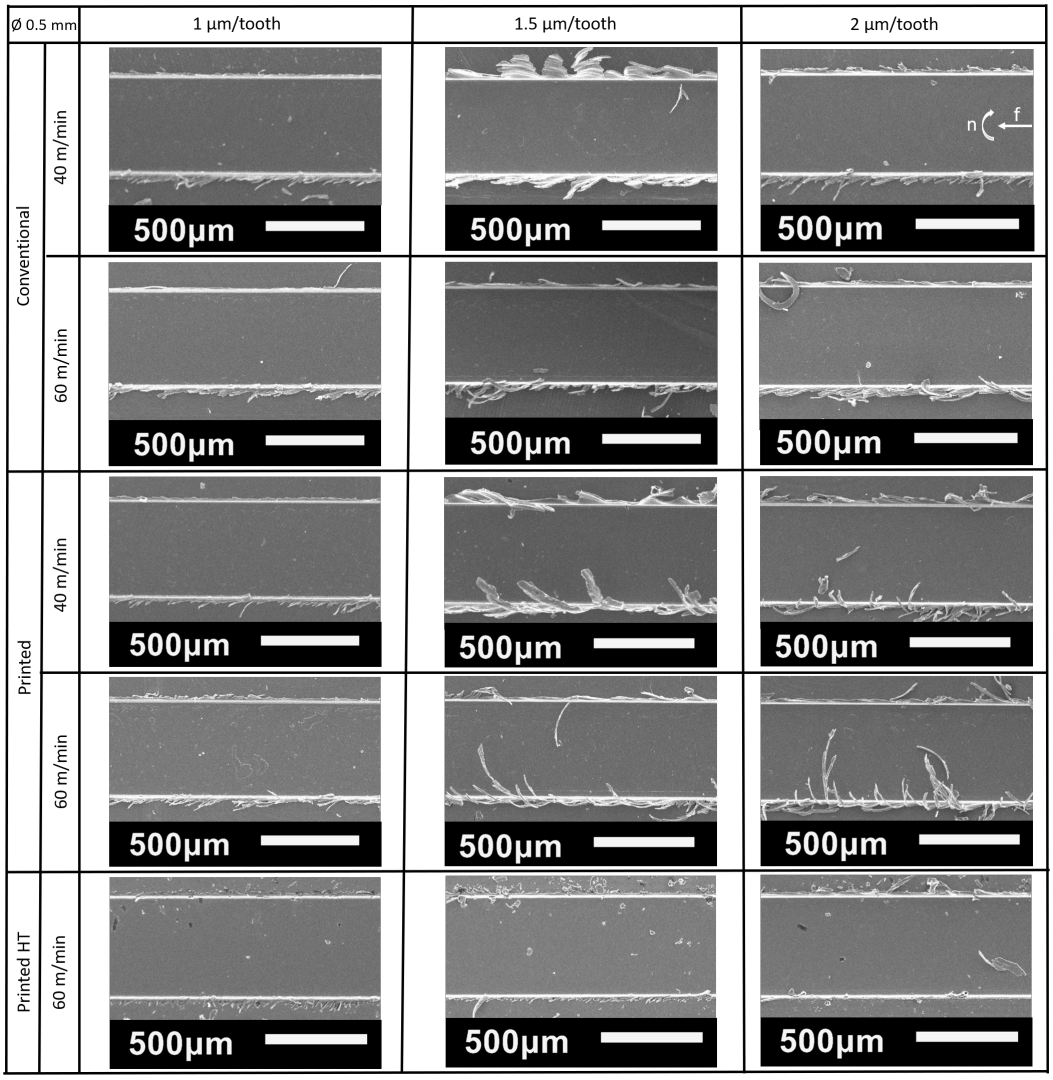

Figure 90: SEM images showing burr formation for each milling condition using the tool diameter of 0.5 mm.

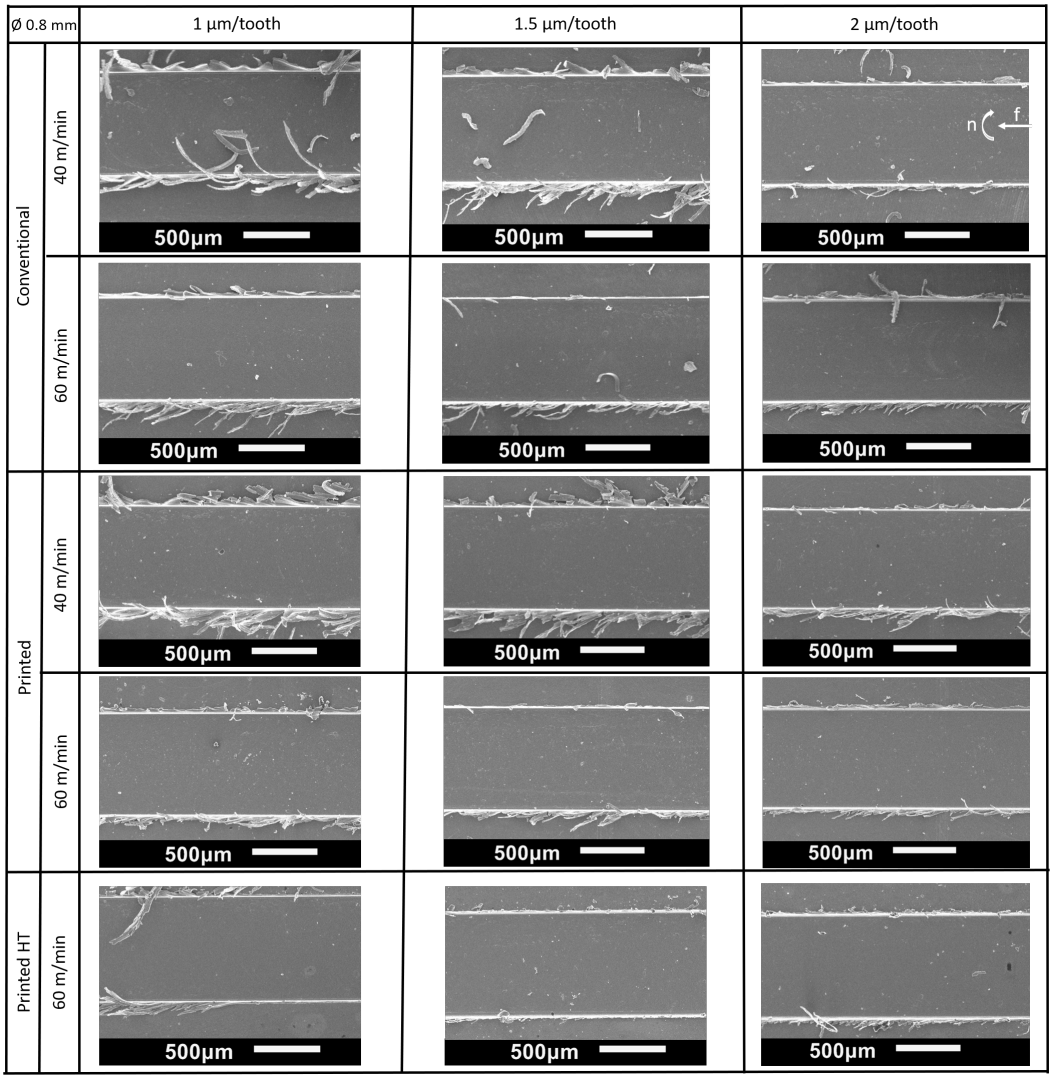

Figure 91: SEM images showing burr formation for each milling condition using the tool diameter of 0.8 mm.

(a) (b)

Figure 92: Illustration of the binary image used for estimating burr area. The images presented are from the: (**a**) conventional sample and (**b**) printed samples, both machined with the 0.5 mm tool diameter, Vc = 40 m/min and f = 1.5 μm/tooth.

Figure 92 presents the experiments where burr formation was higher considering the

0.5 mm diameter tool. These experiments also presented higher cutting force, as it can be seen from Tables 15 and 16, and worst surface finishing considering the lower tool diameter, as shown (Figures 68 and 73). Table 23 shows burr results for all experiments made.

Table 23: Burr area results.

Sample	V_c **(m/min)**	**Feed (μm/tooth)**	**Burr (%)**	
			⌀0.5 mm	**⌀0.8 mm**
Conventional	40	1	9.48	20.72
Conventional	40	1.5	19.13	16.30
Conventional	40	2	12.27	8.71
Conventional	60	1	10.43	14.04
Conventional	60	1.5	11.06	9.09
Conventional	60	2	14.64	11.29
Printed	40	1	10.26	19.99
Printed	40	1.5	21.55	15.75
Printed	40	2	17.09	9.86
Printed	60	1	11.47	11.90
Printed	60	1.5	13.72	8.14
Printed	60	2	16.76	10.50
Printed TT	60	1	10.96	12.14
Printed TT	60	1.5	11.66	8.37
Printed TT	60	2	13.14	10.92

Considering the top burr area results, and the feed forces results, it is possible to observe that there is a relation between them. The experiments where feed forces were higher presented higher burr formation (Tables 15, 16 and 17). This happens because the area of contact between the tip of the cutting tool and the feed force causes great stresses on the workpiece material, what compress the material, causing plastic deformation and resulting in the formation of Poisson type burrs [SILVA et al., 2015]. Indeed, top burrs are Poisson type burrs, that happens as a result of lateral deformation, as explained in Section 2.3.5.

In addition, this behavior had more impact for the smaller tool diameter, as it can be seen in the correlation analysis results made for feed forces and burr area (Figure 93). Although, no clear relation between burr area and feed could be established for the 0.8

mm tool diameter, since the correlation was weak. This behavior should be related to the variation in tool cutting edge radius for different tool sizes.

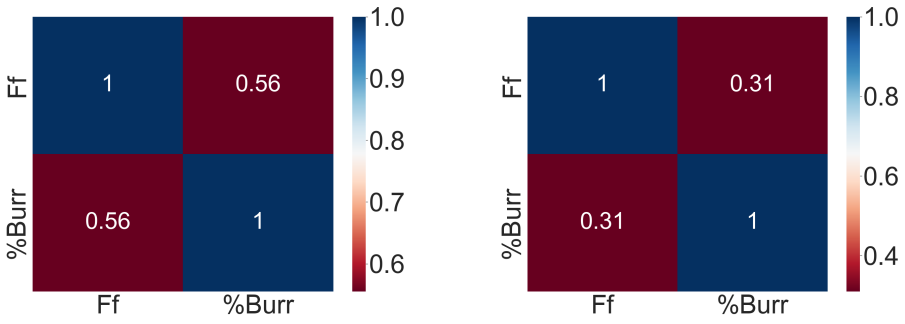

(a) (b)

Figure 93: Heat map showing the correlation between the feed forces and burr area results for: (**a**) 0.5 mm and (**b**) 0.8 mm tool diameters.

4.5 Burr area results for Schaublin CNC experiments

For the experiments made on the Schaublin CNC, image conversion was not possible. This way, the burr area was manually highlighted, as illustrated in Figure 94. From this analysis, the burr area obtained for each experiment, considering both up and down sides, is available in Table 24. These area results are not comparable to the ones made above, since the methodology changed. Since feed was kept constant in these experiments, no conclusions could be made regarding the feed forces results' influence on burr formation. Also, no relation was observed on burr area when varying cutting speed and tool diameter.

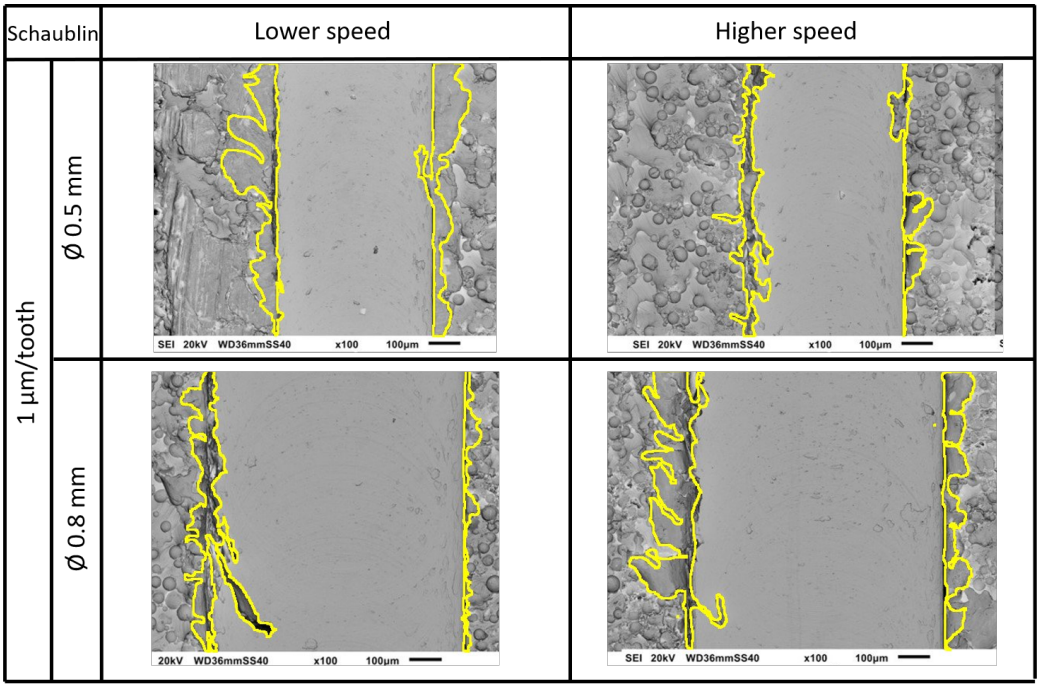

Figure 94: Burrs for the experiments made on the Schaublin CNC.

Table 24: Burr results for the Schaublin experiments.

Tool (mm)	**Feed (μm/tooth)**	V_c **(m/min)**	**Burr** ($\times 10^3 \mu m^2$)
0.5	1	7.85	118.2
0.5	1	11.78	66.8
0.8	1	12.57	74.2
0.8	1	18.85	128.1

4.6 Tool conditions

Cutting tools are made of brittle materials that can fail under excessive chip loading and fatigue due to cyclic thermal and mechanical stresses [YOUSSEF; EL-HOFY, 2008]. Therefore, right after each experiment on the CNC Mini-mill, a visual analysis of the tools used was performed with a SEM. Some of the images obtained for one tool of 0.5 mm and other of 0.8 mm are available in Figure 95.

As it could be observed from SEM images, there was no significant tool wear or damage on the tools. For this reason, the same tools were used for repeating the experiments on different samples. Although, for making one batch of experiments, twelve tools were used, but only after checking the tool conditions, the next batch was made. In this case, the tools were randomly chosen for making distinct experiments, which means that the same tool might have milled experiments of different cutting parameters. The replicas were also made with the same twelve tools.

In Figures 96 and 97 it is possible to better visualize the coating loss of the tools and some build up edge formation, which was observed in all experiments, in different ranges. In addition, even after ultrasonic cleaning, continuous chip formation were observed attached to the tools, specifically after milling the printed samples in high speeds. As an example, Figure 98 shows a continuous chip attached to one tool of 0.5 mm diameter after micromilling the printed sample with heat treatment with the highest speed.

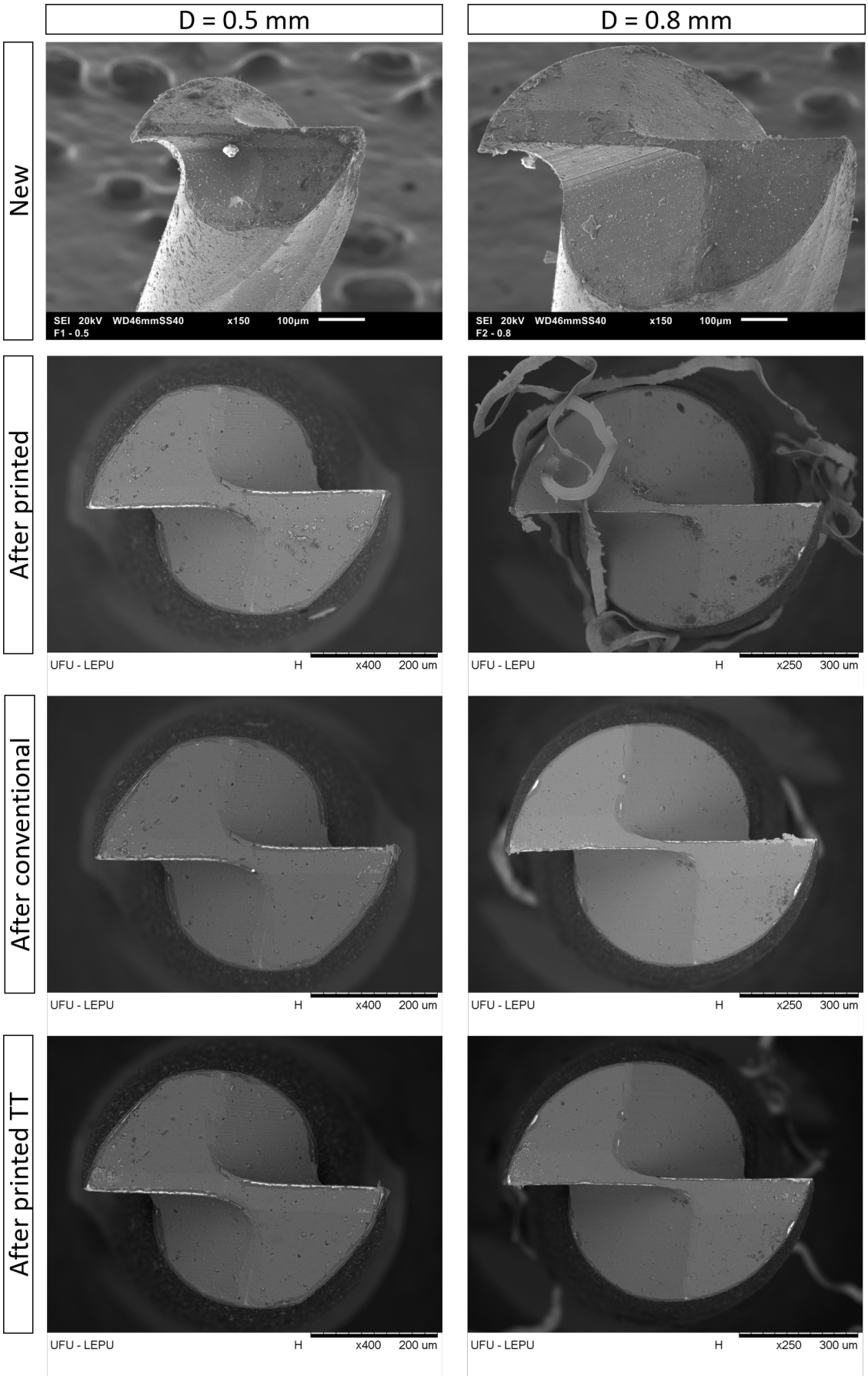

Figure 95: Tools after milling each sample

From observing the tools, it can be induced that they were protected due to BUE formation, specially for low speeds, though surface quality was impaired. In this case, the adherence between tool and workpiece is favored in lower speeds, since high compressive stresses hamper the material from sliding over the tool's rake face, what deteriorated surface quality [REIS; JUNIOR; MACHADO, 2007; KHORASANI et al., 2019; ABIDI, 2020]. Conversely, for high speeds, the BUE is reduced and a lower surface roughness is achieved. Also, the continuous chip formation is an indication of a better surface finishing, since this is a more stable process and no abrupt chip shear will affect the surface quality [ABIDI, 2020]. Although, long chips are not desired in machining process. Indeed, a lower surface roughness was observed for higher speeds during the machining of all different samples as presented in Section 4.2.

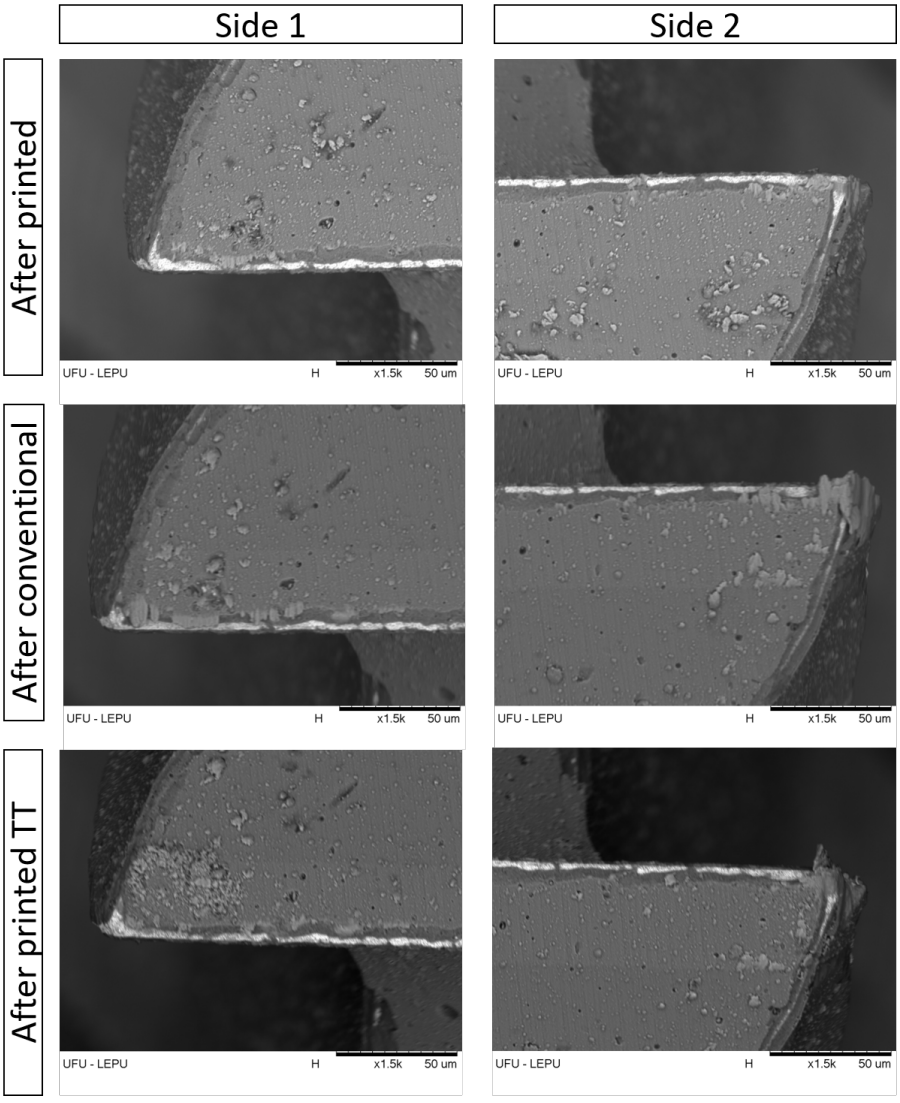

Figure 96: Tool sides after milling each sample (D = 0.5 mm, tool #1)

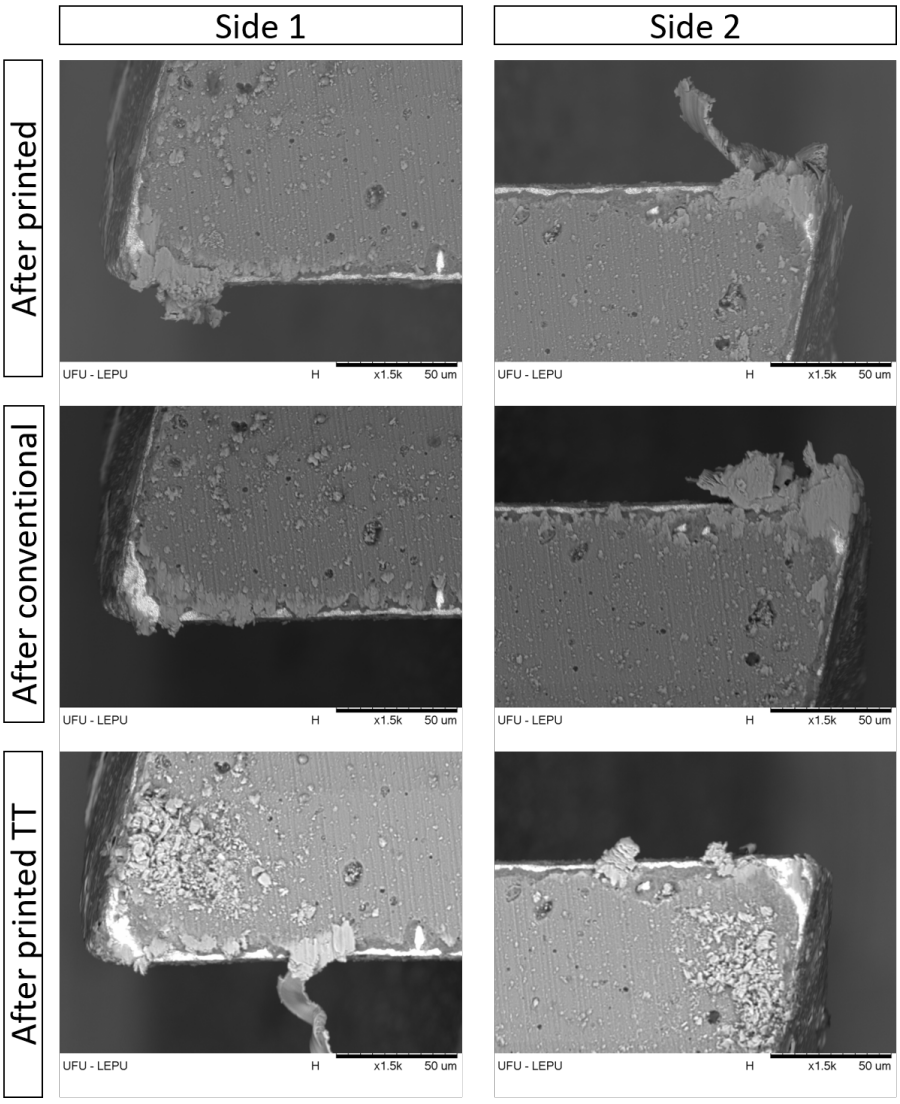

Figure 97: Tool sides after milling each sample (D = 0.8 mm, tool #3)

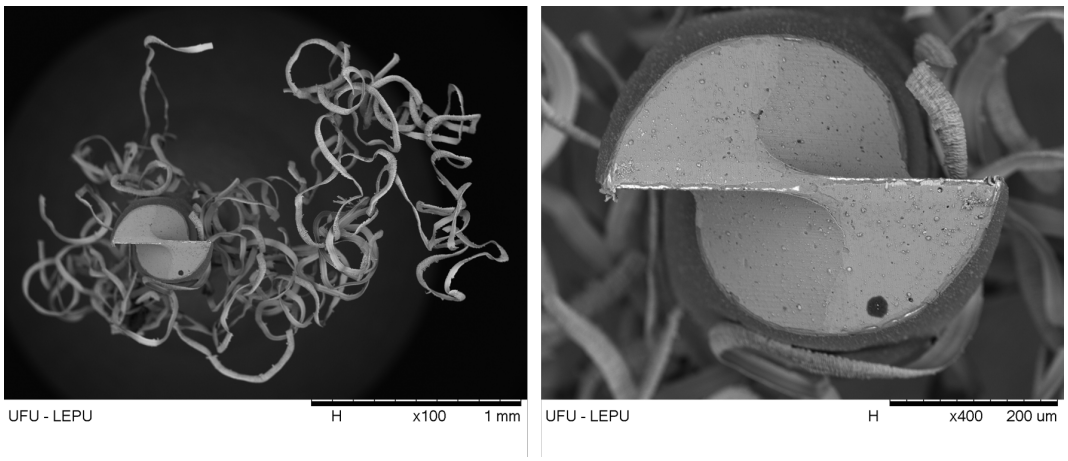

Figure 98: Chip formation after milling the printed TT sample (D = 0.5 mm, tool #2)

5 CONCLUSIONS

This work aimed to present a study in the area of micromilling 3D printed parts. For that, experiments were made in a CNC Mini-mill and in a conventional CNC machine, making comparisons between printed, printed with heat treatment and conventional Ti-6Al-4V samples. The main focus of this work was to compare the micromilling process regarding the manufacturing process and the two different systems used for the tests. The outcome variables analyzed were the cutting and feed forces, surface roughness, burr formation, and residual stresses. In addition, the characterization of the samples machined and tool conditions were presented.

In the initial analysis of the printed and conventional samples, it was possible to observe that their hardness measurements were according to what is predicted in literature, in the range of 30 - 41 HRC. The roughness of the samples varied according to the printing direction of the last layer, which is due to the anisotropy of the LPBF process. In this context, higher roughness was measured perpendicular to printing direction, which occurs due to the waviness caused by the action of the laser. Before machining, 3D surface roughness of the printed samples was measured, and the S_a mean value obtained was 22.02 μm.

Analyzing the samples' microstructure, a formation of α' martensite was observed on the printed samples, which is characteristic of the rapid cooling from the LPBF process. These thin martensites have a tight spacing that prevents displacement movement, resulting in a material of high strength and low ductility. Furthermore, this microstructure, which has columnar beta grains, favors intergranular failure of the alloy. For the conventional sample, an equiaxial microstructure was observed. Due to its small percentage of the lamellar matrix, this microstructure leads to a good material ductility.

With the micromilling forces results, it was possible to observe that the parameter that influenced the cutting forces the most was cutting speed. On the other hand, feed forces were more influenced by feed. In addition, no significant changes on cutting and feed forces are seen regarding the material manufacturing process. Since the printing

strategies applied for manufacturing the printed samples aimed to achieve mechanical properties results as close as possible to the conventional manufactured alloy, this behavior is understandable. Also, for the bigger diameter tool submitted to lower feed, rubbing and burnishing took place due to the scale effect and bigger tool nose radius. In this case, one tooth of the tool did not effectively cut the material, and in the action of the next edge, the material was removed. This behavior increased burr formation. In addition, tool run-out was observed in the experiments, because when measuring the channel width, it was few micrometers bigger than tool diameter.

From the experiments done in the Schaublin CNC it could be observed that the acquired cutting and feed forces were higher than the ones made in the Mini-mill CNC. This happens because the cutting speed used in the robust system was lower, due to this machine limitation. Also, it is important to consider that the dynamometer used for these experiments had lower sensitivity and that the machine was less precise. Although, from forces signals the action of each cutting edge of the tool was easily detected when zooming the data. In this case, the variable affecting the forces results the most was the tool diameter.

With the surface roughness analyses, it was observed that the best results were achieved with lower diameter tools and higher speeds. Indeed, the material removal rate increases with the increase of cutting speed, what makes the surface smoother for higher velocities. Regarding the surface's morphology, it can be concluded there it presents a peak predominance for all experiments, since S_{sk} values were greater than zero. Furthermore, the S_{ku} results showed that the surfaces obtained present extreme peaks and valleys, what can have an influence of the chips left on the surface, even after ultrasonic cleaning. Additionally, the surface roughness results did not change significantly with the different manufacturing process, though the S_a and S_q parameters were slightly higher for the printed samples without heat treatment.

For the experiments made on the robust system, the surface roughness achieved the same range (0.1 - 0.3 μm for S_a values) as the samples machined on the Mini-mill CNC. Although, the surface roughness results were generally higher for this set of experiments, what is due to this system's higher vibration and instabilities that damages surface quality. Even though, good surface roughness can be achieved by micromilling the samples in a conventional CNC machine, as it can be seen from the results presented in this dissertation. In addition, cutting speed was the parameter that influenced surface roughness the most, for all set of experiments. Since, at lower cutting speeds BUE formation increases, deteriorating surface quality.

The residual stresses results lead to the conclusion that the micromilling process does not significantly change the residual stresses of the material, due to this process low deformation energy storage. Also, compressive residual stresses were obtained for all samples, in accordance with literature. As expected, heat treatment reduced the residual stresses of the printed material.

From the burr formation estimative, it was possible to observe a correlation between feed forces and burr area results. As the feed forces were higher, burr tended to grow, as these forces causes great stresses on the workpiece, compressing the material and causing plastic deformation, what results in greater top burr formation.

Regarding the tool conditions, no significant tool wear or damage were observed. Although, coating loss and build up edge formation were observed. From that, it can be induced that the tools were protected due to BUE formation, specially for low speeds, though impairing surface quality. On the other hand, continuous chips were observed attached to the tool in higher speeds. This chip formation benefits surface finishing, since this is a more stable process and no abrupt chip shear will affect the surface quality. Indeed, a better surface roughness was observed for higher speeds during the machining of all different samples.

5.1 Future works

Since the micromilling process of printed materials is still under development, further research is needed to increment the knowledge about this topic. In future works, there is a need to analyze the influence of printing directions on the micromilling process, as well as to make the experiments in a wider range of cutting parameters. Furthermore, tests on other printed materials with featured applications are equally important and welcome.

Additionally, there is a need to approach an easy way to measure residual stress in microcomponents, that could also be applied for analyzing the residual stress in micromachining processes. Furthermore, studies regarding the micromilling process temperature and system vibration and stability would help to understand better the mechanisms happening during cut.

REFERENCES

ABBOUD, E. et al. Residual stresses and surface integrity of ti-alloys during finish turning – guidelines for compressive residual stresses. *3rd CIRP Conference on Surface Integrity (CIRP CSI)*, 2016.

ABIDI, Y. Relationship between surface roughness and chip morphology when turning hardened steel. Production Engineering Archieves, v. 26(3), p. 92–98, 2020.

ADVANCED CHEMICAL ETCHING. *Etching of Titanium Alloys*. United Kingdom, 2015. 3 p. Available from internet: ⟨https://ace-uk.net/knowledge-base/titanium-etching-whitepaper/⟩.

ALTINTAS, Y. *Manufacturing Automation: metal cutting mechanics, machine tool vibrations, and CNC design*. [S.l.]: Cambridge University Press, 2012.

AMERICAN SOCIETY FOR TESTING AND MATERIALS. *F3001-14*: Standard specification for additive manufacturing titanium-6 aluminum-4 vanadium eli (extra low interstitial) with powder bed fusion. ASTM International, West Conshohocken, PA, 2014.

AMERICAN SOCIETY FOR TESTING AND MATERIALS. *ASTM52900-15*: Standard terminology for additive manufacturing—general principles—terminology. ASTM International, West Conshohocken, PA, 2015.

AMERICAN SOCIETY FOR TESTING AND MATERIALS. *F3302-18*: Standard for additive manufacturing – finished part properties – standard specification for titanium alloys via powder bed fusion. ASTM International, West Conshohocken, PA, 2018.

AMIT, P. et al. Machining challenges in Ti-6Al-4V - a review. *International Journal of Innovations in Engineering and Technology (IJIET)*, v. 5, p. 6–23, 2015.

ANTONIALLI, A. I. S. *Uma contribuição ao fresamento frontal da liga de titânio Ti6Al4V*. Thesis (PhD) — Unicamp, 2009.

ARAUJO, A. C.; MOUGO, A. L.; CAMPOS, F. de O. *Usinagem para engenharia: um curso de mecânica do corte*. [S.l.]: E-papers, 2021. 360 p. ISBN 9786587065045.

ASLANTAS, K.; EKICI, E.; ÇIÇEK, A. Optimization of process parameters for micro milling of Ti-6Al-4V alloy using Taguchi-based gray relational analysis. Measurement, v. 128, p. 419–427, 2018.

ASSOCIAÇÃO BRASILEIRA DE NORMAS TÉCNICAS. *NBR 8404*: Indicação do estado de superfícies em desenhos técnicos - procedimento. [S.l.], 1984. 10 p.

ATTANASIO, A. Tool run-out measurement in micro milling. *Micromachines*, v. 8(7):221, p. 1–16, 2017.

ATTANASIO, A. et al. Influence of material microstructures in micromilling of Ti6Al4V alloy. *Materials*, v. 6, p. 4268–4283, 2013.

BALDO, D. *Estudo do microfresamento da liga de titânio Ti-6Al-4V utilizando análise de sinais de força e emissão acústica*. Master's dissertation — Departamento de Engenharia Mecânica, Universidade Federal de São João Del-Rei, 2013.

BARNES, J. E.; KINGSBURY, A. B. Does *Low Cost* titanium powder yield low cost titanium parts? PowderMet 2016 International Conference on Powder Metallurgy, Boston, MA, 2016.

BHAVAR, V. et al. A review on powder bed fusion technology of metal additive manufacturing. 4th International conference and exhibition on Additive Manufacturing, Banglore, India, 2014.

BIJANZAD, A.; KUZU, A. T.; BAKKAL, M. Influence of MQL on tool wear in CGI turning. Istanbul Technical University, 2014.

BORDINASSI, E. C. *Contribuição ao estudo da integridade superficial de um aço inoxidável super-duplex após usinagem*. Thesis (PhD) — USP, 2006.

BREMEN, S.; MEINERS, W.; DIATLOV, A. Selective laser melting. *Laser Journal*, v. 2, p. 33–38, 04 2012.

BRINKSMEIER, E. et al. Residual stresses - measurement and causes in machining processes. *Annals of the CIRP*, v. 31, p. 491 – 510, 1982.

CAMPOS, F.; ARAUJO, A.; KAPOOR, S. Experimental comparison of micromilling pure titanium and Ti-6Al-4V. Journal of Micro- and Nano-Manufacturing, v. 7(2), p. 6, 2019.

CAMPOS, F. O. *Estudo das forças de corte no microfresamento da liga de alumínio 6351-T6*. Thesis (PhD) — UFRJ - Universidade Federal do Rio de Janeiro, 2014.

CHAE, J.; PARK, S.; FREIHEIT, T. Investigation of micro-cutting operations. *International Journal of Machine Tools and Manufacture*, v. 46, p. 313–332, 2006.

CHEN, L. Y. et al. Anisotropic response of Ti-6Al-4V alloy fabricated by 3D printing selective laser melting. Materials Science & Engineering A, v. 682, p. 389–395, 2017.

CHEN, X. et al. Experimental study and genetic algorithm-based optimization of cutting parameters in cutting engineering ceramics. The International Journal of Advanced Manufacturing Technology, v. 74, p. 807–817, 2014.

CHIA, H. N.; WU, B. M. Recent advances in 3D printing of biomaterials. Journal of Biological Engineering, v. 9(4), 2015.

CILAS. *Escolhendo a melhor teoria na Difração a Laser Mie ou Fraunhofer*. 2020. Available from internet: ⟨http://www.acilweber.com.br/wp-content/uploads/2017/07/escolhendo-a-melhor-teoria-na-difracao-a-laser-mie-ou-fraunhofer.pdf⟩. Access: August 2020.

CIMM. *Definição - O que é fresamento*. 2018. Available from internet: ⟨http://www.cimm.com.br⟩. Access: May 2018.

COELHO, R. T.; SILVA, E. J. *Força e potência de corte em torneamento*. 2018. Available from internet: ⟨https://docplayer.com.br/213648461-Forca-e-potencia-de-corte-em-torneamento.html⟩. Access: April 2021.

COZ, G. L. et al. Micro cutting of Ti-6Al-4V parts produced by SLM process. Procedia CIRP, v. 58, p. 228–232, 2017.

CUNHA, D. F. *Influência da utilização do fluido de corte com adição de grafeno na temperatura de usinagem e formação de rebarba no processo de microfresamento*. Thesis (PhD) — Faculdade de Engenharia Mecânica, Universidade Federal de Uberlândia, 2016.

DABROWSKI, R. The kinetics of phase transformations during continuous cooling of the Ti6Al4V alloy from the single-phase β range. Archives of Metallurgy and Materials, v. 56, 2011.

DEVORE, J. *Probabilidade e estatística para engenharia e ciências*. Cengage Learning Edições Ltda., 2010. ISBN 9788522109241. Available from internet: ⟨https://books.google.com.br/books?id=0dojnQAACAAJ⟩.

DIB, M. H. M.; DIAS, D. G.; JASINEVICIUS, R. G. Análise das forças de usinagem durante a formação do cavaco em microfresamento. COBEF, Joinville – SC, 2017.

DMITRIYEV, T. et al. 3D printing as an alternative method of alloys obtaining. Chemistry Journal of Kazakhstan, v. 1(57), 2017.

DOBRZAŃSKI, L. A. *Metalowe Materiały Inżynierskie*. [S.l.]: Wydawnictwa Naukowo-Techniczne, 2009.

DONACHIE, M. J. *Titanium - A Technical Guide*. [S.l.]: ASM International, 1988. 13-15 p.

DUCATO, A. et al. An automated visual inspection system for the classification of the phases of Ti-6Al-4V titanium alloy. CAIP, v. 8048, p. 362–369, 2013.

FARIAS, A. de. *Análise da tensão residual e integridade superficial no processo de torneamento em material endurecido do aço ABNT 8620 cementado*. Master's dissertation — Universidade de São Paulo, 2009.

FEDRIGO, G.; JUNIOR, M. W. Avaliação da microestrutura da liga de titânio Ti6Al4V após tratamento térmico de envelhecimento. *VI SECITEC 2017*, p. 21–29, 2017.

FOREGS. *Ti - Titanium*. 2018. Available from internet: ⟨https://weppi.gtk.fi/publ/foregsatlas⟩. Access: April 2018.

FREESE, H. L.; VOLAS, M. G.; WOOD, J. R. *Metallurgy and Technological Properties of Titanium and Titanium Alloys*. [S.l.]: Springer, 2001. 25-51 p.

FRKAN, M. et al. Microstructure and fatigue performance of SLM-fabricated Ti6Al4V alloy after different stress-relief heat treatments. 13th International Scientific Conference on Sustainable, Modern and Safe Transport (TRANSCOM), p. 24–29, 2019.

GADDAM, R. et al. Study of alpha-case depth in Ti-6Al-2Sn-4Zr-2Mo and Ti-6Al-4V. *Materials Science and Engineering*, v. 48, p. 8, 2013.

GILLESPIE, L. K. *Burrs produced by end milling*. Kansas City, 1976. 121 p.

GONÇALVES, M. C. C. et al. Análise de amostras da liga de titânio Ti6Al4V impressas por fsl para ensaios de microfresamento. *39º SENAFOR*, Porto Alegre - RS, 2019.

GOWRI, S. et al. Micromachining: technology for the future. *International Journal of Materials and Structural Integrity*, v. 1, p. 161–179, 2007.

GRZESIAK, D.; KRAWCZYK, M. Effects of the selective laser melting process parameters on the functional properties of the co-cr alloy. *International Journal of Recent Contributions from Engineering, Science & IT*, v. 3, p. 39–42, 03 2015.

GU, D. et al. Laser additive manufacturing of metallic components: materials, processes and mechanisms. *International Materials Reviews*, v. 57, p. 133–164, 11 2015.

GUNDERSON, B.; WEST, B. T.; SHEDDEN, K. *Beyond Means: Sampling Distributions of Other Common Statistics*. 2020. Available from internet: ⟨https://www.coursera.org/lecture/understanding-visualization-data/beyond-means-sampling-distributions-of-other-common-statistics-JHPyP⟩. Access: August 2020.

INTERNATIONAL ORGANIZATION FOR STANDARDIZATION. *ISO 13320-1:1999: Particle size analysis Laser diffraction methods - Part 1: General principles*. Geneva, 1999.

JAFFERY, S. H. I. et al. Statistical analysis of process parameters in micromachining off Ti-6Al-4V alloy. *Journal of Engineering Manufacture*, v. 230(6), p. 1–18, 2015.

KHORASANI, A. M. et al. The effect of SLM process parameters on density, hardness, tensile strengthand surface quality of Ti-6Al-4V. *Additive Manufacturing*, v. 25, p. 176–186, 2019.

KILICKAP, E.; YARDIMEDEN, A.; ÇELIK, Y. Mathematical modelling and optimization of cutting force, tool wear and surface roughness by using Artificial Neural Network and Response Surface Methodology in milling of Ti-6242S. *Applied Sciences*, v. 7, p. 1–12, 2017.

KISTLER. *4-8-Channel Laboratory Charge Amplifier with LCD*. 2021. Available from internet: ⟨https://www.kistler.com/en/product/type-5070a/⟩. Access: October 2021.

KISTLER. *Compact Multi-Component Dynamometer*. 2021. Available from internet: ⟨https://www.kistler.com/pt/product/type-9119aa1/?application=33⟩. Access: October 2021.

KISTLER GROUP. *MiniDyn Type 9256C - Data sheet*. Switzerland, 2003.

KISTLER GROUP. *Cutting Force Measurements: Precise Systems for Metal Cutting*. Switzerland, 2017.

KOK, Y. et al. Anisotropy and heterogeneity of microstructure and mechanical properties in metal additive manufacturing: A critical review. *Materials and Design*, v. 139, p. 565–586, 2018.

KOLLI, R. P.; DEVARAJ, A. A review of metastable beta titanium alloys. *Metals*, v. 8(7):506, 2018.

KÖNIG, W. *Fertigungsverfahren: Drehen, Fräsen, Bohren*. Düsseldorf: VDI-Verlag, 1990. 417 p.

KOU, Z. et al. Burr Controlling in Micro Milling with Supporting Material Method. 43rd Proceedings of the North American Manufacturing Research, v. 1, p. 501–511, 2015.

KRUTH, J. P. et al. Binding mechanisms in selective laser sintering and selective laser melting. *Rapid Prototyping Journal*, v. 11, p. 26–36, 2005.

KUMMAMKANDATH, A. et al. Investigation on residual stresses in milling of Ti-6Al-4V for both rake and flank application of different mwf strategies. *5th CIRP*, v. 87, p. 131–136, 2020.

KURAM, E.; OZCELIK, B. Optimization of machining parameters during micro-milling of Ti6Al4V titanium alloy and inconel 718 materials using taguchi method. *Journal of Engineering Manufacture*, v. 231(2), p. 228–242, 2015.

LEKKALA, R. et al. Characterization and modeling of burr formation in micro-end milling. *Precision Engineering*, v. 35, p. 625–637, 2011.

LIU, C. R.; BARASH, M. M. The mechanical state of the sublayer of a surface generated by chip-removal process, part 1: Cutting with a sharp tool. *Transactions of ASME*, p. 1192–1201, 1976.

LIU, Y. et al. Applications of savitzky-golay filter for seismic random noise reduction. *Acta Geophysica*, v. 64, p. 101–124, 2016.

LKALLOY. *Grau de titânio 23, Ti-6Al-4V-ELI*. China: [s.n.], 2020. Available from internet: ⟨https://lkalloy.com/pt/titanium-and-titanium-alloys/titanium-grade-23/⟩. Access: May 2020.

LÜTJERING, G.; WILLIAMS, J. C. *Titanium*. [S.l.]: Springer, 2007. 15-50 p.

MACHADO Álisson R. et al. Study on burr formation in turning. Proceedings of the 17th International Congress of Mechanical Engineering (COBEM), São Paulo, SP, 2003.

MALISKA, A. M. Microscopia eletrônica de varredura. LABMAT - UFSC, 2003.

MANSO, C. S. et al. Tool wear modelling using micro tool diameter reduction for micro-end-milling of tool steel h13. The International Journal of Advanced Manufacturing Technology, v. 105, p. 2531–2542, 2019.

MARINHO, E. P. *Desenvolvimento de prensa para conformação superplástica com sistema de controle in situ e tempo real de pressão e de temperatura e com módulo de monitoramento da deformação por correlação digital de imagem*. Thesis (PhD) — Universidade de São Paulo, 2016.

MARKUS, W. *Aspectos tecnológicos da minimização e eliminação do fluido de corte no processo de torneamento com insertos de metal-duro revestidos com TiN*. Master's dissertation — Universidade Federal de Santa Catarina, 2001.

MAUREL-PANTEL, A. et al. Experimental investigations from conventional to high speed milling on a 304-l stainless steel. *The International Journal of Advanced Manufacturing Technology*, 2013.

MEHDI, K. Prediction of cutting force in a circular peripheral milling process. *International Journal of Mechanical Engineering and Robotics Research*, v. 7, 2018.

MEIER, H.; HABERLAND, C. Experimental studies on selective laser melting of metallic parts. *Mat.-wiss. u. Werkstofftech*, v. 39, p. 665–670, 2008.

MERGULHÃO, M. V. *Avaliação de propriedades mecânicas e caracterização microestrutural de consolidados de Cobalto-Cromo-Molibdênio obtidos por fusão seletiva a laser e fundição de precisão*. Master's dissertation — IPEN - Universidade de São Paulo, 2017.

METAL-AM. *Growth areas and market potential in Additive Manufacturing*. 2020. Available from internet: ⟨https://www.metal-am.com/introduction-to-metal-additive-manufacturing-and-3d-printing/growth-areas-and-market-potential/⟩. Access: January 2020.

METALLURGISTS, I. *Residual Stress*. 2021. Available from internet: ⟨https://www.imetllc.com/residual-stress/⟩. Access: October 2021.

MILTON, S. et al. Influence of finish machining on the surface integrity of Ti6Al4V produced by selective laser melting. *3rd CIRP Conference on Surface Integrity (CIRP CSI)*, v. 45, p. 127–130, 2016.

MOREIRA, S. R. da S. *Energia específica de corte e integridade superficial no microfresamento do aço ABNT 1045*. Master's dissertation — Faculdade de Engenharia, Universidade Estadual Paulista "Júlio de Mesquita Filho", 2012.

MUMMERY, L. *Surface Texture Analysis: The Hand Book*. [S.l.]: West Germany: Hommelwerke GmbH, 1992.

NI. *NI USB 6221 Board*. 2021. Available from internet: ⟨https://www.ni.com/pdf/dspdf/en/ds-21⟩. Access: October 2021.

NI. *PCIe-6321*. 2021. Available from internet: ⟨https://www.ni.com/pt-br/support/model.pcie-6321.html⟩. Access: October 2021.

OLIVEIRA, E. A. de. *Confiabilidade metrológica na determinação de espécies químicas em materiais siderúrgicos por espectrometria de fluorescência de raios-X*. Master's dissertation — PUC-Rio, 2011.

OLIVEIRA, L. C. P. de. *Estudo da formação de rebarba nos processos de fresamento e torneamento*. Undergraduate thesis — Universidade Federal do Rio de Janeiro, 2015.

OLYMPUS. *Medição da rugosidade de superfícies*. 2021. Available from internet: ⟨https://www.olympus-ims.com/pt/metrology/surface-roughness-measurement-portal/parameters/\#!cms[focus]=022⟩. Access: April 2021.

PAGAC, M. et al. A review of vat photopolymerization technology: Materials, applications, challenges, and future trends of 3D printing. Polymers, 2021.

PAPINI, C. J. *Estudo comparativo de métodos de determinação do tamanho de partícula*. Master's dissertation — Universidade de São Paulo, São Paulo, 2003.

PARHAD, P. et al. The effect of cutting speed and depth of cut on surface roughness during machining of austempered ductile iron. *Transactions of the Indian Institute of Metals*, v. 68, p. 99–108, 2015.

PEDERSON, R. *Microstructure and phase tranformation of Ti-6Al-4V*. Thesis (PhD) — Lulea University of Technology, 2002.

PICARELLI, T. *Microfresamento: Estudo e Aplicação do Processo*. Master's dissertation — Faculdade de Engenharia, Arquitetura e Urbanismo, Universidade Metodista de Piracicaba, 2015.

PODESTÁ, C. E. *Pós esféricos de titânio produzidos a partir de plasma por indução e consolidados por Fusão Seletiva a Laser*. Master's dissertation — IPEN - Universidade de São Paulo, 2018.

PREVITALI, B. et al. Comparative costs of additive manufacturing vs. machining: the case study of the production of forming dies for tube bending. Solid Freeform Fabrication 2017: Proceedings of the 28th Annual International, 2017.

RAILSBACK, L. B. *Some Fundamentals of Mineralogy and Geochemistry*. 2018. Available from internet: ⟨http://www.gly.uga.edu/railsback/FundamentalsIndex.html⟩. Access: April 2018.

RANSIKARBUM, K.; PITAKASO, R.; KIM, N. A decision-support model for additive manufacturing scheduling using an integrative analytic hierarchy process and multi-objective optimization. Applied Sciences, 2020.

REIS, L. L. G.; JUNIOR, W. M. da S.; MACHADO Álisson R. Effect of cutting speed and cutting fluid on the bue geometry of a sae 12l14 free machining steel. Journal of the Brazilian Society of Mechanical Sciences and Engineering, 2007.

RODRIGUES, A. R.; JASINEVICIUS, R. G. *Estado de Superfície*. 2020. Available from internet: ⟨https://edisciplinas.usp.br/pluginfile.php/4187111/mod_resource/content/2⟩. Access: August 2020.

SAHU, N. K.; ANDHARE, A. B. Prediction of residual stress using RSM during turning of Ti–6Al–4V with the 3D FEM assist and experiments. *Springer Nature Applied Sciences*, 2019.

SANDVIK COROMANT. *Modern Metal Cutting: A practical Handbook*. Sweden, 1994. 500 p.

SANTOS, M. W. B. dos. *Investigation of the mechanical behaviour and microstructure evolution of titanium alloys under superplastic and hot forming conditions*. Thesis (PhD) — Universidade de São Paulo, 2017.

SEIKA, A. G.; KOWALSKI, G. *Influência da rugosidade sobre a adesão do revestimento em aços rápidos M2 com tratamento duplex*. Undergraduate thesis — Universidade Tecnológica Federal do Paraná, 2014.

SEKER, U.; HASIRCI, H. Evaluation of machinability of austempered ductile irons in terms of cutting forces and surface quality. *Journal of Materials Processing Technology*, v. 260, 2006.

SHI, K. et al. Effect of tool path on cutting force in end milling. The International Journal of Advanced Manufacturing Technology, 2019.

SHIMADZU. *Fraunhofer Diffraction Theory and Mie Scattering Theory*. 2019. Available from internet: ⟨https://www.shimadzu.com/an/powder/support/practice/p01/lesson13.html⟩. Access: January 2019.

SHOKRANI, A.; DHOKIA, V.; NEWMAN, S. T. Comparative investigation on using cryogenic machining in CNC milling of Ti-6Al-4V titanium alloy. *Machining Science and Technology*, v. 20(3), p. 475–494, 2016.

SHUNMUGAVEL, M. et al. Chip formation characteristics of selective laser melted ti–6al–4v. Australian Journal of Mechanical Engineering, v. 17, p. 109–126, 2017.

SHUNMUGAVEL, M.; POLISHETTY, A.; LITTLEFAIR, G. Microstructure and mechanical properties of wrought and additive manufactured Ti-6Al-4V cylindrical bars. Procedia Technology, v. 20, p. 231–236, 2015.

SILVA, F. L. dos Santos e. *Desenvolvimento de Estratégias para Manufatura Aditiva via Soldagem a Arco*. Undergraduate thesis — Universidade Federal de Santa Catarina, 2017.

SILVA, J. K. de M. *Correlação entre Textura Superficial e Corrosão de Conjugados Processados por PAPVD: Monocamada e Duplex Cr-N*. Master's dissertation — Universidade Federal de Minas Gerais, 2004.

SILVA, L. C. da et al. Study of burr behavior in face milling of ph 13-8 mo stainless steel. CIRP Journal of Manufacturing Science and Technology, v. 8, 2015.

SILVIA; SHIMAKURA. *Interpretação do coeficiente de correlação*. 2006. Available from internet: ⟨http://leg.ufpr.br/~silvia/CE003/node74.html⟩. Access: June 2020.

SINGH, P. P value, statistical significance and clinical significance. *Journal of Clinic and Preventive Cardiology*, 2013.

SOUZA, T. S. G. *Efeito da rugosidade no desgaste de punções de conformação a frio*. Master's dissertation — Universidade de São Paulo, São Paulo, 2016.

SUGAHARA, H. J. et al. Measurement of residual stresses in welded joints by dcp method. *Materials Reasearch*, v. 21, 2018.

TAMINGER, K. *Electron Beam Freeform Fabrication: A Metal Deposition Apparatus to Build Components Directly from CAD*. USA: NASA Langley Research Center, 2008. Available from internet: ⟨http://209.197.69.104/technologies/EBF3/EBF3-Overview.pdf⟩. Access: April 2021.

TURIBUS, S. N. et al. Tensometria por técnica de difração de raios x aplicada na análise de soldagens. *19º Congresso Brasileiro de Engenharia e Ciência dos Materiais - CBECiMat*, 2010.

UHLMANN, E. et al. Additive Manufacturing of Titanium Alloy for Aircraft Components. Procedia CIRP, v. 35, p. 55–60, 2015.

VAFADAR, A. et al. Advances in metal additive manufacturing: A review of common processes, industrial applications, and current challenges. *Applied Sciences*, 2021.

VIEIRA, S. *Estatística Básica*. [S.l.]: Cengage Learning Edições Ltda., 2012.

WAIKAR, R. A.; GUO, Y. B. A comprehensive characterization of 3D surface topography induced by hard turning versus grinding. journal of materials processing technology, v. 197, p. 189–199, 2008.

WAN, Y. et al. Weld residual stresses in a thick plate considering back chipping: Neutron diffraction, contour method and finite element simulation study. *Materials Science and Engineering*, v. 699, p. 62–70, 2017.

WANG, W.; KWEON, S.; YANG, S. A study on roughness of the micro-end-milled surface produced by a miniatured machine tool. Journal of Materials Processing Technology, p. 702–708, 2005.

WOHLERS, T. et al. 3D printing and additive manufacturing state of the industry: Annual worldwide progress report. *Lund University: Lund, Sweden.*, 2017.

XIONG, X.; ZHANG, H.; WANG, G. Metal direct prototyping by using hybrid plasma deposition and milling. Journal of Materials Processing Technology, v. 209, p. 124–130, 2009.

YANG, J. et al. Formation and control of martensite in Ti-6Al-4V alloy produced by Selective Laser Melting. *Materials and Design*, v. 108, p. 308–318, 2016.

YAP, C. Y. et al. Review of selective laser melting: materials and applications. Applied Physics Reviews, v. 2, 2015.

YOUSSEF, H. A.; EL-HOFY, H. *Machining technology: machine tools and operations*. [S.l.]: Taylor & Francis Group, 2008.

YUN, H. et al. Ploughing detection in micromilling processes using the cutting force signal. *International Journal of Machine Tools and Manufacture*, Elsevier Limited, v. 51, n. 5, p. 377–382, 2011. ISSN 0890-6955.

ZHANG, Y. et al. *Additive manufacturing processes and equipment*. [S.l.]: Additive Manufacturing: Materials, Processes, Quantifications and Applications, 2018. 39-51 p.

ZIBEROV, M. *Microfresamento da liga Ti-6Al-4V com microferramentas com diferentes revestimentos e aplicação de MQL*. Thesis (PhD) — Faculdade de Engenharia Mecânica, Universidade Federal de Uberlândia, 2018.